UNIVERSITY OF OKLAHOMA

GRADUATE COLLEGE

IMPLEMENTATION AND VALIDATION OF A HYDRO-MECHANICAL ELASTOPLASTIC CONSTITUTIVE MODEL FOR FULLY COUPLED ANALYSIS OF UNSATURATED SOILS

A DISSERTATION

SUBMITTED TO THE GRADUATE FACULTY

in partial fulfillment of the requirements for the

Degree of

DOCTOR OF PHILOSOPHY

By

BO ZHANG
Norman, Oklahoma
2017

IMPLEMENTATION AND VALIDATION OF A HYDRO-MECHANICAL ELASTOPLASTIC CONSTITUTIVE MODEL FOR FULLY COUPLED ANALYSIS OF UNSATURATED SOILS

A DISSERTATION APPROVED FOR THE
SCHOOL OF CIVIL ENGINEERING AND ENVIRONMENTAL SCIENCE

BY

_____
Dr. Kanthasamy Muraleetharan, Chair

_____
Dr. John Albert

_____
Dr. Amy Cerato

_____
Dr. Randall Kolar

_____
Dr. Gerald Miller

DEDICATION

To my parents for all their endless love and support

ACKNOWLEDGEMENTS

I would like to express my sincere gratitude to my advisor, Professor Kanthasamy Muraleetharan for his exceptional guidance, encouragement, patience, and dedication during my studies and research at the University of Oklahoma (OU). His incredible scientific intuition and academic curiosity has immensely inspired and enriched my growth as a student and will guide my future work and research. He has certainly become a role model for me as a researcher and an academic.

I am grateful to Dr. John Albert, Dr. Amy Cerato, Dr. Randall Kolar, and Dr. Gerald Miller for serving on my dissertation committee. Their significant guidance and insightful comments are greatly valued.

I would like to thank all my friends who supported and encouraged me to get through difficult times. I would like to express my most profound gratitude to my family for their never-ending support, love and encouragement throughout my Ph.D studies. It would not have been possible to achieve this journey without their sacrifice and endless support.

TABLE OF CONTENTS

LIST OF TABLES

LIST OF FIGURES

ABSTRACT

Unsaturated soils are commonly encountered in natural soil deposits above the ground water table and in civil infrastructure construction as compacted soils. In earthquake prone areas, problems arise from dynamic loading of unsaturated soils. These problems have received increasing attention in geotechnical and geo-environmental engineering research in recent years. Many geohazards such as liquefaction, slope failures, and embankment collapse are triggered when unsaturated soils are subjected to dynamic loading. Although extensive work has been done to study the liquefaction behavior of unsaturated sands in the laboratory, relatively few numerical studies have been carried out to investigate the liquefaction potential of unsaturated sands under different degrees of saturation, relative densities, and initial effective stresses. Thus far, most of the developments in the numerical modeling of the dynamic response of unsaturated soils have occurred in relation to monotonic loading of unsaturated soils and the important effects such as elastoplasticity, hydro-mechanical coupling, and hydraulic hysteresis are rarely taken into account in the constitutive models used in these analysis procedures.

In this dissertation, numerical investigation of the capability of a coupled hydro-mechanical elastoplastic constitutive model for unsaturated sands and silts (CM4USS) to predict the liquefaction potential of unsaturated sands at different degrees of saturation and confining pressures is first carried out. A design chart that can be used to evaluate the liquefaction potential of unsaturated sands is developed through numerical investigation on a series of undrained, stress-controlled, cyclic triaxial tests for Toyoura

and Nevada sands under different degrees of saturation, relative densities and initial effective confining pressures. Then a hysteretic model for soil water characteristic curves (SWCCs) is implemented into U_DYSAC2, a fully coupled fluid flow-solid deformation finite element computer code. An unsaturated soil embankment subjected to base shaking is analyzed and the results obtained using the code with non-hysteretic (drying bound) and hysteretic SWCCs are compared to each other. CM4USS is then implemented into U_DYSAC2 and several numerical examples are used to verify the implementation. These examples demonstrate that the modified U_DYSAC2 is capable of predicting the dynamic behavior of unsaturated soils. Finally, the effects of the degree of saturation and relative density on the liquefaction potential of level ground unsaturated Nevada sand deposits subjected to base shaking is studied using the modified code. The simulation results are consistent with those predicted at a single element level, yet they provide valuable insight into the behavior of unsaturated sands in boundary value problems.

CHAPTER 1 INTRODUCTION

1.1 Background

Unsaturated soils are three-phase porous media consisting of a solid skeleton, pore water, and pore air. They exhibit significantly different behavior from saturated soils (Fredlund and Rahardjo 1993). Unsaturated soils are commonly encountered in natural soil deposits above the ground water table and in civil infrastructure construction as compacted soils. In earthquake prone areas, problems arise from dynamic loading of unsaturated soils. These problems have received increasing attention in geotechnical and geo-environmental engineering research in recent years. The repeated loading and unloading (cyclic loading) on unsaturated soils during dynamic loading leads to decrease in shear strength and stiffness due to pore water pressure build up. Many geohazards such as liquefaction, slope failures, and embankment collapse are triggered when unsaturated soils are subjected to dynamic loading (Kazama and Unno 2007, Okamura et al. 2013, Higo et al. 2015).

Liquefaction is a common occurrence in saturated granular soils in many parts of the world subjected to earthquakes. Recent laboratory tests have shown that unsaturated granular soils can also liquefy (Sherif et al. 1977, Chaney 1978, Yoshimi et al. 1989, Huang et al. 1999, Grozic et al. 2000, Tsukamoto et al. 2002, Eseller-Bayat

2009, Arab et al. 2011, Eseller-Bayat et al. 2013a, b, Tsukamoto et al. 2014, Liu and Xu 2015). The factors such as degree of saturation, relative density, and initial effective stress affect the liquefaction resistance of unsaturated soils. Although extensive work has been done to study the liquefaction behavior of unsaturated sands in the laboratory, relatively few numerical studies have been carried out to investigate the liquefaction potential of unsaturated sands under different degrees of saturation, relative densities, and initial effective stresses.

Accurate prediction of dynamic behavior of unsaturated soils is of practical importance to many geotechnical engineering problems, such as soil-structure interaction (Ravichandran et al. 2015), liquefaction evaluation (Okamura and Soga 2006, Unno et al. 2008, Zhang et al. 2016), wave propagation (Chen et al. 2011, Maghoul et al. 2011b, Steeb et al. 2014), and earthquake resistance of structures (Khoei et al. 2004, Ravichandran 2009, Ravichandran and Muraleetharan 2009, Khoei and Mohammadnejad 2011, Mori et al. 2011, Oka et al. 2012, Sadeghi et al. 2014, Matsumaru and Uzuoka 2016, Yoshikawa et al. 2016). A fully coupled analysis of unsaturated soils involving solid deformation and fluid flows is complicated due to the interactions among various phases and interfaces as well as the nonlinear behavior of the solid skeleton. An important consideration in the numerical modeling (e.g. the finite element method) of the dynamic response of unsaturated soils is the accurate constitutive modeling of the cyclic mechanical response of solid skeleton and the hydraulic response of fluids that fill the voids between the solid skeleton. Thus far, most of the developments in unsaturated soils have occurred in relation to monotonic loading of unsaturated soils and the important effects such as elastoplasticity, hydro-mechanical

coupling, and hydraulic hysteresis are rarely taken into account in the constitutive models used in these analysis procedures. Therefore, a systematic investigation of unsaturated soils using a fully coupled analysis procedure that includes elastoplastic constitutive models that can accurately describe the cyclic responses is necessary to simulate dynamic boundary value problems accurately.

1.2 Objectives

The primary objective of the proposed research is to implement and validate a coupled hydro-mechanical elastoplastic constitutive model for unsaturated sands and silts (CM4USS) developed by Liu and Muraleetharan (2012a, 2012b) into a fully coupled finite element computer code, U_DYSAC2 (Muraleetharan and Wei 1999b), to solve boundary and initial value problems in unsaturated soils, especially dynamic loading problems. The proposed research is divided into the following detailed tasks:

- Investigate the effect of initial conditions (degree of saturation, relative density and confining pressure) on the liquefaction of unsaturated sands using CM4USS and develop a design chart that can be used to evaluate the liquefaction potential of unsaturated sands.
- Implement the hysteretic soil water characteristic curves (SWCCs) (a part of CM4USS) into U_DYSAC2 for use in the analysis of dynamic response of unsaturated soils and study the effect of the hydraulic hysteresis on the dynamic response of unsaturated soils.
- Implement CM4CSS into U_DYSAC2 using an implicit integration algorithm

and validate the implementation using numerical examples on unsaturated soils subjected to dynamic loading.

1.3 Dissertation Layout

In addition to this introduction, the dissertation is arranged in 7 chapters as follows:

- Background literature related to elastoplastic constitutive models for unsaturated soils under cyclic loading, finite element models for unsaturated soils, and the liquefaction of unsaturated soils are reviewed in Chapter 2.
- The numerical investigation of the capability of CM4USS for predicting the liquefaction potential of unsaturated sands at different initial conditions is investigated in Chapter 3. A design chart is also developed in this chapter to evaluate the liquefaction potential of unsaturated sands based on the numerical analysis through a series of simulated undrained, stress-controlled, cyclic triaxial tests on Toyoura and Nevada sands.
- The fully coupled equations governing the dynamic behavior of unsaturated soils used in U_DYSAC2 are first presented in Chapter 4. The finite element spatial discretization of these equations using Galerkin approach is then presented. Finally, a three-parameter Hilber-Hughes-Taylor time integration scheme employed to integrate the finite element equations in U_DYSAC2 is described.
- The implementation of SWCCs used in CM4USS into U_DYSAC2 is presented

in Chapter 5. An unsaturated embankment subjected to base shaking is analyzed and the results obtained using the code with non-hysteretic (drying bound) and hysteretic SWCCs are compared to each other in this chapter. The effect of the hydraulic hysteresis on the dynamic behavior of unsaturated soils is studied by comparing the predicted pore water and pore air pressures, suction, and displacements.

- The implementation and validation of CM4USS into U_DYSAC2 is presented in Chapter 6. The validation is performed through numerical examples. The results demonstrate that CM4USS implemented into U_DYSAC2 is capable of predicting the dynamic behavior of unsaturated soils.
- The summary and conclusions of this research and the recommendations for further studies are given in Chapter 7.

CHAPTER 2 LITERATURE REVIEW

2.1 Introduction

The finite element method (FEM) has been utilized to model the dynamic behavior of unsaturated soils. Two critical components in numerical modeling of dynamic response of unsaturated soils are the constitutive models, one describing the mechanical behavior of solid skeleton and the other one governing the hydraulic behavior of fluids that fill the voids between the solid skeleton. Cyclic response (loading/unloading) of unsaturated soils is complex due to the coupling effect between mechanical and hydraulic behavior.

This chapter presents a thorough review of the existing literature on liquefaction of unsaturated soils and the constitutive and numerical models for unsaturated soils under cyclic and dynamic loading. Section 2.2 presents the previous research on liquefaction of unsaturated soils. The development of constitutive models for unsaturated soils under monotonic and cyclic loading is reviewed in Section 2.3. Section 2.4 presents the available literature on finite element analysis of unsaturated soils. A summary of knowledge gap is given in Section 2.5.

2.2 Liquefaction of Unsaturated Soils

Soil liquefaction is a phenomenon in which large pore pressures develop during cyclic loading of granular soils and subsequent softening of these soils. During an earthquake, a saturated soil loses shearing resistance and develops excessive strains due to the pore water pressure buildup, resulting in slope failures, foundation damage, lateral spreading, and settlement. The phenomenon of liquefaction in saturated soils has been observed in the past during moderate to large earthquakes, such as in 1999 Chi-Chi (Taiwan) and 1964 Niigata (Japan) earthquakes. In geotechnical earthquake engineering practice, liquefaction is only considered in saturated soils and 100% degree of saturation is an essential prerequisite for liquefaction. Unsaturated granular soils are considered to be not susceptible to liquefaction. A saturated soil reaches initial liquefaction when the effective stress (σ') becomes zero. Under level ground conditions, σ' is the initial effective vertical stress and under isotropic stress conditions, such as in laboratory triaxial tests, σ' is the initial effective mean normal stress. Therefore, when the soil liquefies, the excess pore water pressure ratio ($R_u = \Delta u / \sigma'$) becomes 1.0, where Δu is the excess pore water pressure generated during cyclic shearing.

Recent laboratory tests have, however, shown that not only saturated granular soils, but also unsaturated granular soils can liquefy (Sherif et al. 1977, Chaney 1978, Yoshimi et al. 1989, Huang et al. 1999, Grozic et al. 2000, Tsukamoto et al. 2002, Tsukamoto et al. 2014, Liu and Xu 2015). Liquefaction in unsaturated soils has also been observed in the field (Hsu et al. 1995, Chillarige et al. 1997, Grozic et al. 2000,

Uzuoka et al. 2005). Similar to the definition of liquefaction in saturated soils, an unsaturated soil reaches complete liquefaction when the effective stress reaches a value of zero, i.e., the pore water pressure and pore air pressure are equal to the initial total stress (Liu and Xu 2015).

Some previous research works have studied the liquefaction of unsaturated soils. Martin et al. (1978) selected a theoretical model to investigate the effect of degree of saturation on the liquefaction potential of unsaturated soils. Their results showed that cyclic stress ratio required to cause liquefaction significantly increases with a small decrease in the degree of saturation, i.e., a 1% drop in degree of saturation of the saturated sand specimen with a porosity $n = 0.4$ results in 28% decrease in the pore water pressure increase per cycle. Subsequent laboratory tests results confirmed this finding and concluded that the degree of saturation (expressed in terms of the B-value) has the most significant effect on the soil resistance to onset of liquefaction (Chaney 1978, Yoshimi et al. 1989, Xia and Hu 1991, Ishihara et al. 1998, Huang et al. 1999, Fourie et al. 2001, Ishihara et al. 2001, Ishihara and Tsukamoto 2004, Nakazawa et al. 2004, Okamura et al. 2006, Okamura and Soga 2006, Hatanaka and Masuda 2008, Arab et al. 2011).As shown in Fig. 2.1, even a slight decrease in the degree of saturation can cause a significant increase in the liquefaction resistance of unsaturated sands. In Fig. 2.1, the initial liquefaction is defined on the basis of a soil specimen deforming to 5% double amplitude (DA) axial strain. Chaney (1978) and Yoshimi et al. (1989) demonstrated that the liquefaction resistance at $S_r = 90\%$ is approximately two times that at $S_r = 100\%$. Xia and Hu (1991) have shown that the liquefaction resistance

increases about 30% as the degree of saturation decreases from $S_r = 100\%$ to $S_r = 97.8\%$.

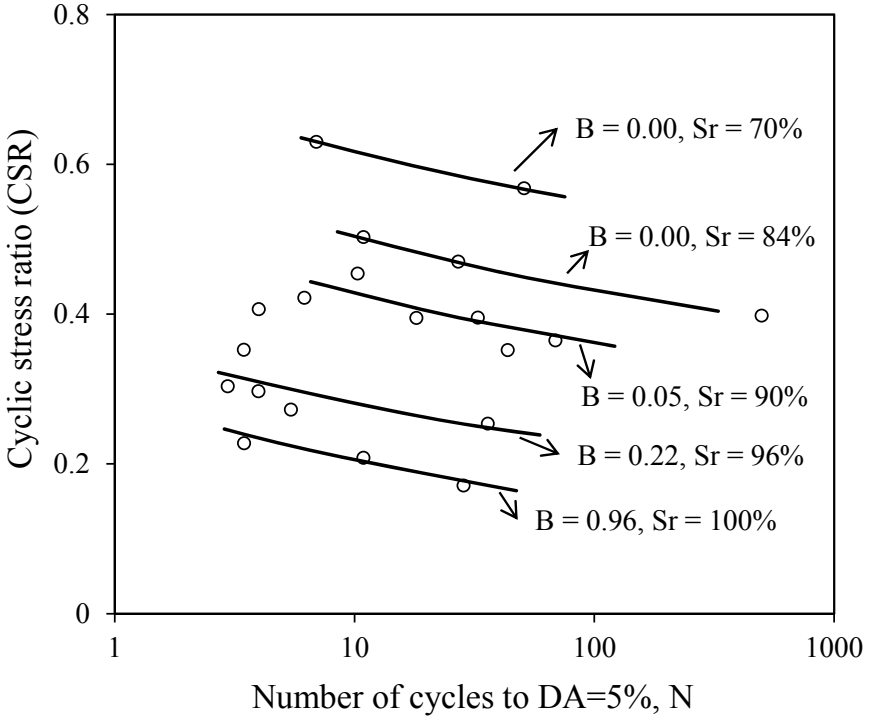

Fig. 2.1 Effect of degree of saturation on cyclic stress ratio for Toyoura sand (after Yoshimi et al. 1989)

The effect of saturation on liquefaction potential was also observed in the field in the 1995 Kobe earthquake in Japan and the 2001 Bhuj earthquake in India. Nagao et al. (2007) cited Shiraishi (1997) work and reported that 312 examples of structures with entrapped air in foundation were prevented from serious damage by liquefaction in the Kobe earthquake. Singh et al. (2005) examined the damage to six earth dams in the 2001 Bhuj earthquake. The six reservoirs of these dams were nearly empty during the earthquake, and the liquefiable soils were in a partially saturated state. The field

observed dam performance indicated that the downstream area of the dams generally had less damage than the upstream area due to partial saturation on the downstream area. In fact, changing a saturated sand deposit into an unsaturated deposit by injecting air or through chemical means or denitrification process has been considered as a liquefaction counter measure (Okamura and Teraoka 2005, Yegian et al. 2007, Okamura et al. 2011, Rebata-Landa and Santamarina 2012, Eseller-Bayat et al. 2013a, He and Chu 2014). Lowering of the groundwater table and injection of air bubbles were used as countermeasures against soil liquefaction off the Pacific coast after the 2011 Tohoku Earthquake (Tsukamoto et al. 2014). Okamura et al. (2006) discussed the liquefaction resistance of loose sand deposits that was improved by sand compaction piles (SCP). Inspection of undisturbed samples and the primary wave velocity testing revealed that the increase in liquefaction resistance is due to the desaturation of ground during SCP installation. The degree of saturation was lower than 77% for the sand piles in the improved area and 91% for the improved sand layers. The decrease in the degree of saturation resulted in a significant increase in liquefaction resistance. The degree of saturation of saturated soils can be significantly reduced by injecting air and the unsaturated condition can last for a long time (Okamura et al. 2003, Okamura et al. 2006). Yegian et al. (2007) studied a new liquefaction mitigation technique by introducing small amount of gas into soil pores utilizing the electrolysis method and drainage-recharge of the pore water. The effect of saturation on the generation of excess pore water pressure was investigated by the cyclic shear strain controlled tests. The experimental results revealed that the small decrease in the degree of saturation can increase the initial liquefaction resistance.

Attempts have been made to understand the mechanism of liquefaction and develop charts using in situ testing, which include Standard Penetration Test (SPT), Cone Penetration Test (CPT), and shear wave velocity measurement, for evaluating the liquefaction potential of saturated soils (Seed and Idriss 1971, Seed et al. 1983, Robertson and Campanella 1985, Seed et al. 1985, Youd et al. 2001, Kayen et al. 2013, Maurer et al. 2015). A large number of computational models can now be found in the literature for simulating liquefaction of saturated soils (Oka et al. 1994, Buscarnera and Whittle 2013, Kuhn et al. 2014). The cyclic resistance ratio (CRR) is the maximum cyclic stress ratio (maximum shear stress divided by effective confining pressure) at which a saturated soil can resist liquefaction. CRR is influenced by overburden pressure, static shear stress and earthquake magnitude and should be corrected to account for these factors, which is given by (Youd et al. 2001, Montgomery et al. 2014)

$$CRR_{correted} = CRR \cdot MSF \cdot K_{\sigma} \cdot K_{\alpha} \tag{2.1}$$

where MSF is the magnitude scaling factor, K_{σ} is the correction factor for overburden pressure, K_{α} is the correction factor for static shear stress. CRR of unsaturated soils should be corrected to account for the effect of degree of saturation by modifying Eq.(2.1) (Hossain et al. 2013)

$$CRR_{correted} = CRR \cdot MSF \cdot K_{\sigma} \cdot K_{\alpha} \cdot K_{s} \tag{2.2}$$

where K_s is the correction factor for degree of saturation, which is defined as the ratio of CRR of unsaturated soil to the CRR of the soil in a saturated state. Presented in Fig. 2.2 is the relationship between degree of saturation and the correction factor K_s, based on the laboratory test results from literature. It can clearly be seen that the capacity of an unsaturated soil to resist liquefaction increases as the degree of saturation decreases. The compression wave velocity and shear wave velocity have been used to evaluate the liquefaction resistance of unsaturated sand based on the laboratory test results by many researchers (Yang 2002, Yang et al. 2004, Hossain et al. 2013).

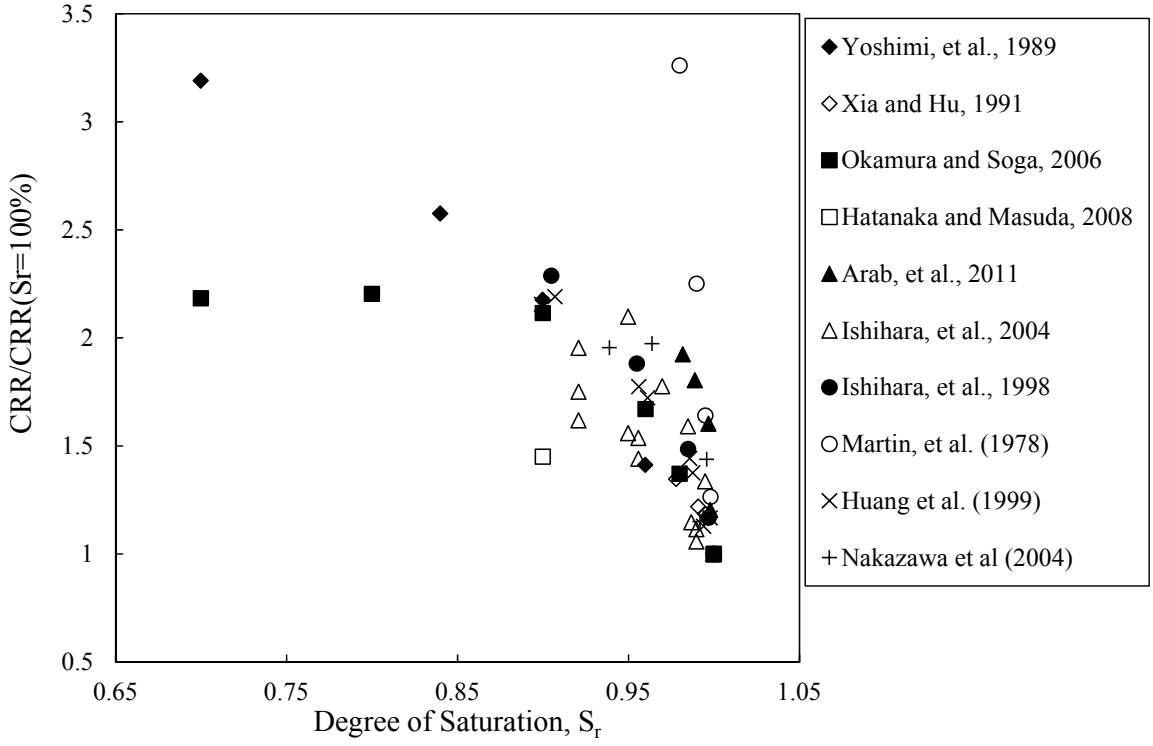

Fig. 2.2 Relationship between degree of saturation and correct factor K_s

The degree of saturation is, however, not the only factor that affects the resistance to liquefaction of unsaturated soils. The relative density and initial confining pressure also have a profound influence on the cyclic strength of unsaturated sands (Grozic et al. 2000, Okamura and Soga 2006). Liu and Xu (2015) concluded that the liquefaction resistance increases with a decrease in the initial degree of saturation and increases in relative density and initial effective confining pressure through the results of strain-controlled cyclic loading tests on saturated and unsaturated Nevada sand under different relative densities (30% and 70%), effective confining stresses (50 and 200 kPa), and degrees of saturation (90%, 95%, and 100%).

Although extensive work has been done to study the liquefaction behavior of unsaturated sands in the laboratory, relatively few numerical studies have been carried out to investigate the liquefaction potential of unsaturated sands. Pietruszczak et al. (2003) investigated the liquefaction potential of an one dimensional unsaturated sand layer at degrees of saturation of 85%, 95 %, 98%, and 100% subjected to a scaled-down version of the El Centro (1940) earthquake using a constitutive model (Pietruszczak and Pande 1996). Their findings confirmed that the liquefaction resistance of unsaturated sands increases when the degree of saturation is a few percent below 100. Jafari-Mehrabadi et al. (2007) developed a constitutive model to predict the cyclic behavior of unsaturated sands at various degrees of saturation (95% and higher) under seismic loads based on Henry's law for dissolution of gas in water, the ideal gas law, and the law of conservation of mass. Khalili et al. (2008) studied the undrained cyclic behavior of unsaturated silty sand using a fully coupled constitutive model. The numerical simulation results showed that two samples at a degree of saturation 90% with cyclic

stress ratios (CSR) (CSR is defined as the ratio of the maximum shear stress to the net confining stress) of 0.35 and 0.30 can liquefy and the test with the lower CSR showed higher liquefaction resistance. Bian and Shahrour (2009) presented a numerical model for the description of the liquefaction behavior of unsaturated sandy soils based on the framework of theory of Biot and the multiphase theory of Coussy. Numerical simulations were conducted for the undrained strain-controlled triaxial test on unsaturated Hostun sand at different initial degrees of water saturation (100%, 99%, 95% and 90%). It was concluded that the degree of saturation largely influences the liquefaction resistance of sandy soils and the decrease in degree of saturation increases the soils liquefaction resistance. However, the initial pore water pressure was assumed to be zero and the pore air pressure was not considered in the numerical simulations. Liu and Muraleetharan (2012c) conducted a parametric study to research the combined effects of initial degree of saturation and relative density on liquefaction by a constitutive model for unsaturated sands and silts. The results revealed that decrease in the initial degree of saturation and increase in the initial relative density can prevent the occurrence of liquefaction.

2.3 Constitutive Models for Unsaturated Soils

Laboratory tests indicate that the hydraulic and mechanical behaviors of unsaturated soils are coupled (Vaunat et al. 2000, Gallipoli et al. 2003, Tarantino and Tombolato 2005, Geiser et al. 2006, Miller et al. 2008) and the relationship between water content and soil suction called SWCCs exhibit hysteresis during wetting and

drying cycles (Topp 1969, Poulovassilis 1970, Topp 1971). The plastic volumetric strain affects SWCCs by increasing the degree of saturation and causing a change in water content (Wheeler 1996, Rampino et al. 1999, Vanapalli et al. 1999, Wheeler et al. 2003, Buenfil et al. 2005). Hysteretic SWCCs, on the other hand, influence stress-strain behavior of a soil (Gallipoli et al. 2003) and produces irreversible volumetric strain (Alonso et al. 1995). The important role of this coupling effect has come to the forefront of many geotechnical engineering problems (Cho and Lee 2001, Qi and Vanapalli 2015). It is critical to incorporate this coupling effect into constitutive models to reflect the real behavior of unsaturated soils subjected to different loading conditions.

The first comprehensive elastoplastic constitutive model that deals with the stress-strain behavior of unsaturated soils was the Barcelona Basic Model (BBM) (Alonso et al. 1990), which is an extension of the modified Cam-clay model. The distinctive features of this model include: (1) two independent stress state variables, namely net stress (total stress in excess of pore air pressure) and suction (pore air pressure in excess of pore water pressure); (2) elastic strain increments that are related to the net stress changes and suction changes; and (3) a Loading-Collapse surface defined in the net stress-suction space that indicates the size of the elastic domain increase with suction increase. Since then, investigators have developed many constitutive models for unsaturated soils. However, limitations existed in the earlier developed models: some of them do not account for the influence of the mechanical behavior on hydraulic behavior (Gallipoli et al. 2003), some only partially accentuated the mechanical behavior on hydraulic behavior (Vaunat et al. 2000), and some of them do not consider the hydraulic hysteresis (Wheeler and Sivakumar 1995, Chiu and Ng

2003, GENS 2010). The first constitutive model incorporating the coupled hydro-mechanical behavior is attributed to Vaunat et al. (2000). Gallipoli et al. (2003) proposed an elastoplastic constitutive model for unsaturated soils incorporating the influence of degree of saturation and suction on mechanical behavior.

The conventional constitutive models for unsaturated soils fail to describe the soil behavior under cyclic loading. Cyclic loading on unsaturated soils in this dissertation includes the cyclic drying and wetting, cyclic isotropic loading and cyclic deviator stress loading, which results in cyclic variations in the stress (effective stress and matric suction) or strain (solid skeleton strain and volumetric water content) in the soil. Typical examples of cyclic loading are natural loads due to wind, waves, earthquakes, traffic loading, machine foundations, and variations in pore water pressure as a result of infiltration and evapotranspiration or fluctuation of the ground water level.

Many constitutive models have been proposed to simulate the stress-strain behavior for saturated soils under cyclic loading based on kinematic hardening plasticity (Lade and Kim 1988, Pastor et al. 1990, Inel and Lade 1997), multi-surface plasticity theory (Mróz 1967, Mrŏz et al. 1978, Mróz et al. 1979, Mróz and Pietruszczak 1983, Pietruszczak and Mróz 1983), and the bounding surface plasticity theory (Dafalias and Popov 1975, Krieg 1975, Dafalias and Popov 1976, Dafalias 1986, Dafalias and Herrmann 1986). Among these works, the bounding surface plasticity theory has attracted many researchers' attention due to the ease of use in describing soil behavior under cyclic loading. The bounding surface plasticity concept is based on the observation that plasticity can occur inside a conventional yield surface. The unique feature of the bounding surface theory is that there is a smooth transition of stiffness

from elasticity to elastoplasticity. The plastic modulus is a decreasing function of the distance between the current stress state and the "image" stress state on the bounding surface. Many researchers have developed various constitutive models for unsaturated soils under cyclic loading and some progress has been achieved. Yang et al. (2008) presented an elastoplastic constitutive model for unsaturated structured loess soils under cyclic loading based on the bounding surface theory and the damage theory for structured soils. In this model, the bond degradation was defined as a function of the accumulated strain and BBM was accepted to describe the unsaturated soil behavior. The hydraulic hysteresis was not considered in this model. Khalili et al. (2008) presented a coupled hydro-mechanical elastoplastic constitutive model for unsaturated soils under cyclic loading using the bounding surface plasticity. The model was validated by comparing the model simulation results with the experimental results from drying-wetting tests on clay, isotropic and triaxial loading tests on silt and undrained cyclic triaxial tests on sand. Zhou and Ng (2016) developed a thermo-mechanical constitutive model to simulate the cyclic behavior for unsaturated soil based on the bounding surface plasticity model. The unsaturated silt behavior under suction- and temperature-controlled cyclic loading was simulated.

Following the saturated sand models developed by Manzari and Dafalias (1997) and Taiebat and Dafalias (2008), Liu and Muraleetharan (2012a, 2012b) proposed a comprehensive coupled hydro-mechanical elastoplastic constitutive model (named as CM4USS in this dissertation) to simulate the monotonic and cyclic behavior for unsaturated sands and silts that is based on the critical state soil mechanics framework

and the bounding surface plasticity. This rate independent constitutive model has the following special features:

(1) a hysteretic model for SWCCs based on the bounding surface plasticity concept;

(2) coupling mechanisms between SWCCs and the stress-strain behavior of the solid skeleton;

(3) hysteresis in the stress-strain response of the solid skeleton.

The bounding surface plasticity concept is incorporated into the hydro-mechanical behavior to accurately simulate the monotonic and cyclic behavior of unsaturated soils. This model will be utilized in this research. The details of this model are presented in Chapter 3.

2.4 Finite Element Analysis of Dynamic Behavior of Unsaturated Soils

In recent years, fully coupled dynamic analysis procedures have been increasingly used in geotechnical engineering practice and research to calculate deformations and pore pressure and provide insight into the behavior of geotechnical structures on unsaturated soils subjected to earthquakes (Khoei et al. 2004, Ravichandran 2009, Ravichandran and Muraleetharan 2009, Khoei and Mohammadnejad 2011, Mori et al. 2011, Oka et al. 2012, Matsumaru and Uzuoka 2016).

The behavior of unsaturated soils is governed largely by the coupling effects between the solid skeleton, pore water, and pore air. In a finite element analysis of unsaturated soils these coupling effects have to be properly taken into account. The first

general model for the quantitative study of dynamic analysis of unsaturated soils is attributed to Zienkiewicz et al. (1990). Based on the assumption that the air pressure is constant, a saturated soil formulation was extended to unsaturated problems. Since then, great efforts have been devoted to the development of analysis procedures for unsaturated soils by many researchers (Meroi et al. 1995, Schrefler and Scotta 2001, Khoei et al. 2004, Ravichandran and Muraleetharan 2009). Many simplifying assumptions such as constant air pressure (usually atmospheric pressure) (Sheng et al. 2003, Sheng et al. 2008b, Callari and Abati 2009, Pedroso 2015), quasi-static condition (Schrefler and Xiaoyong 1993, Laloui et al. 2003, Oettl et al. 2004, Stelzer and Hofstetter 2005), and simple constitutive models for the solid skeleton (Uzuoka and Borja 2012) were made. It is worth mentioning that the pore air pressure plays a significant role in the dynamic behavior of unsaturated soils and structures, such as earth dams (Muraleetharan and Wei 2000, Khoei and Mohammadnejad 2011) and liquefaction (Kazama et al. 2006, Okamura and Soga 2006, Unno et al. 2008). The pore air pressure is treated as a primary variable in recent developments (Habte 2006, Ravichandran 2009, Ravichandran and Muraleetharan 2009, Maghoul et al. 2011a, Uzuoka and Borja 2012, Ravichandran and Krishnapillai 2013, Uzuoka et al. 2014).

One common feature in the aforementioned numerical analyses of dynamic behavior of unsaturated soils was the use of a single curve for SWCCs. The hydraulic hysteresis can significantly influence the behavior of unsaturated soils subjected to dynamic loading (Ng et al. 2009, Khosravi and McCartney 2012) and therefore modeling with a single SWCC is not appropriate. Some investigation has been carried out to incorporate the hydraulic hysteresis in the numerical analysis of dynamic

behavior of unsaturated soils. Tamagnini (2005) studied an ideal dike subjected to the variation of water level utilizing the finite element analysis. The stress-strain behavior of the solid skeleton was described by an extended Cam-clay model for unsaturated soils with the incorporation of the hydraulic hysteresis (Tamagnini 2004). The finite element analysis results showed that the simulated pore pressure, vertical displacement, and stress path were greatly influenced by the hydraulic hysteresis. Pedroso (2015) developed a formulation based on the theory of porous media with hysteresis. The pore air pressure was assumed to be zero and the proposed formulation was used to study the porous media behavior under drying and wetting cycles. Shahbodagh-Khan et al. (2015) proposed a fully coupled flow-deformation numerical model for the nonlinear dynamic deformation analysis of unsaturated soils accounting for the hydraulic hysteresis.

Usually the elastoplastic constitutive models are incorporated to describe the cyclic mechanical behavior of solid skeleton and the cyclic hydraulic response of fluids that fill the voids between solid skeleton. Among the considerable recent advances is the successful implementation of some non-linear constitutive models to improve the capabilities of the numerical procedures. Ravichandran and Muraleetharan (2009) employed a generalized elastoplastic constitutive model (Muraleetharan and Nedunuri 1998), which used net stress and suction to describe the stress-strain behavior of unsaturated soils, to study dynamic behavior of unsaturated embankments. Yoshikawa et al. (2016) preformed the soil–water–air coupled finite deformation analysis of the seismic behavior of the unsaturated embankment on clayey ground using SYS Cam-clay model (Asaoka et al. 2002). The modified Pastor–Zienkiewicz plasticity model for clay (Pastor et al. 1990, Bolzon et al. 1996) was accepted to describe the mechanical

behavior of the lower San Fernando dam and the Mahabad dam under earthquake loading in the numerical modeling of dynamic behavior of unsaturated soils (Khoei and Mohammadnejad 2011). Although some progress has been made, it is apparent that more research is needed, specifically with coupled hydro-mechanical models that account for hysteresis in both SWCCs and the solid skeleton stress-strain curves.

Thus far, most of the developments in numerical analysis of dynamic behavior of unsaturated soils have occurred in relation to monotonic loading of unsaturated soils and the important effects such as elastoplasticity, hydro-mechanical coupling, and hydraulic hysteresis are rarely taken into account in the constitutive models used in these analysis procedures. Furthermore, majority of the development so far has focused solely on unsaturated clay or plastic silts. Therefore, elastoplastic constitutive models for unsaturated sands and non-plastic silts that can accurately describe the cyclic responses are needed to be implemented into unsaturated soil finite element computer codes to simulate boundary value problems.

2.5 Summary of Knowledge Gap

Based on the literature review of the numerical modeling and liquefaction of unsaturated soils, it can be concluded that: 1) a systematic study of the combined effects of degree of saturation, relative density, and initial effective stress on liquefaction of unsaturated granular soils using a comprehensive constitutive model is needed; 2) the incorporation of hydraulic hysteresis in the finite element analysis of dynamic behavior of unsaturated soils will provide useful insights; 3) a fully coupled

finite element dynamic analysis procedure with a coupled hydro-mechanical constitutive model is needed to solve boundary value problems involving the dynamic behavior of unsaturated sands and non-plastic silts.

CHAPTER 3 A COUPLED HYDRO-MECHANICAL CONSTITUTIVE MODEL FOR UNSATURATED SANDS AND SILTS AND MODELING LIQUEFACTION

3.1 Introduction

A thorough literature review in Chapter 2 shows that relatively few numerical studies have been carried out to investigate the liquefaction potential of unsaturated sands under different initial conditions and the liquefaction resistance of unsaturated soils is influenced by degree of saturation, relative density and initial effective stress. A systematic investigation of the combined effects of these factors on liquefaction of unsaturated granular soils is lacking. Since unsaturated soils are commonly encountered in natural soil deposits above the ground water table, it is important to systematically study the liquefaction potential of unsaturated soils.

In this chapter, first, the details of the CM4USS (Liu and Muraleetharan 2012a, b) are presented. Model parameters for Nevada sand are then calibrated using available laboratory test results from the literature. The comparisons between the measured and predicted number of cycles to cause initial liquefaction for unsaturated Toyoura sand are then provided to investigate the constitutive model's capability for predicting the liquefaction potential of unsaturated sands at different initial conditions. Then, a series

of undrained, stress-controlled, cyclic triaxial tests for Toyoura sand and Nevada sand are simulated using the calibrated constitutive model to systematically understand the influence of various parameters on liquefaction of unsaturated sands. The main objectives of this chapter are: (1) to provide valuable insight into the behavior of unsaturated sands under cyclic loading; (2) to investigate the effect of initial conditions (degree of saturation, relative density and confining pressure) on the liquefaction of unsaturated sands; and (3) to develop a design chart that can be used to evaluate the liquefaction potential of unsaturated sands.

Portions of this chapter have been published in Zhang et al. (2015) and Zhang et al. (2016).

3.2 CM4USS

3.2.1 Stress Invariants

Effective stress principle plays a significant role in constitutive modeling of saturated and unsaturated soils. In the last few decades, many studies have been done to find effective stress equations based on different theories or experimental observations (Aitchison 1960, Bishop and Donald 1961, Schrefler 1984, Khalili and Khabbaz 1998). For unsaturated soils, most researchers use the Bishop-type effective stress as follows (Bishop 1959):

$$\boldsymbol{\sigma}' = \left(\boldsymbol{\sigma} - p_a \mathbf{I}\right) + \chi s_c \mathbf{I} \;;\; \sigma'_{ij} = \left(\sigma_{ij} - p_a \delta_{ij}\right) + \chi s_c \delta_{ij} \tag{3.1}$$

$$s_c = p_a - p_w \tag{3.2}$$

where, $\boldsymbol{\sigma}'$ is the effective stress tensor, $\boldsymbol{\sigma}$ is the total stress tensor, p_a is pore air pressure, $\mathbf{I}$ is the second-order unit tensor, δ_{ij} is the Kronecker delta, χ is Bishop's parameter, s_c is matric suction and p_w is pore water pressure, σ_{ij} and σ'_{ij} are the total stress and intergranular stress tensors.

Many definitions have been proposed for the Bishop's parameter (Aitchison 1960, Schrefler 1984, Khalili and Khabbaz 1998). Following Wei and Muraleetharan (2002a, 2002b), χ is defined as the volumetric water content n_w in this study. In this dissertation, $\boldsymbol{\sigma}'$ is referred to as the intergranular stress tensor, which is conjugated with the strain tensor $\boldsymbol{\varepsilon}$ of the solid skeleton. The pore water pressure equals the pore air pressure for saturated soils. Therefore, for saturated soils, the matric suction becomes zero and the intergranular stress automatically becomes the Terzaghi's effective stress. It provides a straightforward transition between saturated and unsaturated states. The model uses intergranular stress and matric suction as stress variables and solid skeleton strains and volumetric water content as strain variables to capture the above described hysteresis and couplings.

The stress invariants are defined as follows:

$$\text{First stress invariant: } I = tr(\boldsymbol{\sigma}')/3 \tag{3.3}$$

$$\text{Second stress invariant: } \bar{J} = \left[\frac{1}{2} tr\left(\bar{\mathbf{r}}^2\right)\right]^{1/2} \tag{3.4}$$

$$\text{Third stress invariant: } \bar{S} = \left[\frac{1}{3} tr\left(\bar{\mathbf{r}}^3\right)\right]^{1/3} \tag{3.5}$$

where $\bar{\mathbf{r}} = \left(\frac{\mathbf{s}}{I} - \boldsymbol{\alpha}\right)$, $\mathbf{s} = dev\left(\sigma'_{ij}\right)$ is the deviatoric stress tensor and $\boldsymbol{\alpha}$ is the kinematic hardening parameter.

3.2.2 Hysteretic Soil Water Characteristic Curves

SWCCs play an important role in describing the unsaturated soil behavior. Experimental studies have shown that the SWCCs exhibit hysteresis during wetting and drying cycles. Many models have been proposed to capture the hydraulic hysteresis. In this research a hysteretic model for soil water characteristic curves based on the bounding surface plasticity theory (Liu and Muraleetharan 2006, 2012a) is adopted to describe the hydraulic hysteresis. A schematic representation of SWCC model is shown in Fig. 3.1. The boundary curves are described by the equations proposed by Feng and Fredlund (1999):

$$\text{Wetting: } n_w = \frac{n_{ws} + n_{wr}\left(s_{c0w} / b_2\right)^{d_2}}{1 + \left(s_{c0w} / b_2\right)^{d_2}} \tag{3.6}$$

$$\text{Drying: } n_w = \frac{n_{ws} + n_{wr}\left(s_{c0d} / b_3\right)^{d_3}}{1 + \left(s_{c0d} / b_3\right)^{d_3}} \tag{3.7}$$

where b_2, d_2, b_3 and d_3 are material parameters , n_{ws} and n_{wr} are the saturated and residual volumetric water contents, respectively. s_{c0w} and s_{c0d} are suctions on the wetting and drying bounds, respectively.

Similar to the traditional elastoplastic soil mechanics, the SWCCs model is developed in an incremental form and the increment of the volumetric water content dn_w is assumed to be the additive decomposition of elastic part (dn_w^e) and plastic part (dn_w^p),

$$dn_w = dn_w^e + dn_w^p \tag{3.8}$$

$$ds_c = \Gamma^e dn_w^e \tag{3.9}$$

$$ds_c = \Gamma^p dn_w^p \tag{3.10}$$

where Γ^e and Γ^p are the capillary elastic and plastic moduli, respectively, so the scanning curve can be expressed as:

$$ds_c = \Gamma\left(s_c, n_w\right) dn_w \tag{3.11}$$

$$\frac{1}{\Gamma} = \frac{1}{\Gamma^e} + \frac{1}{\Gamma^p} \tag{3.12}$$

$$\Gamma^p = \Gamma_0^p \left(1 + \frac{H \cdot \delta}{< \delta_{in} - g\delta >}\right) \tag{3.13}$$

where Γ is the tangent capillary modulus in s_c - n_w space; δ is the vertical distance (in suction units) between the current state and its projection on the drying or wetting bounding curve depending on whether the loading is either a drying or a wetting process, as shown in Fig. 3.1; δ_{in} is the value of δ at the initiation of yielding for each drying/wetting process; Γ_0^p is the value of Γ^p when $\delta = 0$, i.e., the value of Γ^p on the bounding curves; < > are the Macaulay brackets; H is a shape hardening parameter, which can be assumed a constant; g can be assumed to be 1 for most soils. The performance of this model to simulate the hysteretic SWCCs has been validated (Miller et al. 2008, Liu 2009, Muraleetharan et al. 2009, Liu and Muraleetharan 2012a).

3.2.3 Elastic Moduli

The elastic moduli, bulk modulus K, shear modulus G are defined as follows:

$$\dot{\varepsilon}_v^e = \frac{\dot{I}}{K},\ \dot{\boldsymbol{\varepsilon}}_q^e = \frac{\dot{\mathbf{s}}}{2G} \tag{3.14}$$

where: ε_v^e and $\boldsymbol{\varepsilon}_q^e$ are the elastic components of volumetric and deviatoric strain of the solid skeleton, respectively, and given by $\varepsilon_v = tr\left(\varepsilon_{ij}\right)$ and $\boldsymbol{\varepsilon}_q = dev\left(\varepsilon_{ij}\right)$, where ε_{ij} is the strain tensor of the solid skeleton, I is the hydrostatic intergranular stress given by $I = \left(\sigma'_{11} + \sigma'_{22} + \sigma'_{33}\right)/3$, $\mathbf{s}$ is the deviatoric stress tensor defined as $\mathbf{s} = dev\left(\sigma'_{ij}\right)$. The

hypoelastic assumption is adopted, which is consistent with the stress-strain behavior of sandy soils, giving

$$K = K_0 \left(\frac{I}{p_{ref}} \right)^{b_1}, \; G = G_0 \left(\frac{I}{p_{ref}} \right)^{d_1} \tag{3.15}$$

where p_{ref} is a reference pressure, which is assumed to be 100 kPa, $K = K_0$ and $G = G_0$ when $I = p_{ref}$, b_1 and d_1 are two model parameters.

3.2.4 Yield, Critical, Bounding and Dilatancy Surfaces

The formulation of CM4USS is developed by introducing four surfaces in the general stress space, namely:

- yield surface (YS), which defines the elastic region
- bounding surface (BS), which corresponds to the bounding (or peak) stress ratio
- critical surface (CS), which corresponds to critical stress ratios
- dilatancy surface (DS), which defines the stress states at which dilatancy (or phase transfer) occurs

Fig. 3.2 illustrates all the surfaces in the general stress space. The yield surface is given by:

$$f\left(\boldsymbol{\sigma}', s_c; \boldsymbol{\alpha}, m\right) = \sqrt{\left(\mathbf{s} - I\boldsymbol{\alpha}\right) : \left(\mathbf{s} - I\boldsymbol{\alpha}\right)} - \sqrt{2/3} m I \sqrt{1 - \left(I / I_0\right)^{\beta}} = 0 \tag{3.16}$$

where $\boldsymbol{\alpha}$ is kinematic hardening parameter which stands for the center of the yield surface. m is the isotropic hardening parameter that defines the size of the yield surface, I_0 is the initial hydrostatic intergranular stress.

The slope of the critical state line of soils in the general stress space is given as a function of the Lode angle, θ

$$\cos 3\theta = \frac{3\sqrt{3}}{2}\left(\frac{\bar{S}}{\bar{J}}\right)^3 \tag{3.17}$$

The bounding surface, dilatancy surface, and critical surface are defined as follows:

$$\boldsymbol{\alpha}_{\theta}^{b,c,d} = \sqrt{2/3}\,\alpha_{\theta}^{b,c,d}\,\mathbf{n} \tag{3.18}$$

$$\alpha_{\theta}^{b} = g\left(\theta, c\right) M_c^c + g\left(\theta, c_b\right) k_c^b < -\psi > -m\sqrt{1 - \left(I / I_0\right)^{\beta}} \tag{3.19}$$

$$\alpha_{\theta}^{d} = g\left(\theta, c\right) M_c^c + g\left(\theta, c_d\right) k_c^d \psi - m\sqrt{1 - \left(I / I_0\right)^{\beta}} \tag{3.20}$$

$$\alpha_{\theta}^{c} = g\left(\theta, c\right) M_c^c - m\sqrt{1 - \left(I / I_0\right)^{\beta}} \tag{3.21}$$

where superscripts b, c and d represent variables for the bounding surface, the critical surface, and the dilatancy surface, respectively; M is the stress ratio on the critical state

line; k_c^b and k_c^d are two model parameters which define the bounding (or peak) and phase transfer (or dilatancy) surfaces on the compression side of the surfaces; c, c_b and c_d are the conversion factors between a quantity in extension and compression ($c = M_e^c / M_c^c$, $c_b = k_e^b / k_c^b$, $c_d = k_e^d / k_c^d$); subscripts c and e stand for variables under compression and extension; $g(\theta, c)$ is given as $g(\theta, c) = 2c / \left((1+c) - (1-c)\cos 3\theta\right)$. $\psi = e - e_c$ is the state parameter and it is defined as the difference between the current void ratio e and the critical void ratio e_c at the same stress state. The formulation of critical state line $e_c = e_{cr} - \lambda\left(I / p_{ref}\right)^{\xi}$ on $e - p'$ plane (Li and Dafalias 2000) is employed in the proposed model, in which e_{cr}, λ and ξ are three model parameters and I is current mean intergranular stress.

3.2.5 Hardening Laws

It's assumed that the effect of suction on the kinematic hardening is only through its contribution to the intergranular stress tensor. The isotropic hardening parameter is only affected by the plastic volumetric strain of soil skeleton and the irrecoverable water content change. So the evolution equations for the kinematic hardening parameter $\boldsymbol{\alpha}$ and isotropic hardening parameter m are given as

$$\dot{\boldsymbol{\alpha}} = < \Lambda > h\left(\boldsymbol{\alpha}_\theta^b - \boldsymbol{\alpha}\right) = < \Lambda > h\mathbf{b} \tag{3.22}$$

$$\dot{m} = c_m \left(1+e_0\right) \dot{\varepsilon}_v^p + c_v \left(\frac{s_c n_w}{p_{ref}} \right)^{\varpi} \dot{n}_w^p \tag{3.23}$$

where e_0 is the initial void ratio, c_v, c_m , ϖ are model parameters. The rate of change of the kinematic hardening parameter $\dot{\boldsymbol{\alpha}}$ is dependent on $\left(\boldsymbol{\alpha}_\theta^b - \boldsymbol{\alpha}\right)$, which is the distance between $\boldsymbol{\alpha}$ and its image on the bounding surface $\boldsymbol{\alpha}_\theta^b$. The function h depending on $|\mathbf{b}:\mathbf{n}|$ was proposed by Dafalias and Popov (1976):

$$h = h_0 \frac{|\mathbf{b}:\mathbf{n}|}{b_{ref} - |\mathbf{b}:\mathbf{n}|} \tag{3.24}$$

in which h_0 is a model parameter and b_{ref} is a reference value which is given as $b_{ref} = 2\sqrt{2/3}\alpha_c^b$.

In order to investigate the coupling effects between the mechanical and hydraulic behavior of unsaturated sands or silts, the evolution of the bounding suctions on the drying bound and wetting bound (s_{c0d} and s_{c0w}) are given below (Muraleetharan et al. 2009)

$$\text{Wetting: } \dot{s}_{c0w} = s_{c0w} \zeta v \dot{\varepsilon}_v^p + \Gamma_{0w}^p \dot{n}_w^p \tag{3.25}$$

$$\text{Drying: } \dot{s}_{c0d} = s_{c0d} \zeta v \dot{\varepsilon}_v^p + \Gamma_{0d}^p \dot{n}_w^p \tag{3.26}$$

where ζ is material parameter, v is the specific volume which is defined in terms of the porosity n as $v = 1/(1-n)$, Γ^p_{0w} and Γ^p_{0d} are the capillary plastic moduli on the wetting and drying bounds, respectively.

3.2.6 Flow Rules and Plastic Moduli

The plastic strain tensor of the soil skeleton and plastic volumetric water content are given as follows:

$$\dot{\boldsymbol{\varepsilon}}^p = <\Lambda> \left(\mathbf{n} + \frac{1}{3} D\mathbf{I} \right) \tag{3.27}$$

$$\dot{n}^p_w = \dot{s}_c / \Gamma^p \tag{3.28}$$

where $\mathbf{n}$ is the deviatoric part of the unit normal to the yield surface, Γ^p is the capillary plastic modulus. Γ^p_0 can be either Γ^p_{0w} or Γ^p_{0d}. Γ^p_{0w} and Γ^p_{0d} are calculated as follows:

$$\Gamma^p_{0w} = -\frac{1}{d_2} \frac{(n_{ws} - n_{wr}) s_c}{(n_{ws} - n_w)(n_w - n_{wr})} \Big|_{s_c = s_{c0w}} \tag{3.29}$$

$$\Gamma^p_{0d} = -\frac{1}{d_3} \frac{(n_{ws} - n_{wr}) s_c}{(n_{ws} - n_w)(n_w - n_{wr})} \Big|_{s_c = s_{c0d}} \tag{3.30}$$

The loading index Λ is given by considering the coupling effects between the intergranular stress and matric suction

$$\Lambda = \frac{1}{K_s^p}\left(\mathbf{n} : \dot{\mathbf{s}} + \frac{\partial f}{\partial I}\dot{I} - \frac{K_m^p}{\Gamma^p}\dot{s}_c \right) \tag{3.31}$$

$$\frac{\partial f}{\partial I} = -\left[\mathbf{n} : \boldsymbol{\alpha} + \sqrt{\frac{2}{3}} m \left(\frac{2 - (2+\beta)(I/I_0)^\beta}{2\sqrt{1-(I/I_0)^\beta}} \right) \right] \tag{3.32}$$

$$K_m^p = \sqrt{\frac{2}{3}} I \sqrt{1-(I/I_0)^\beta}\, c_v \left(\frac{s_c n_w}{p_{ref}} \right)^{\varpi} \tag{3.33}$$

$$K_s^p = hI\mathbf{b} : \mathbf{n} + \sqrt{\frac{2}{3}} I \sqrt{1-(I/I_0)^\beta}\, c_m (1+e_0) D \tag{3.34}$$

where K_s^p and K_m^p are two plastic moduli, representing the two mechanisms related to the yield surface. K_s^p is equivalent to the traditional plastic modulus in the elastoplasticity theory, while K_m^p is a new plastic modulus accounting for the effects of the hydraulic mechanism on the yield surface.

3.2.7 Dilatancy Coefficient

In the general stress space, the dilatancy coefficient, D, is related to the distance from the dilatancy surface $\mathbf{d}$:

$$D = B\left(\boldsymbol{\alpha}_\theta^d - \boldsymbol{\alpha}\right) : \mathbf{n} = B\mathbf{d} : \mathbf{n} \tag{3.35}$$

$$B = B_0\left(1 + < \mathbf{F} : \mathbf{n} >\right) \tag{3.36}$$

$$\dot{\mathbf{F}} = - < \Lambda > c_f < -D > \left(F_{\max}\mathbf{n} + \mathbf{F}\right) \tag{3.37}$$

where: B_0, c_f, $F_{\max}$ are model parameters, $\mathbf{F}$ is fabric tensor.

3.3 Parameter Calibration

The 32 parameters that are used to define the model in the general stress space and their physical meanings are summarized in Table 3.1. Available experimental data for two different sands, Toyoura sand and Nevada sand were used to determine the constitutive model parameters. Toyoura sand is a fine clean sand with a specific gravity G_s of 2.65 and a mean particle size D_{50} of 0.17 mm. The minimum and maximum void ratios are $e_{\min} = 0.6$ and $e_{\max} = 0.97$, respectively. Results of monotonic and cyclic triaxial tests performed on saturated and unsaturated Toyoura sand can be found in the literature (Verdugo and Ishihara 1996, Unno et al. 2008). A single drying SWCC provided for Toyoura sand at $D_r = 60\%$ (Unno et al. 2008) is used as the drying bounding curve and the other SWCCs parameters are assumed. The SWCCs parameters for unsaturated Toyoura sand at $D_r = 40\%$ are assumed to be the same as those at $D_r = 60\%$. Nevada sand is a foundry sand from Simplot Silica Products in Overton, Nevada, with $G_s = 2.67$, $D_{50} = 0.15$ mm, $e_{\min} = 0.54$ and $e_{\max} = 0.97$. The data for

undrained triaxial tests under monotonic and cyclic loading on saturated Nevada sand of two relative densities ($D_r = 40\%$ and $D_r = 60\%$) can be found in Arulmoli et al. (1992). The model parameters related to unsaturated behavior were obtained using a subset of tests on unsaturated Nevada sand available in Liu and Xu (2015) and Xu (2012).

Most of the model parameters can be easily calibrated based on conventional triaxial compression and extension tests results, while other parameters have to be determined using a trial-and-error procedure. The calibration of the model parameters for Toyoura sand can be found in Liu and Muraleetharan (2012b) and Liu (2009). The calibration procedure used for Nevada sand is described here.

(1) Elastic parameters (K_0, G_0 , b_1 , d_1 , and p_{ref}): K_0 is the reference value for the bulk modulus and b_1 is the modulus exponent. These parameters were obtained by matching the low-strain behavior in drained triaxial tests. G_0 is the reference value for shear modulus and d_1 is the modulus exponent; both were calibrated by matching the low-strain behavior in undrained triaxial tests. Parameter p_{ref} is the reference pressure, which is assumed to be 100 kPa.

(2) Critical state parameters (e_{cr} , λ , ξ , M_c^c , and M_e^c): The parameters e_{cr} , λ and ξ define the location of the critical state line in $e - p'$ space, and these parameters were calibrated using monotonic undrained triaxial tests that approached critical state. M_c^c and M_e^c are equal to the stress ratio q / p' at the critical state in triaxial compression and extension, respectively. In this chapter, q, the deviatoric stress is defined as $q = \sigma_1 - \sigma_3$ and p', the effective mean

normal (or confining) stress is defined as $p' = \left(\sigma_1' + 2\sigma_3'\right)/3$, where σ_1 and σ_3 are total principal stresses and σ_1' and σ_3' are principal intergranular stresses given by Eq. (3.1).

(3) Other state parameters (k_c^b , k_c^d , k_e^b , and k_e^d): Calibrating k_c^b , k_c^d , k_e^b , k_e^d requires monotonic compression and extension tests. For example, k_c^b and k_c^d , respectively, can be determined by plotting the bounding (or peak) stress ratio (M_c^b) and the phase transfer (dilatancy) stress ratio (M_c^d) for different compression tests versus the corresponding state parameters (ψ). M_c^b was obtained from drained and undrained compression tests and M_c^d was obtained using undrained compression tests where dilative behavior was observed. Similar procedures were adopted for calibration of k_e^b and k_e^d, corresponding to extension values.

(4) Dilatancy parameter (B_0): Good quality stress-dilatancy data were used to estimate the dilatancy parameter (B_0), i.e., the relationship between the volumetric strain and the axial strain in a constant confining pressure drained test.

(5) Hardening parameters (h_0 , m , c_m , I_0 , β , c_v , and ϖ): The value of h_0 was determined by matching the q - ε_1 curves between the model predictions and the test results in a drained compression test. Parameter m is generally a small value. A reasonable $p'-q$ curve will provide a good estimation of I_0 . Parameter β can be assumed as 20 for most soils. Parameters c_m , c_v and ϖ

were determined by a trial-and-error procedure; however, the influence of these parameters on the predicted behavior was minimal.

(6) Fabric parameters (c_f and $F_{\max}$): Fabric parameters, c_f and $F_{\max}$ were determined through trial-and-error procedure of fitting cyclic data.

(7) SWCCs model parameters (b_2 , d_2 , b_3 , d_3 , Γ^e , g , H , n_{ws} , n_{wr} , and ς): Parameter n_{ws} equals saturated volume fraction of water and n_{wr} is the residual volume fraction of water. Parameters b_2 , d_2 , b_3 , d_3 , n_{ws} and n_{wr} were obtained by matching the bounding curves. A canning curve was used to determine the capillary plastic modulus Γ^e, g and H . g can be assumed to be 1 for most soils. ς was calibrated using a trial-and-error process. SWCCs for Nevada sand at different relative densities available in Xu (2012) were used for calibartion of these parameters.

The calibrated model parameters for Toyoura sand and Nevada sand are summarized in Table 3.2. The constitutive model simulations of unsaturated Toyoura sand under monotonic and cyclic loading can be found in Liu and Muraleetharan (2012b). Liu and Xu (2015) conducted 12 strain-controlled cyclic loading tests on saturated and unsaturated Nevada sand under different relative densities (30% and 70%), effective confining stresses (50 and 200 kPa), and degrees of saturation (90%, 95%, and 100%). In these tests, the saturated soil was first consolidated under a given effective confining pressure. Then, the soil specimen was tuned to the target degree of saturation by applying pore air pressure. Cyclic strain at a frequency of 0.005 Hz was then applied under undrained conditions, and the pore water and air pressures were

measured continuously by water and air pressure transducers. Such slow loading rates are needed to ensure pore pressures come to equilibrium throughout the sample. The effective stress Eq. (3.1) was also used by Liu and Xu (2015); however, they defined the Bishop's parameter χ as the degree of saturation, which is different from the definition used in this chapter i.e., $\chi = n_w$ (volume fraction of water). The effective stresses reported by Liu and Xu (2015) were therefore converted to conform to the definition used in this chapter. For example, an effective confining pressure of 50 kPa reported by Liu and Xu (2015) corresponds to an effective confining pressure of 46.1 kPa according to the definition of effective stress used in this chapter. The model simulations for an undrained, strain-controlled, cyclic triaxial test on unsaturated Nevada sand with 70% relative density, 46.1 kPa effective confining stress and 90% degree of saturation are compared with measurements in Fig. 3.3. Considering the fact that the results of the tests shown in Fig. 3.3 were not used in calibration of the model parameters, the comparisons shown in Fig. 3.3 are very good. As can be seen in Fig. 3.3, the simulated deviatoric stresses in the first few cycles of loading are larger than the measured values. The exact reason for this discrepancy is not known. The simulated deviatoric stresses in later cycles of loading as well as the simulated excess pore air and water pressures, however, match the measured values reasonably well. The model predicts the occurrence of liquefaction in approximately eight loading cycles, which agrees well with the measured number of cycles to liquefaction. These results show that the model simulation provides a satisfactory agreement with the test results.

3.4 Model's Capability for Predicting Liquefaction

Okamura and Soga (2006) studied the factors that influence the liquefaction resistance of unsaturated Toyoura sand through a series of undrained stress-controlled triaxial tests. These test specimens had approximately the same relative densities (D_r = 39 - 43%), but different degrees of saturation ($S_r = 70\%$, 80%, 90%, 96%, 98% and 100%) and initial effective confining pressures (19.6 kPa, 49 kPa and 98 kPa). A Bishop's type effective stress $\boldsymbol{\sigma}' = \left(\boldsymbol{\sigma} - p_a \mathbf{I}\right) + \chi s_c \mathbf{I}$ was also adopted by Okamura and Soga (2006), but χ was defined as unity in their work. The effective stress used by Okamura and Soga (2006) was converted to the intergranular stress defined in this chapter, i.e., the values of 49 kPa and 98 kPa were converted to 46.5 kPa and 95.5 kPa, respectively. In this research the predicted results are compared with undrained stress-controlled cyclic tests results at different degrees of saturation (90%, 98%) and initial effective confining pressures (46.5 kPa, 95.5 kPa) for Toyoura sand at 40% relative density. The initial conditions and their range of values are shown in Table 3.3. The initial liquefaction of unsaturated Toyoura sand is defined following the reference (Okamura and Soga 2006) on the basis of a soil specimen deforming to 5% double amplitude (DA) axial strain.

Fig. 3.4 shows typical model simulations for an undrained stress-controlled triaxial test on unsaturated Toyoura sand at $D_r = 40\%$, $S_r = 98\%$, $p_0' = 95.5\,\text{kPa}$, and $q = \pm 41$ kPa. The initial matric suction is 4.67 kPa. It can be observed that both pore water pressure and pore air pressures increase with the number of cycles. The matric

suction becomes nearly zero at about 21st cycles at which point the effective confining pressure also becomes zero. When the effective confining pressure becomes zero, the axial strain starts to increase significantly.

Fig. 3.5 compares predicted and measured number of cycles to cause liquefaction (double amplitude axial strain = 5%) for undrained stress-controlled cyclic tests on unsaturated Toyoura sand at $D_r = 40\%$ and $p_0' = 95.5\,\text{kPa}$ under two degrees of saturation of S_r = 90% and 98%. The CSR is defined as the ratio of one half of the applied deviatoric stress (q) to the initial effective confining pressure, p_0' , i.e., $\text{CSR} = q/\left(2p_0'\right)$. It can be observed from Fig. 3.5 that a good match is obtained between the predicted and measured results when $S_r = 98\%$ at low CSR, while there is a small discrepancy at high CSR. For the sands at $S_r = 90\%$, although there are about 2 cycles difference between the measured and predicted results, in general the model predicts the number of cycles to cause liquefaction well. The results clearly demonstrate the capabilities of this model to capture the liquefaction potential of unsaturated sands at various degrees of saturation. Furthermore, it is obvious that the liquefaction potential is influenced by the degree of saturation, i.e., the lower the degree of saturation, the lower liquefaction potential of unsaturated sands.

Comparisons between the predicted and measured number of cycles to cause liquefaction for undrained stress-controlled cyclic tests on unsaturated Toyoura sand at $D_r = 40\%$, $p_0' = 46.5$ kPa, and $S_r = 98\%$ under cyclic stress ratios of 0.18, 0.19, 0.23 and 0.25 are shown in Fig. 3.6. It can be deduced from Fig. 3.6 that the predicted number of cycles to cause liquefaction under both high and low CSRs at low effective

confining pressures compares quite well with the measured ones. From Fig. 3.5 and Fig. 3.6, the liquefaction resistances of unsaturated Toyoura sands at $D_r = 40\%$ and $S_r = 98\%$ are obtained and plotted in Fig. 3.7. The liquefaction resistance is defined here as the CSR required to cause 5% double amplitude axial strain in 20 cycles. The overall performance of the model on predicting the liquefaction resistance of unsaturated sands under different effective confining pressure is satisfactory. It is of interest to note that the increase in effective confining pressure results in more resistant to liquefaction.

3.5 Constitutive Model Simulations

To study the influence of initial conditions on liquefaction potential of unsaturated sands, various degrees of saturation (75%, 85%, 90%, 95% and 98%), relative densities (30%, 50% and 70%) and initial effective confining pressures (50 kPa and 100 kPa) were considered (Table 3.4) for both Toyoura and Nevada sand. Various applied deviatoric stresses in the stress controlled cyclic test simulations are also shown in Table 3.4.

In all the simulations, the initial pore water pressure was assumed to be equal to 98 kPa. The initial suction was obtained based on the degree of saturation and the drying boundary curve. All simulations were conducted as undrained, i.e., the drainage of both the pore air and pore water were prevented during cyclic loading. The initial liquefaction of unsaturated soils in triaxial tests occurs when the effective mean stress reaches a value of zero. Since this definition is more commonly used than that in

Okamura and Soga (2006), it will be employed as the liquefaction criteria. Unfortunately, this condition is difficult to precisely discern in testing and simulations. In this research, the soil is assumed to have reached initial liquefaction when the effective mean stress reaches a value of 10% of the initial value, i.e., $0.1p_0'$. The liquefaction resistance is defined as the cyclic stress ratio that leads to initial liquefaction in 15 cycles, the number of significant cycles for a magnitude 7.5 earthquake (Seed and Idriss 1982).

3.6 Results and Discussion

A typical simulation of an undrained, cyclic, stress-controlled test using the constitutive model is shown in Fig. 3.8 (Toyoura sand with $D_r = 50\%$, $S_r = 95\%$, $p_0' = 100$ kPa and $q = \pm 60$ kPa). It can be observed that both pore water and pore air pressures increase with the number of cycles. The matric suction becomes nearly zero in approximately 19 cycles and the axial strain starts to increase significantly. Based on the definition given earlier, the specimen reaches initial liquefaction in 18.5 cycles as shown in Fig. 3.8. Typical simulation results of an undrained, cyclic, stress-controlled test at $S_r = 65\%$ are shown in Fig. 3.9. It can be seen that this sample did not reach liquefaction. Therefore, it can be concluded that unsaturated Toyoura sand with $D_r = 50\%$ and $p_0' = 100$ kPa is not susceptible to liquefaction if its degree of saturation is lower than a value between 75% and 65% for a CSR = 0.3. Effects of initial degree of saturation, relative density, and confining pressure on liquefaction are discussed below. Although simulations were conducted for Toyoura sand and Nevada sand for all the

cases listed in Table 3.4, only typical results are shown below. Results from all simulations are later combined into a design chart.

3.6.1 Effect of Degree of Saturation

For Nevada sand with a relative density of 50% and an initial effective confining stress of 100 kPa, the number of cycles required to cause initial liquefaction for various CSRs at a given degree of saturation are shown in Fig. 3.10. The following can be observed from Fig. 3.10: (1) for a given CSR, the number of cycles required to cause initial liquefaction increases significantly as the degree of saturation reduces; and (2) a slight decrease in degree of saturation when the initial degree of saturation is high (e.g. 98% to 95%) results in a significant increase in number of cycles to cause initial liquefaction for a given CSR.

The liquefaction resistance can be read from the curves shown in Fig. 3.10 (CSR required to cause liquefaction in 15 cycles) and are depicted as a function of degree of saturation in Fig. 3.11 for both Nevada sand and Toyoura sand. It can be seen form Fig. 3.11 that the lower the degree of saturation, the higher the liquefaction resistance. The liquefaction resistance at $S_r = 75\%$ is approximately 170% times higher than that at $S_r = 98\%$. It can also be seen from Fig. 3.11 that the effect of the degree of saturation on the liquefaction resistance is more pronounced for high values of degree of saturation. For example, for Toyoura sand, a 3% drop (from 98% to 95%) in degree of saturation results in about 25.3% increase in the liquefaction resistance, while there is only 8.8% increase in liquefaction resistance when the degree of saturation changes

from 85% to 75%. Furthermore, the liquefaction resistance values of Toyoura sand and Nevada sand are similar.

3.6.2 Effect of Density

Typical simulation results showing the effect of density are depicted in Fig. 3.12. As expected, for a given cyclic stress ratio, number of cycles to cause initial liquefaction increases with density. The number of cycles to cause initial liquefaction at a $\mathrm{CSR} = 0.3$ for $D_r =$ 30%, 50% and 70% are approximately 7, 11.5 and 19.5, respectively. Liquefaction resistance values obtained from Fig. 3.12 and similar curves not shown here are given in Fig. 3.13. Increases of 11.4% and 7.6% in liquefaction resistance occur when relative density changes from 30% to 50% and 50% to 70%, respectively, at 85% degree of saturation. At a relative density of 50%, the liquefaction resistance at degrees of saturation of 95%, 90%, 85% and 75%, respectively, is 30%, 47%, 61% and 77% more than that at 98% degree of saturation. It can be concluded from Fig. 3.13 that for all degrees of saturations, liquefaction resistance increases with density.

3.6.3 Effect of Confining Pressure

Typical simulation results showing the effect of initial effective confining pressure are given in Fig. 3.14. For an unsaturated sample with a same degree of saturation and relative density, the number of cycles to cause initial liquefaction

increases as the initial effective confining pressure increases. The variations of liquefaction resistance with the initial effective confining pressure for unsaturated Nevada sand at $D_r = 30\%$ under different degrees of saturation values are shown in Fig. 3.15. Fig. 3.15 shows that, for all degrees of saturation values, the liquefaction resistance increases with an increase in initial effective confining pressure. The liquefaction resistance increases approximately 10-20% as the initial effective confining pressure increases from 50 kPa to 100 kPa. It can be concluded that liquefaction resistance is significantly influenced by the initial effective confining pressure. Unsaturated soils under larger effective confining pressures are expected to be more stable than those with smaller effective confining pressures at the same degree of saturation and relative density.

3.6.4 Design Chart

The results presented in the previous sections suggest that the liquefaction potential of unsaturated sands is influenced by the initial conditions (density, degree of saturation, and effective confining pressure). Based on the results presented earlier, boundary curves between liquefied and non-liquefied samples can be obtained. A typical boundary curve is shown in Fig. 3.16. There is about 7% difference in the value of liquefaction resistance between Toyoura sand and Nevada sand if the initial conditions are kept the same and therefore average values were used to obtain the boundary curve shown in Fig. 3.16. All such boundary curves obtained are shown in

Fig. 3.17. This design chart provides the boundary that separates liquefaction from no-liquefaction occurrence for the following range of parameters:

- Degree of saturation, S_r = 75%, 85%, 90%, 95%, and 98%;
- Relative density, D_r = 30%, 50% and 70%;
- Effective confining pressure, p_0' = 50 kPa and 100 kPa;

This design chart distinctly indicates that the higher the degree of saturation and lower the effective confining pressure and relative density, the easier the unsaturated sands will liquefy. It can be used to evaluate the liquefaction potential of unsaturated sands. Similar to the procedure used by Seed (1983), by taking the ratio of liquefaction resistance at an effective confining pressure to that obtained at a reference effective confining pressure of 100 kPa under the same degree of saturation and relative density, a correction factor for effective confining pressure can be developed to simplify the design chart shown in Fig. 3.17. This correction factor, K_σ, is given as

$$K_\sigma = \frac{CRR_\sigma}{CRR_1} \tag{3.38}$$

where CRR_σ is the liquefaction resistance at a given effective confining pressure , CRR_1 is the liquefaction resistance at a reference effective confining pressure of 100 kPa. Fig. 3.18 shows the relationship between degree of saturation and K_σ at an effective confining pressure of 50 kPa.

3.7 Summary

In this chapter, a coupled hydro-mechanical elastoplastic constitutive model is presented and its capability to simulate the cyclic behavior of unsaturated sands is investigated through comparisons between the model simulations and a series of undrained cyclic tests results on unsaturated Toyoura sand. A series of undrained stress-controlled cyclic triaxial tests on unsaturated Toyoura sand and Nevada sand were simulated using a calibrated, coupled, hydro-mechanical, elastoplastic constitutive model. The simulation results confirm that liquefaction can indeed occur in unsaturated sands. Based on the comparisons and simulation results, following conclusions can be reached.

(1) The model's ability to predict the number of cycles to cause liquefaction for unsaturated sands is generally satisfactory.

(2) The liquefaction resistance increases with a decrease in the initial degree of saturation and increases in relative density and initial effective confining pressure. When the degree of saturation is near 100%, the effect of the degree of saturation on the liquefaction resistance is more significant.

(3) The differences in liquefaction resistance values between Toyoura sand and Nevada sand under similar initial conditions are small and therefore the results can be combined to develop a liquefaction potential design chart for sands that separates liquefaction from no-liquefaction. The degree of saturation, relative density and initial effective confining pressure are incorporated into this design chart.

Table 3.1 Summary of model parameters and their physical meanings

Symbol	Physical meaning
Elastic parameters	
K_0	Low-strain bulk modulus
G_0	Low-strain shear modulus
b_1	Bulk modulus exponent
d_1	Shear modulus exponent
Critical state parameters	
$e_{cr,}$ λ, ξ	Location of critical state line in e - p' space
M_c^c	Critical state stress ratio in triaxial compression
M_e^c	Critical state stress ratio in triaxial extension
State dependence parameters	
k_c^b	Effect of ψ on the position of BS in triaxial compression
k_c^d	Effect of ψ on position of DS in triaxial compression
k_e^b	Effect of ψ on the position of BS in triaxial extension
k_e^d	Effect of ψ on position of DS in triaxial extension
Hardening parameters	
m	Radius of the yield surface
h_0	Evolution of kinematic hardening
c_m	Evolution of isotropic hardening due to ε_v^p
I_0	Effective confining stress at the tip of yield surface
β	Power exponent
c_v	Evolution of isotropic hardening due to n_w^p
ϖ	
ζ	Evolution of the bounding suctions due to ε_v^p
Dilatancy parameters	
B_0	Dilatancy constant
Fabric parameters	
c_f	Evolution of fabric tensor
F_{max}	Limit size of fabric tensor
SWCCs parameters	
b_2	Location of bounding wetting curve in n_w - s_c space
d_2	
b_3	Location of bounding drying curve in n_w - s_c space
d_3	
Γ^e	Capillary elastic modulus (kPa)
H	Hardening shape parameter
n_{ws}	Saturated volumetric water content
n_{wr}	Residual volumetric water content

Table 3.2 Constitutive model parameters for Toyoura sand and Nevada sand

Parameter list	Toyoura sand	Nevada sand		
	D_r = 30%,50%,70%	D_r = 30%	D_r = 50%	D_r = 70%
K_0 (kPa)	20000		60000	
G_0 (kPa)	10000		30000	
b_1	0.5		0.6	
d_1	0.5		0.6	
e_{cr}	0.935		0.82	
λ	0.019		0.011	
ξ	0.7		0.7	
M_c^c	1.29		1.26	
M_e^c	1.29		1.26	
k_c^b	0.5		2.4	
k_c^d	3.0		2.2	
k_e^b	2.0		1.7	
k_e^d	0.07		0.08	
h_0	500		1400	
m	0.40		0.40	
c_m	0.0		0.0	
I_0 (kPa)	5000		3000	
β	20		20	
c_v	0.5		0.5	
ϖ	10		10	
ς	10		10	
B_0	0.5		0.7	
c_f	100		500	
$F_{\max}$	100		1.0	
b_2	2.3	4.9	2.6	2.9
d_2	1.05	3.2	2.2	2.3
b_3	4.0	8.1	6.5	6.8
d_3	1.3	5.3	5.2	5.4
Γ^e (kPa)	-100	-220	-190	-200
H	7.0	5.0	4.0	9.0
n_{ws}	0.95	0.456	0.43	0.401
n_{wr}	0.03	0.07	0.08	0.072

Table 3.3 Initial conditions and their range of values for undrained tests of Toyoura sand

Relative density D_r (%)	Degree of saturation S_r (%)	Effective confining pressure p'_0 (kPa)	Deviatoric stress q * (kPa)
40	98	95.5	41, 45, 50
		46.5	18, 21, 24
	90	46.5	60, 65, 70

* In the constitutive model simulation, the value range of deviatoric stress is $\pm q$.

Table 3.4 Parameters selected for undrained stress-controlled cyclic test simulations

Relative density D_r (%)	Degree of saturation S_r (%)	Initial effective confining stress p'_0 (kPa)	Deviatoric stress q (kPa)
30, 50, 70	98	50	±20, ±30, ±40
		100	±40, ±60, ±80
	95	50	±20, ±30, ±40
		100	±40, ±60, ±80
	90	50	±20, ±25, ±30, ± 40, ±45
		100	±40, ±50, ±60, ±80, ±90
	85	50	±20, ±25, ±30, ±40
		100	±40, ±60, ±70, ±80, ±90
	75	50	±20, ±30, ±35, ±40
		100	±60, ±70, ±80, ±90

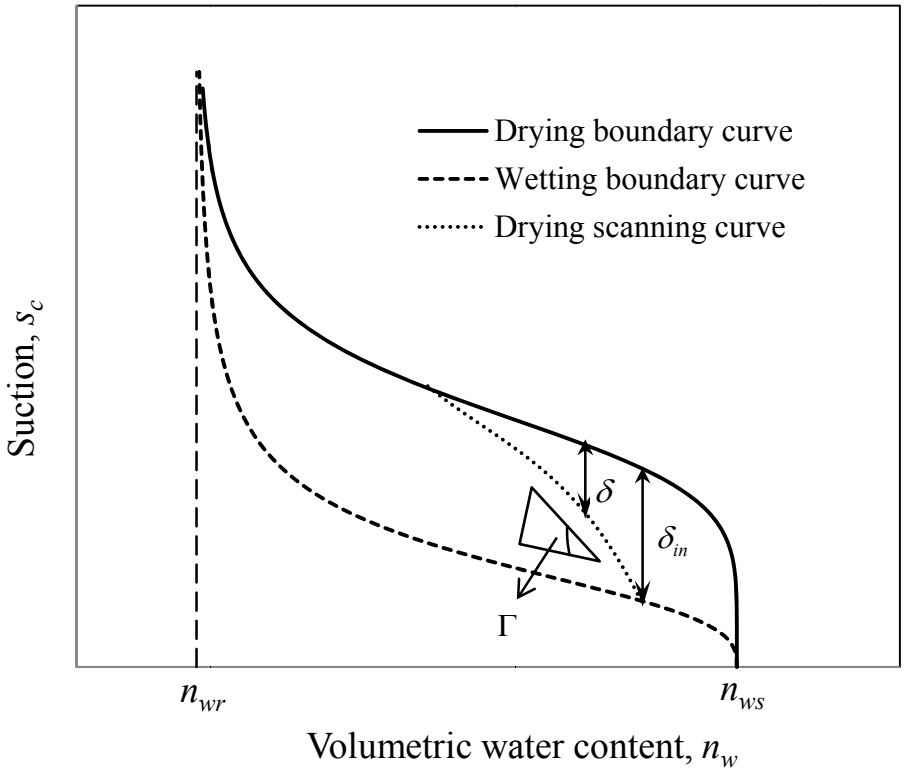

Fig. 3.1 Soil water characteristic curves including hydraulic hysteresis

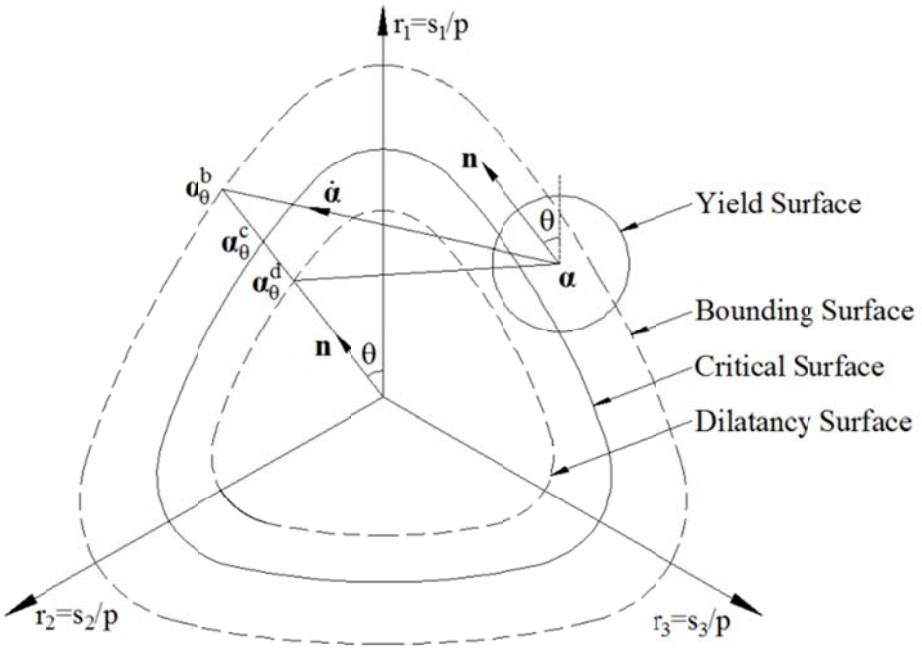

Fig. 3.2 Schematic illustration of the yield, bounding, critical, and dilatancy surfaces in the general stress space (after Taiebat and Dafalias 2008)

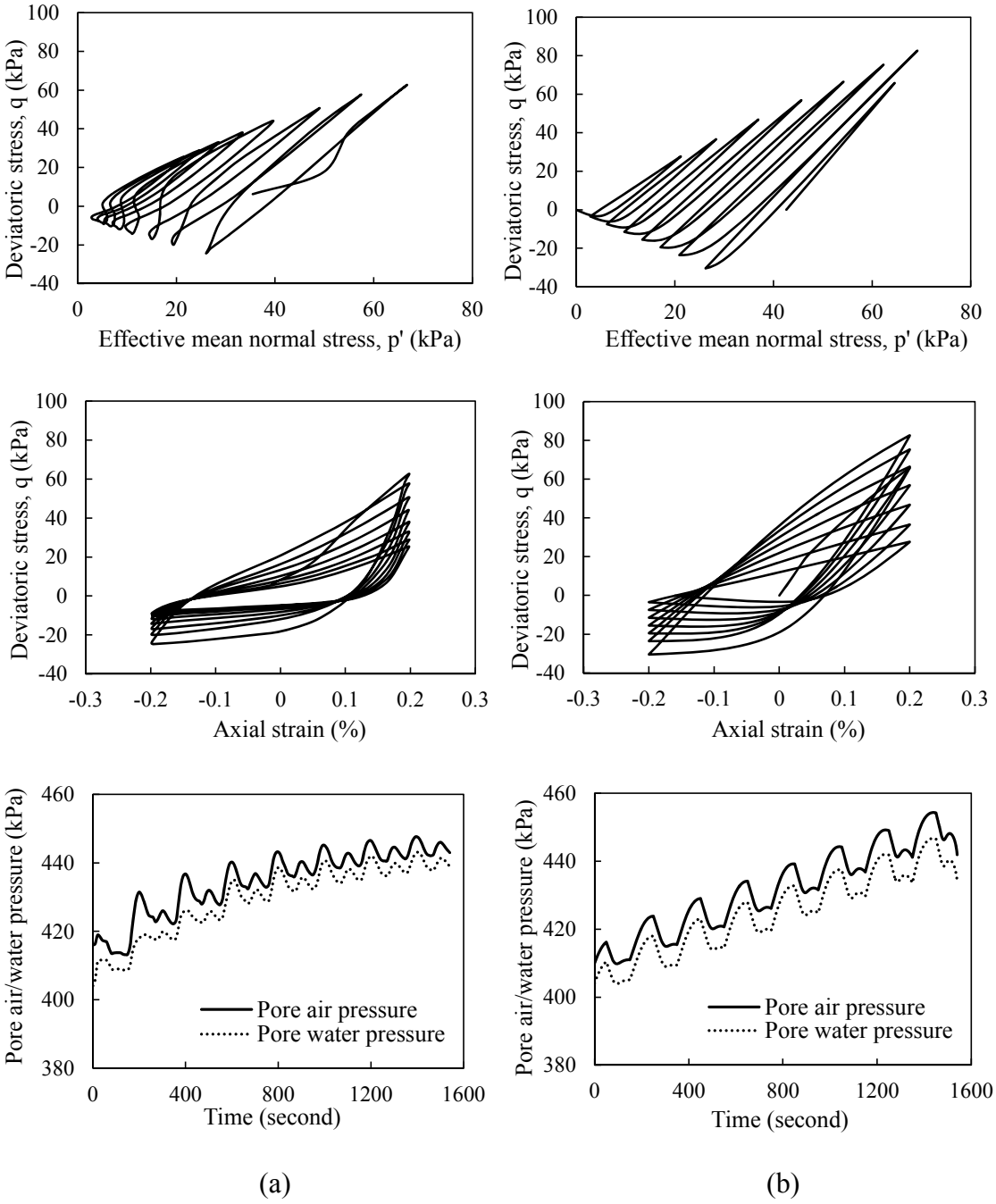

Fig. 3.3 Comparisons of (a) test results and (b) model simulations for an undrained strain-controlled cyclic triaxial test on unsaturated Nevada sand ($D_r = 70\%$, $S_r = 90\%$ and $p_0' = 46.1$ kPa) (test results after Xu 2012)

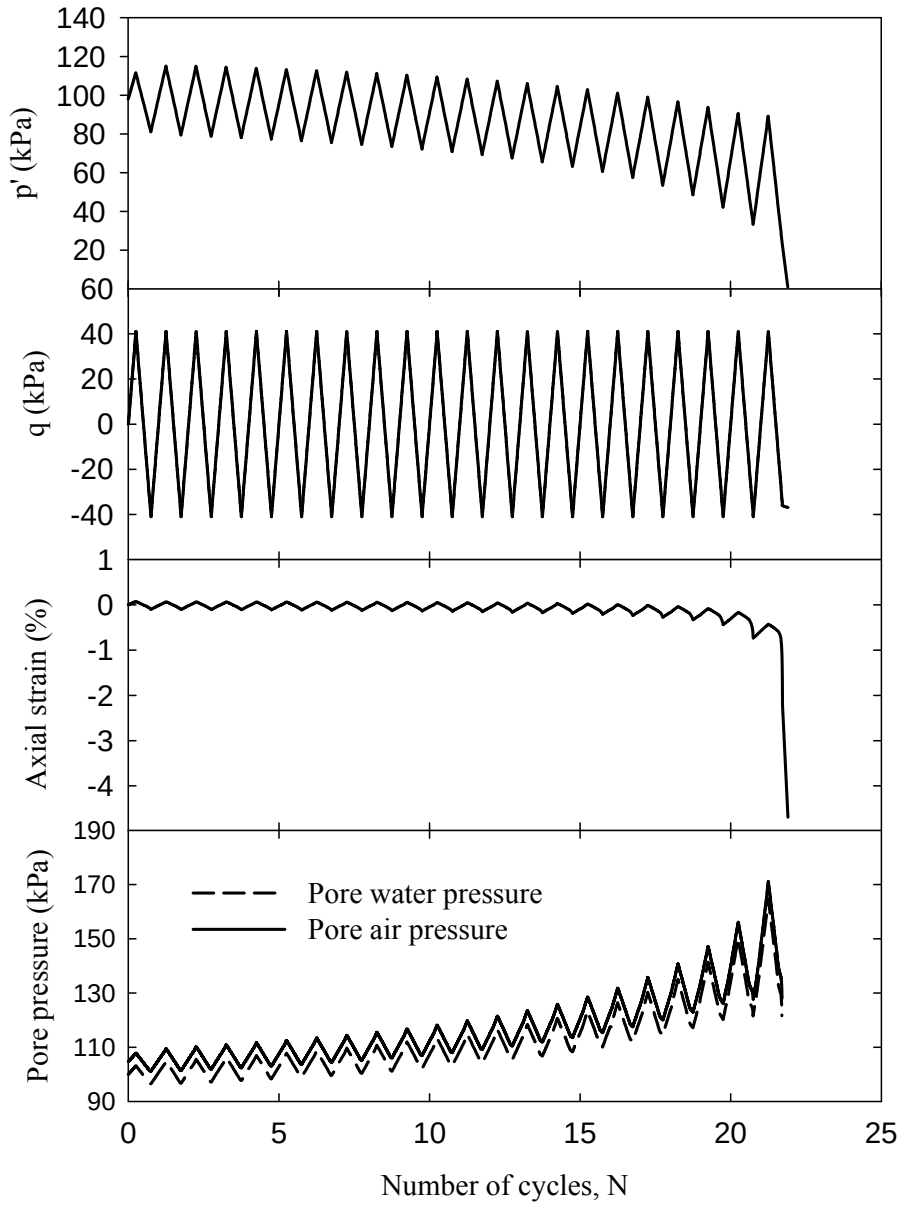

Fig. 3.4 Predicted result of an undrained stress-controlled triaxial test on unsaturated Toyoura sand at D_r = 40%, S_r = 98%, p'_0 = 95.5 kPa, and q = ±41 kPa

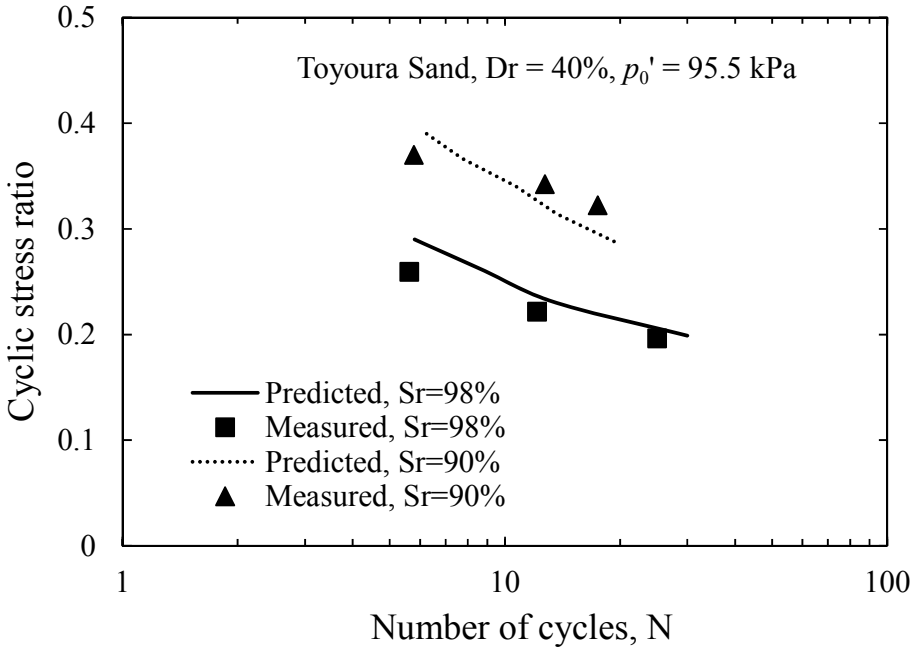

Fig. 3.5 Comparisons between the measured and predicted number of cycles to cause liquefaction for undrained stress-controlled cyclic tests on unsaturated Toyoura sand at D_r = 40% and p'_0 = 95.5 kPa under degrees of saturation of S_r = 98% and 90% (measured results are after Okamura and Soga 2006)

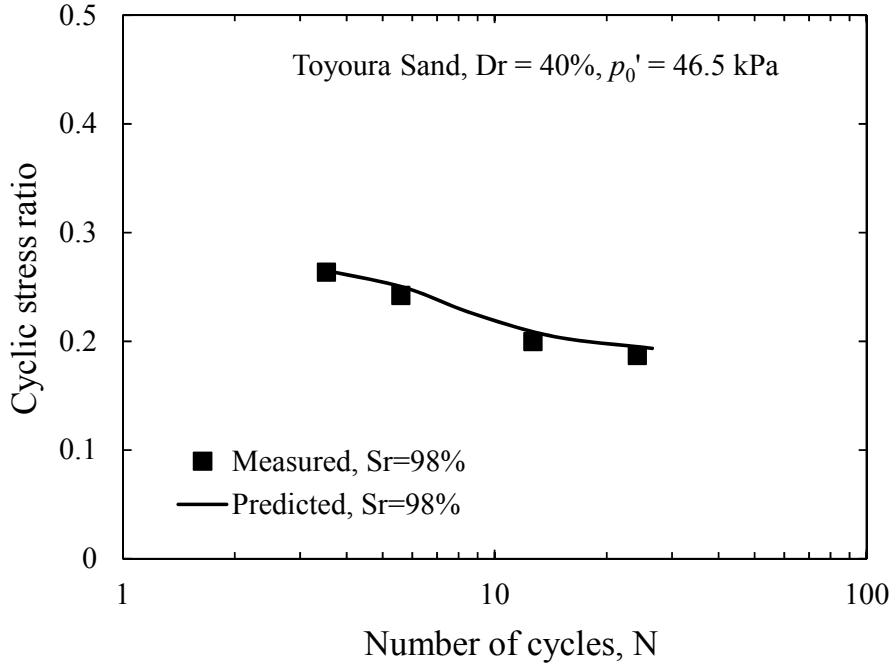

Fig. 3.6 Comparisons between the measured and predicted number of cycles to cause liquefaction for undrained stress-controlled cyclic tests on unsaturated Toyoura sand at D_r = 40% and S_r = 98% (measured results are after Okamura and Soga 2006)

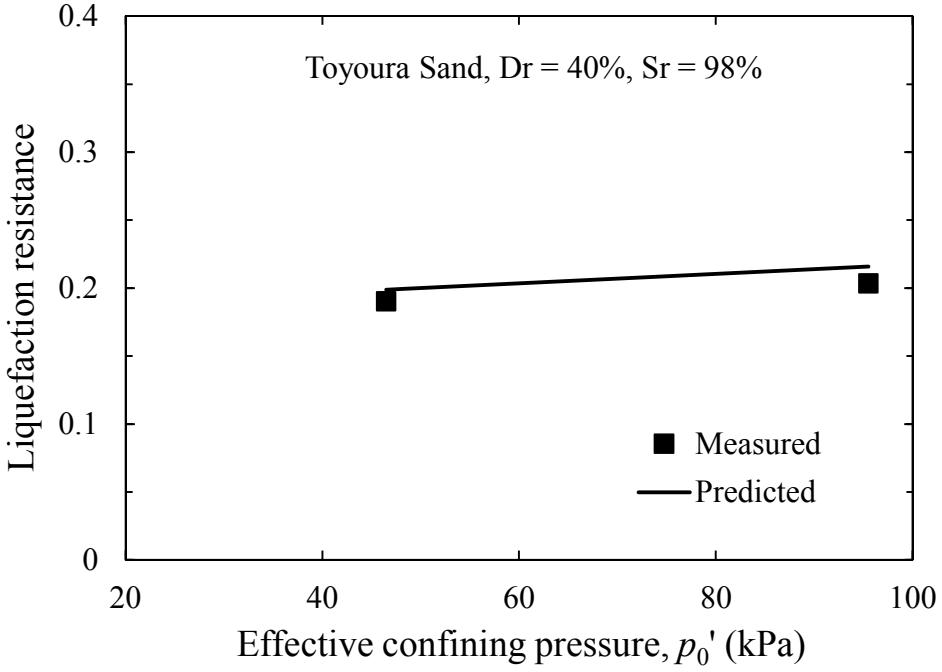

Fig. 3.7 Comparisons between the measured and predicted liquefaction resistance for undrained stress-controlled cyclic tests on unsaturated Toyoura sand at D_r = 40% and S_r = 98% under effective confining pressures of 46.5 kPa and 95.5 kPa (measured results are after Okamura and Soga 2006)

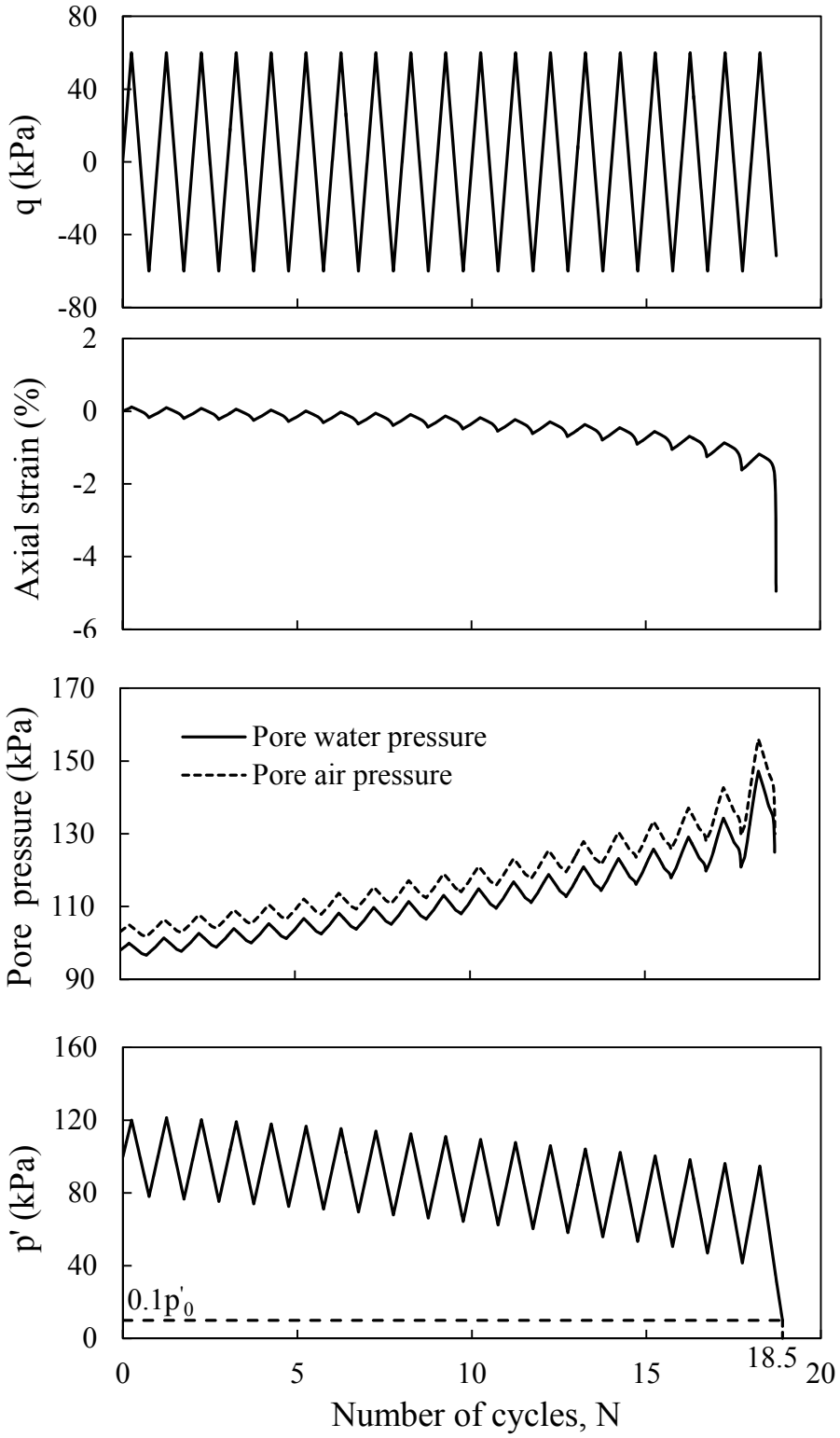

Fig. 3.8 Typical constitutive model simulation of an undrained stress-controlled cyclic test (Toyoura sand with $D_r = 50\%$, $S_r = 95\%$, $p_0' = 100$ kPa and $q = \pm 60$ kPa)

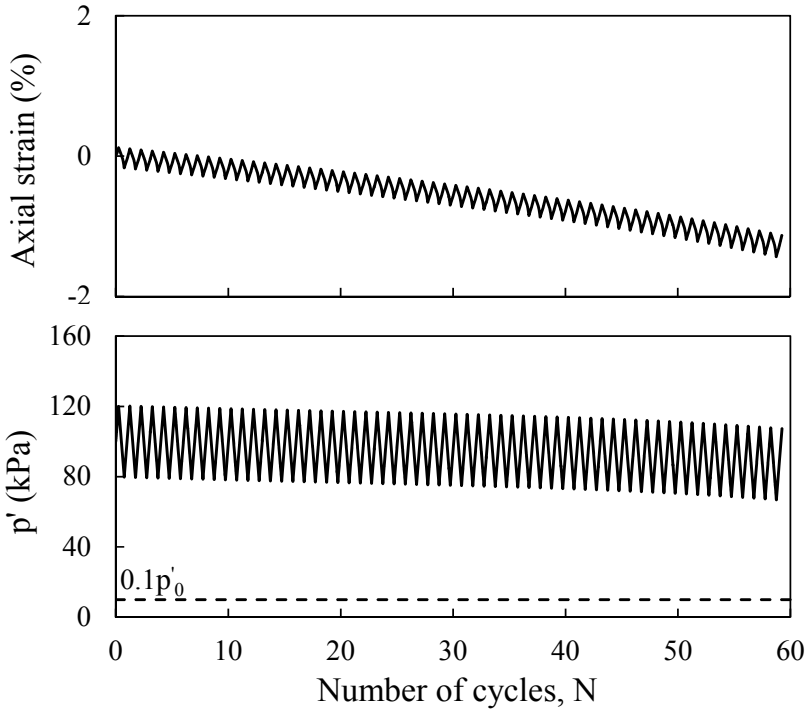

Fig. 3.9 Typical simulation results of an undrained stress-controlled cyclic test (Toyoura sand with $D_r = 50\%$, $S_r = 65\%$, $p_0' = 100$ kPa and $q = \pm 60$ kPa)

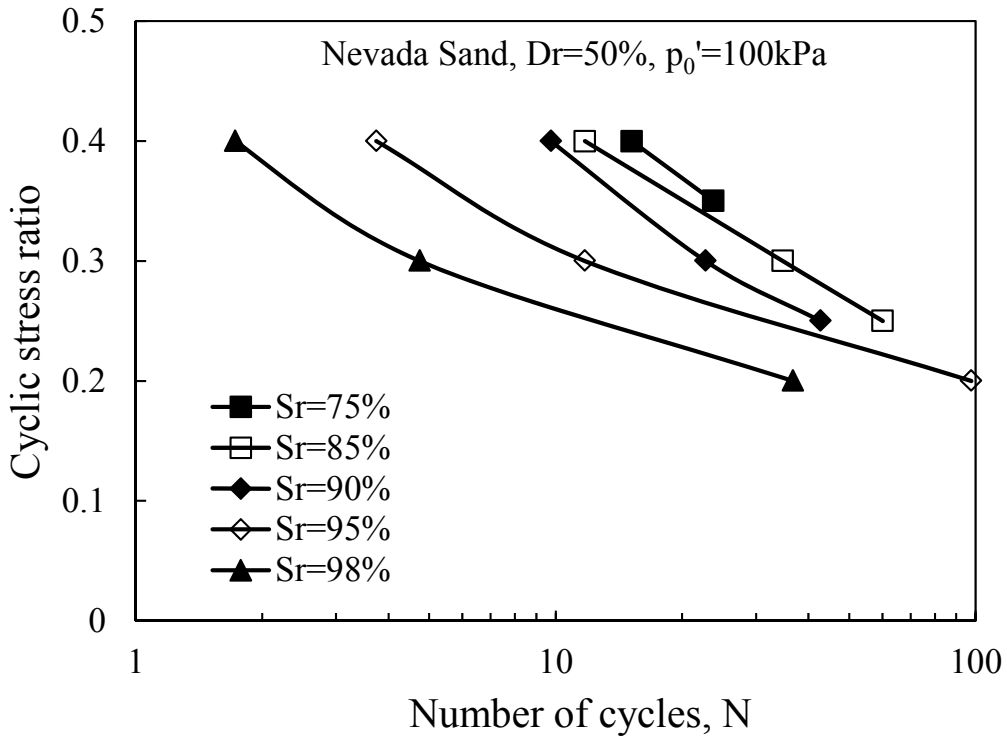

Fig. 3.10 Relationship between cyclic stress ratio and number of cycles to cause initial liquefaction for different degrees of saturation for Nevada sand

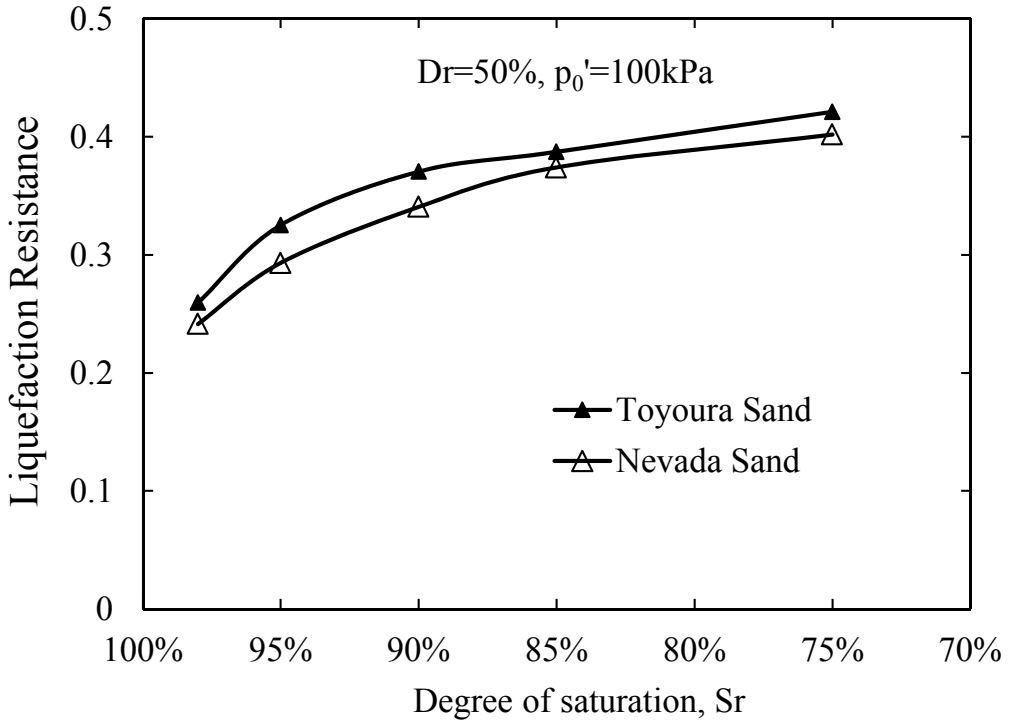

Fig. 3.11 Effect of degree of saturation on liquefaction resistance

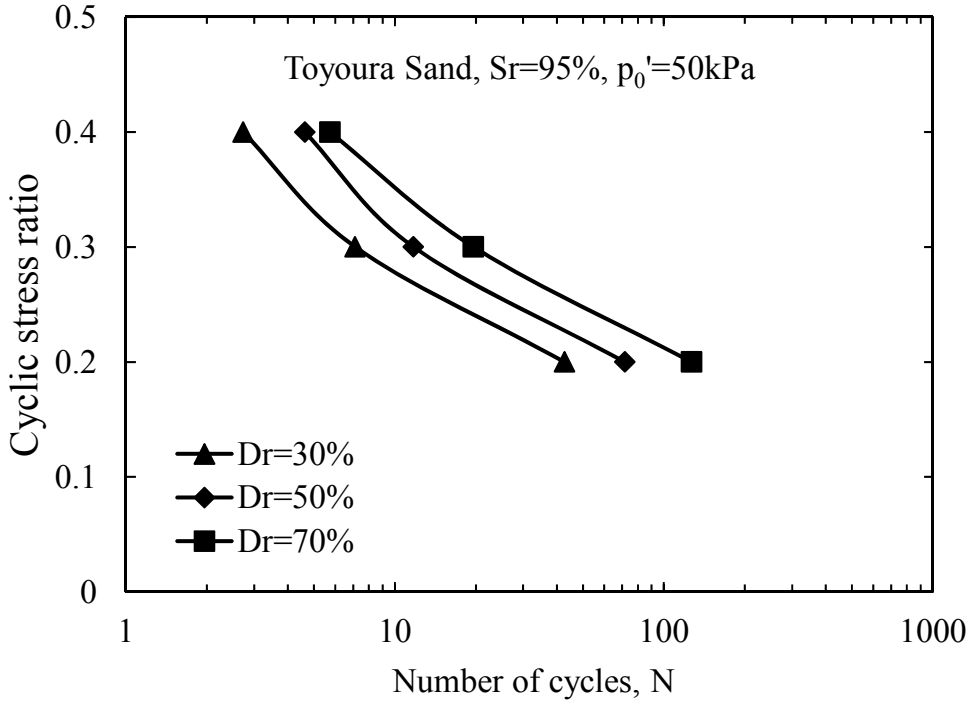

Fig. 3.12 Relationship between cyclic stress ratio and number of cycles to cause liquefaction for Toyoura sand at different relative densities

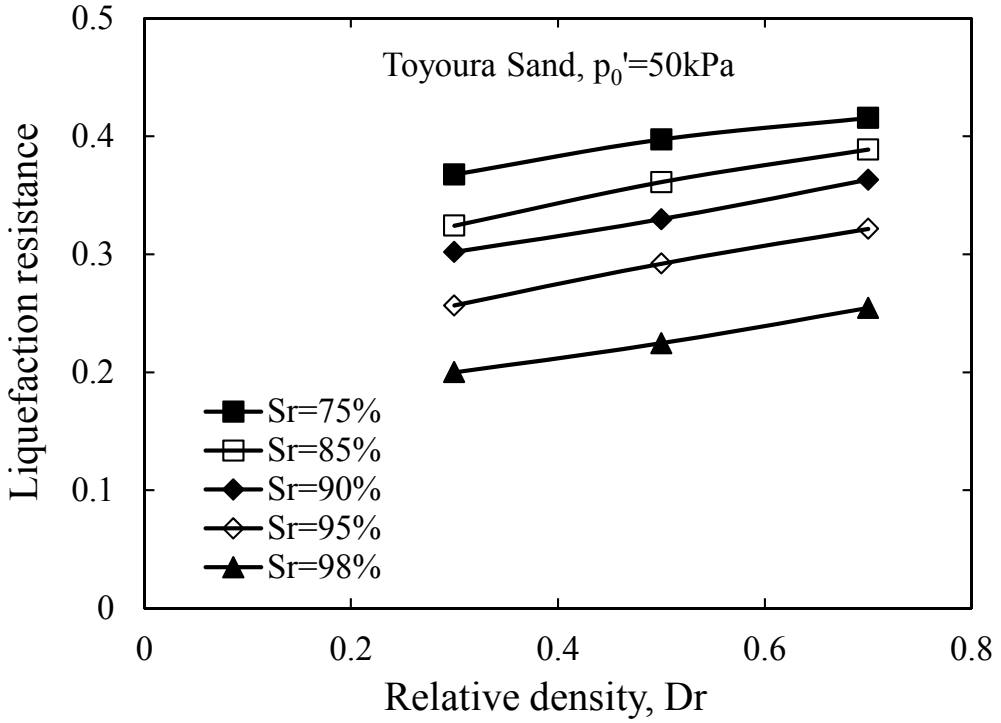

Fig. 3.13 Effect of relative density on liquefaction resistance

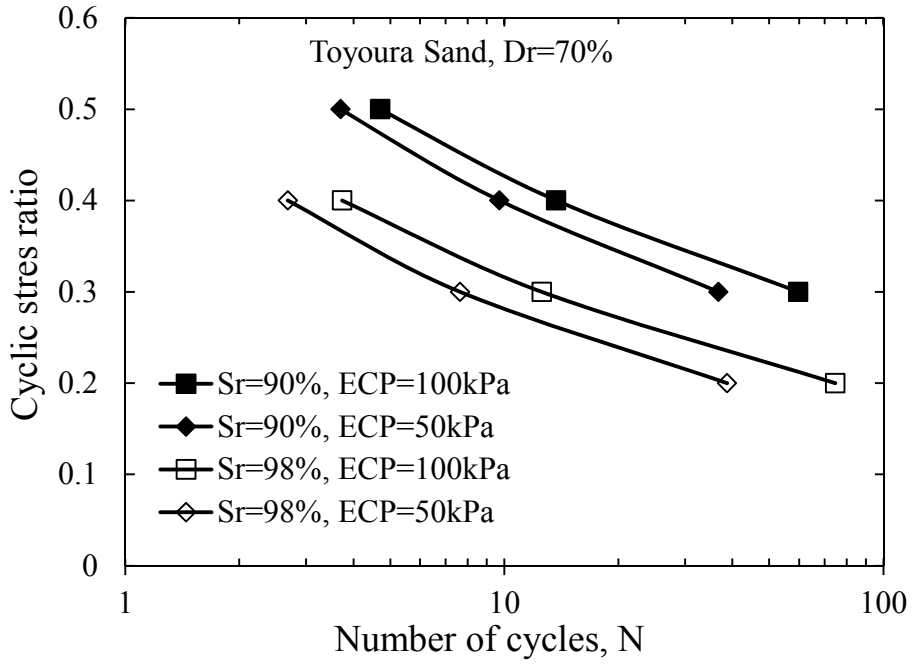

Fig. 3.14 Relationship between cyclic stress ratio and number of cycles to cause initial liquefaction for Toyoura sand under different initial effective confining pressures

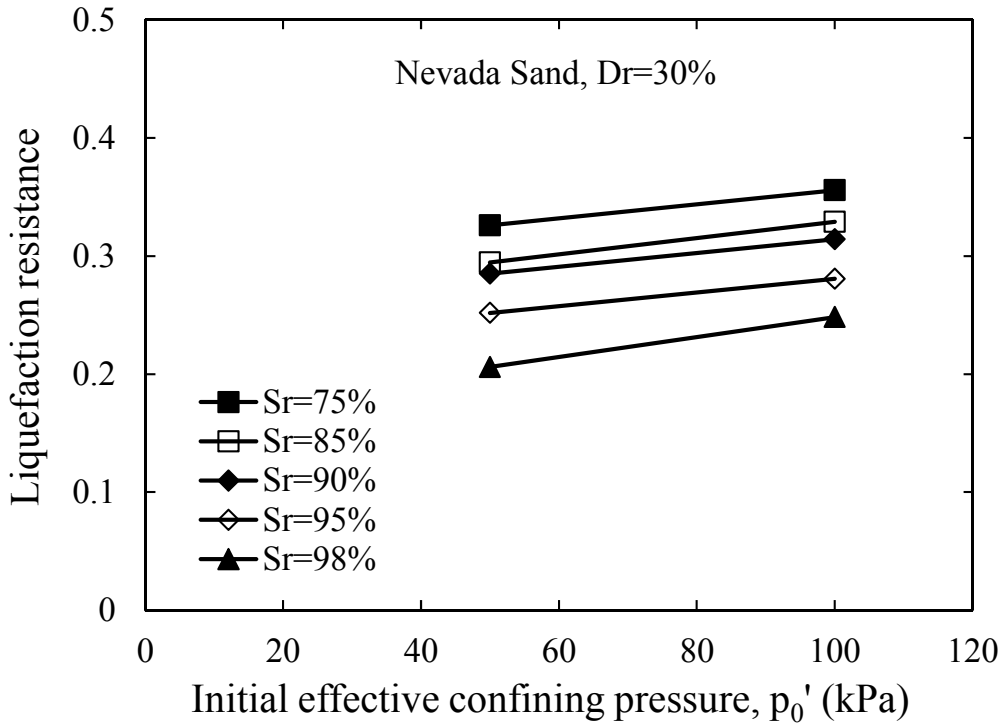

Fig. 3.15 Effect of initial effective confining pressure on liquefaction resistance

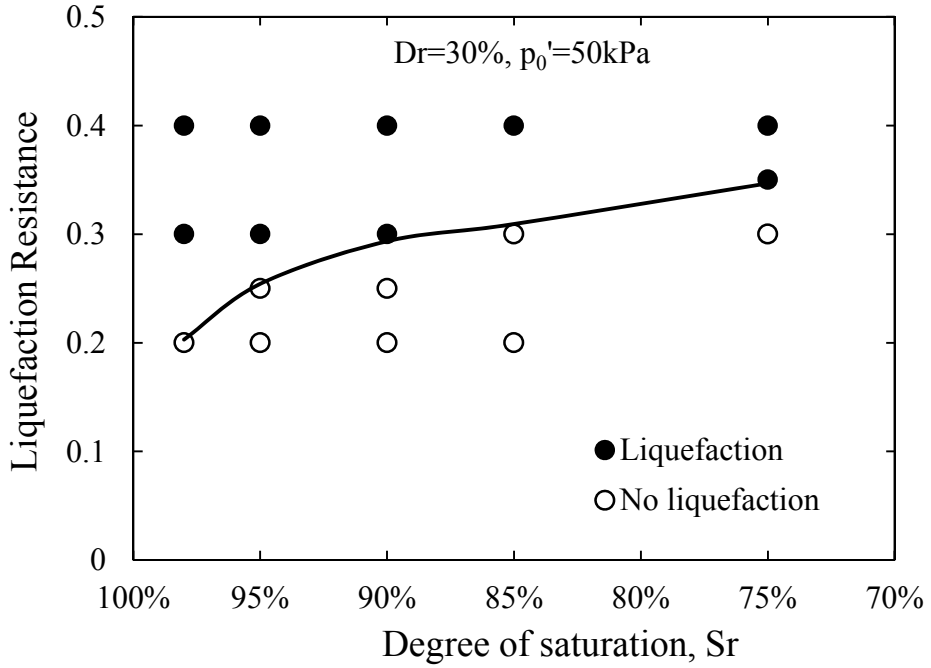

Fig. 3.16 Boundary curve for liquefaction of unsaturated sands

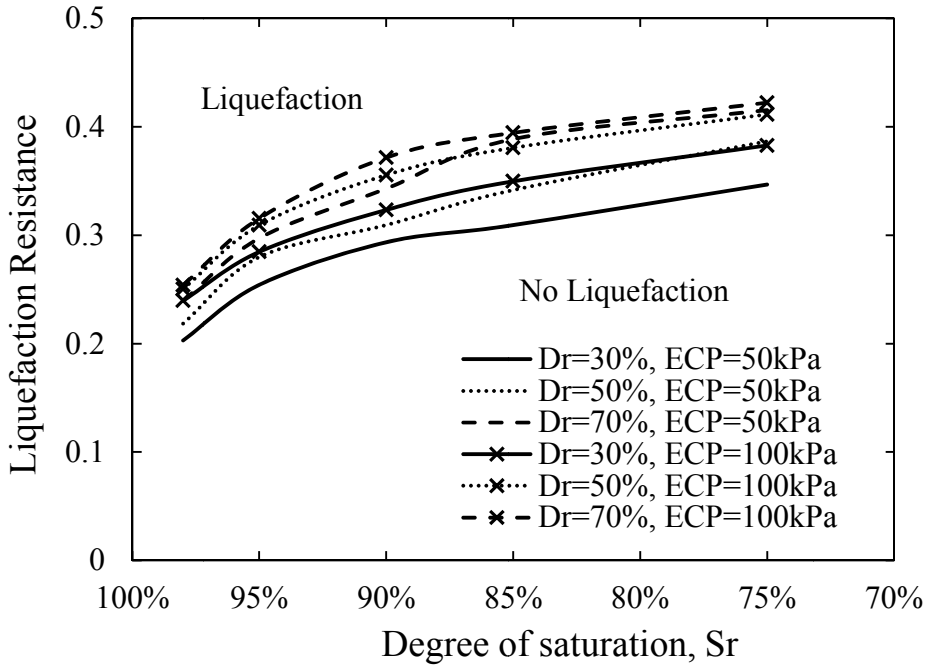

Fig. 3.17 Design chart for liquefaction potential evaluation of unsaturated sands

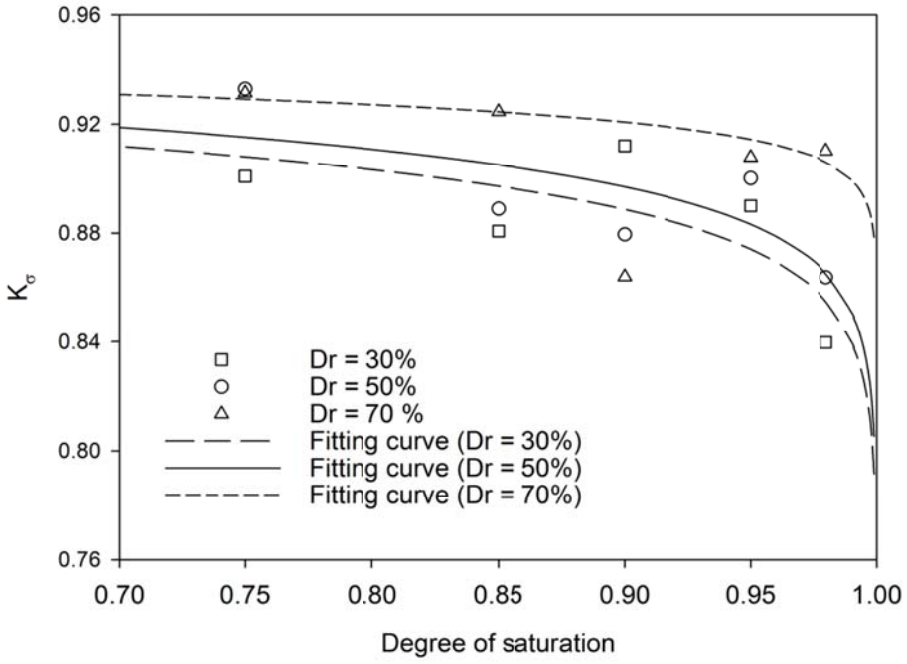

Fig. 3.18 Relationship between degree of saturation and K_σ at ECP = 50 kPa

CHAPTER 4 FINITE ELEMENT MODEL

4.1 Introduction

In order to study the fluid flow and elastoplastic behavior in unsaturated soils subjected to dynamic loading in a boundary value problem, a fully coupled finite element model is needed. The finite element computer code used in this research is U_DYSAC2 (Muraleetharan and Wei 1999b). The fully coupled equations governing the dynamic behavior of unsaturated soils used in U_DYSAC2 are presented here for completeness. The finite element approach utilized by U_DYSAC2 with solid skeleton displacement, pore water pressure, and pore air pressure as primary unknown variables is then detailed. The basic equations include mass balance equations and linear momentum balance equations for the mixture, pore air, and pore water.

4.2 Governing Equations for Unsaturated Soils

4.2.1 Preliminaries

Throughout this section the sign of stresses, strains, and pore pressure follows solid mechanics sign conventions with positive stresses and strains in tension and

negative stresses and strains in compression. Pore water and air pressures are assumed positive in compression. The mathematical description of the behavior of unsaturated soils presented in this research is similar to Lewis and Schrefler (1998), Wei (2001) and Muraleetharan and Wei (1999a) and is derived by extending Biot's formulation. Some details are presented for the completeness. Without loss of generality, the following assumptions are made in this research:

1) all the physical processes are assumed to be under isothermal condition;
2) the solid grains are incompressible;
3) air is considered as a compressible and ideal gas;
4) mass exchange among the solid, water and air phases are neglected;
5) both fluid phases are barotropic, whose densities depend only on upon their pressures;

4.2.2 Basic Definitions

Unsaturated soil is a three-phase porous media consisting of a solid skeleton (s), pore water (w), and pore air (a). The pore space of the solid skeleton is completely filled with the fluid phases β ($\beta = w, a$). Considering a representative elementary volume (REV) in unsaturated soils, each phase has a mass δm_α and a volume δV_α, $\alpha = s, w, a$, the overall volume δV of REV is obtained from the sum of the volumes of α - phase, $\delta V = \sum_\alpha \delta V_\alpha$ and the corresponding mass δm is given by $\delta m = \sum_\alpha \delta m_\alpha$. The volume fraction n^α of α - phase is defined as $n^\alpha = \delta V_\alpha / \delta V$; hence the volume

fractions of the mixture satisfy $n^s + n^w + n^a = 1$ and the degree of saturation $S_{r\beta}$ of fluid phases β is expressed as $S_{r\beta} = n^\beta \Big/ \sum_\beta n^\beta$. The relationships between volume fractions and the parameters typically used in soil mechanics are given by

$$n = n^w + n^a,\ n^s = 1 - n,\ n_w = nS_{rw},\ n^a = n(1 - S_{rw}),\ S_{rw} + S_{ra} = 1 \tag{4.1}$$

where n is porosity of the soil, n_w is the volumetric water content, S_{rw} is degree of water saturation. The intrinsic mass density of α - phase is denoted as $\rho_\alpha = \delta m_\alpha / \delta V_\alpha$, whereas the macroscopic partial density of α - phase is written as $\rho^\alpha = \delta m_\alpha / \delta V$. Thus the macroscopic partial density of α - phase can be expressed by

$$\rho^s = n^s \rho_s = (1 - n)\rho_s \tag{4.2}$$

$$\rho^w = n^w \rho_w = nS_{rw}\rho_w \tag{4.3}$$

$$\rho^a = n^a \rho_a = n(1 - S_{rw})\rho_a \tag{4.4}$$

The overall density ρ of the three-phase mixture is given by

$$\rho = \rho^s + \rho^w + \rho^a = (1 - n)\rho_s + nS_{rw}\rho_w + n(1 - S_{rw})\rho_a \tag{4.5}$$

The velocities for flowing fluid constituents $\beta = w, a$ (water and air) relative to the moving solid $\tilde{\boldsymbol{v}}^{\beta s}$ are defined as

$$\tilde{\mathbf{v}}^{\beta s} = n^{\beta}\left(\mathbf{v}^{\beta} - \mathbf{v}^{s}\right) \tag{4.6}$$

where $\mathbf{v}^{\beta}$ and $\mathbf{v}^{s}$ are the intrinsic or absolute velocities for phase β and the solid skeleton, respectively, which are given by

$$\mathbf{v}^{\beta} = \frac{\partial \mathbf{u}^{\beta}}{\partial t} \text{ and } \mathbf{v}^{s} = \frac{\partial \mathbf{u}}{\partial t} \tag{4.7}$$

where $\mathbf{u}^{\beta}$ and $\mathbf{u}$ are the displacement vectors of phase β and the solid skeleton, respectively. The acceleration of the solid skeleton $\mathbf{a}^{s}$ is defined as $\mathbf{a}^{s} = \partial \mathbf{v}^{s} / \partial t = \ddot{\mathbf{u}}$.

The stress-strain relationship is given in the general incremental form if only small displacements are considered as

$$\dot{\boldsymbol{\sigma}}' = \mathbf{D}\dot{\boldsymbol{\varepsilon}} \tag{4.8}$$

where $\mathbf{D}$ is the tangent stiffness tensor of the soil. The strains of the solid skeleton are related to the skeletal displacements using the classical small strain continuum kinematics as

$$\boldsymbol{\varepsilon} = \frac{1}{2}\left[\nabla \mathbf{u} + \left(\nabla \mathbf{u}\right)^{\mathrm{T}}\right] \tag{4.9}$$

4.2.3 Balance of Mass

The balance of mass for α - phase is written as

$$\frac{D^{\alpha}}{Dt}\left(n^{\alpha}\rho_{\alpha}\right)+n^{\alpha}\rho_{\alpha}\,\mathrm{div}\,\mathbf{v}^{\alpha}=0 \tag{4.10}$$

where $\mathbf{v}^{\alpha}$ is the velocity of α - phase, D^{α}/Dt denotes the material time derivative with respect to the motion of α - phase. For the fluids, $D^{\beta}(\square)/Dt$ is written as (Coussy 1995)

$$\frac{D^{\beta}(\square)}{Dt}=\frac{D^{s}(\square)}{Dt}+\left(\mathbf{v}^{\beta}-\mathbf{v}^{s}\right)\cdot\nabla(\square) \tag{4.11}$$

In this dissertation, the abbreviation $D^{s}(\square)/Dt=\dot{\square}$ is adopted.

With the assumption that the solid grains are incompressible, the material time derivative of solid is

$$\frac{\dot{\rho}_{s}}{\rho_{s}}=0 \tag{4.12}$$

Introducing Eqs. (4.2) and (4.12) into the balance of mass for the solid skeleton (4.10) yields

$$-\dot{n}+(1-n)\,\mathrm{div}\,\mathbf{v}^{s}=0 \tag{4.13}$$

Considering the assumption that all the physical processes are assumed to be under isothermal condition and that the water is barotropic, the material time derivative of pore water phase with respect to the solid skeleton can be obtained as

$$\frac{\dot{\rho}_w}{\rho_w} = \frac{1}{K_w}\dot{p}_w \tag{4.14}$$

where K_w is the bulk modulus of pore water and p_w is the pore water pressure. Similarly, the material time derivative of pore air phase with respect to the solid skeleton can be expressed as

$$\frac{\dot{\rho}_a}{\rho_a} = \frac{1}{K_a}\dot{p}_a \tag{4.15}$$

where K_a is the bulk modulus of pore air and p_a is the pore air pressure. With the assumption of isothermal condition, using Boyle's law ($p_a V_a = const.$), the bulk modulus of pore air is equal to the magnitude of the pore air pressure p_a, i.e., $K_a = p_a$.

Substituting Eqs. (4.3) , (4.11) and (4.14) into the balance of mass for the pore water (4.10) gives

$$\rho_w \dot{n}^w + \frac{nS_{rw}}{K_w}\rho_w \dot{p}_w + nS_{rw}\rho_w \mathrm{div}\,\mathbf{v}^s + \mathrm{div}\,(\rho_w \tilde{\mathbf{v}}^{ws}) = 0 \tag{4.16}$$

Following Wei and Muraleetharan (2002a, 2002b), the volume fraction of the water is assumed to be a function of matric suction and volumetric strain of the solid skeleton, which is given as

$$n^w = f\left(\varepsilon_v, s_c\right) \tag{4.17}$$

Applying the chain rule, the material time derivative of volume fraction of pore water $\dot{n}^w$ can be given in terms of matric suction s_c and volumetric strain of the solid skeleton ε_v

$$\dot{n}^w = \frac{\partial n^w}{\partial \varepsilon_v}\dot{\varepsilon}_v + \frac{\partial n^w}{\partial s_c}\dot{s}_c = \left(1-n\right) S_{rw} \operatorname{div} \mathbf{v}^s + \frac{1}{\Gamma}\left(\dot{p}_a - \dot{p}_w\right) \tag{4.18}$$

With Eqs. (4.13) and (4.18), the balance of mass for the pore water with respect to solid skeleton can be expressed as

$$S_{rw} \operatorname{div} \mathbf{v}^s + \left(\frac{nS_{rw}}{K_w} - \frac{1}{\Gamma}\right)\dot{p}_w + \frac{1}{\Gamma}\dot{p}_a + \operatorname{div}\left(\tilde{\mathbf{v}}^{ws}\right) + \frac{\operatorname{grad}\rho_w}{\rho_w}\tilde{\mathbf{v}}^{ws} = 0 \tag{4.19}$$

Similarly, with the Eqs. (4.6), (4.11), (4.13) , (4.15) and (4.18), the balance of mass for the pore air (4.10) can be rearranged to

$$\left(1-S_{rw}\right)\operatorname{div}\mathbf{v}^{s}+\frac{1}{\Gamma}\dot{p}_{w}+\left[\frac{n\left(1-S_{rw}\right)}{p_{a}}-\frac{1}{\Gamma}\right]\dot{p}_{a}+\operatorname{div}\left(\tilde{\mathbf{v}}^{as}\right)+\frac{\operatorname{grad}\rho_{a}}{\rho_{a}}\tilde{\mathbf{v}}^{as}=0 \tag{4.20}$$

4.2.4 Balance of Linear Momentum

The linear momentum balance equation for the mixture is obtained by adding the balance equations of linear momentum for three phases and disregarding the viscous forces and convective terms

$$\rho\ddot{\mathbf{u}}-\operatorname{div}\boldsymbol{\sigma}-\rho\mathbf{b}=0 \tag{4.21}$$

where $\boldsymbol{\sigma}$ is the total Cauchy stress tensor, $\mathbf{b}$ is the body force tensor.

The linear momentum balance equations for pore water and pore air phase results in the generalized Darcy's law

$$\tilde{\mathbf{v}}^{\beta s}=-\mathbf{k}_{\beta}\left(\nabla p_{\beta}-\rho_{\beta}\mathbf{b}+\rho_{\beta}\ddot{\mathbf{u}}\right) \tag{4.22}$$

where $\mathbf{k}_{\beta}$ is the permeability of phase β which is given as

$$\mathbf{k}_{\beta}=\frac{\mathbf{k}k_{r\beta}}{\mu_{\beta}} \tag{4.23}$$

where **k** is the intrinsic permeability tensor, $k_{r\beta}$ is the relative permeability of phase β , which is dependent on the degree of relative saturation ($0 \le k_{r\beta} \le 1$), μ_β is the dynamic viscosity. Empirical relations for $k_{r\beta}$ can be found in the literature (Brooks and Corey 1964, Mualem 1976, van Genuchten 1980). In this dissertation, the following equations based on the van Genuchten-Mualem (VGM) model (van Genuchten 1980) are accepted

$$k_{rw} = S_e^{0.5}\left[1-\left(1-S_e^{1/m}\right)^m\right]^2 \tag{4.24}$$

$$k_{ra} = \left(1-S_e\right)^{0.5}\left(1-S_e^{1/m}\right)^{2m} \tag{4.25}$$

where m is the material parameter, S_e is the effective degree of water saturation which is given by

$$S_e = \frac{S_{rw}-S_{rw}^r}{S_{rw}^s-S_{rw}^r} \tag{4.26}$$

where S_{rw}^r and S_{rw}^s are the residual (minimum) and saturated (maximum) degrees of water saturation.

Neglecting the spatial gradient of the water density according to Lewis and Schrefler (1998) and eliminating $\tilde{\mathbf{v}}^{\beta s}$ from Eqs. (4.19) and (4.20) by means of (4.22), the fully coupled governing equations for unsaturated porous media with solid skeleton

displacement $\mathbf{u}$, pore water pressure p_w, and pore water pressure p_a as the primary unknown variables are arrived

$$\rho\ddot{\mathbf{u}} = \operatorname{div}\boldsymbol{\sigma} + \rho\mathbf{b} \tag{4.27}$$

$$S_{rw}\operatorname{div}\dot{\mathbf{u}} + \left(\frac{nS_{rw}}{K_w} - \frac{1}{\Gamma}\right)\dot{p}_w + \frac{1}{\Gamma}\dot{p}_a + \operatorname{div}\left[-\frac{\mathbf{k}k_{rw}}{\mu_w}\left(\nabla p_w - \rho_w\mathbf{b} + \rho_w\ddot{\mathbf{u}}\right)\right] = 0 \tag{4.28}$$

$$\left(1 - S_{rw}\right)\operatorname{div}\dot{\mathbf{u}} + \frac{1}{\Gamma}\dot{p}_w + \left[\frac{n\left(1 - S_{rw}\right)}{p_a} - \frac{1}{\Gamma}\right]\dot{p}_a + \operatorname{div}\left(-\frac{\mathbf{k}k_{ra}}{\mu_a}\left(\nabla p_a - \rho_a\mathbf{b} + \rho_a\ddot{\mathbf{u}}\right)\right) = 0 \tag{4.29}$$

4.3 Boundary and Initial Conditions

In order to obtain the numerical solution for the governing equations of the initial and boundary value problems (IBVP) in a domain Ω with boundary $\Gamma = \partial\Omega$ and in a time period $[0, t]$, the initial and boundary conditions are needed. The boundary is composed of DIRICHLET or forced boundary (Γ_D) and NEUMANN or natural boundary (Γ_N)

DIRICHLET boundary (Γ_D)	NEUMANN boundary (Γ_N)
displacement specified: $\mathbf{u} = \bar{\mathbf{u}}$ on Γ_u	traction specified: $\boldsymbol{\sigma}\cdot\mathbf{n} = \bar{\mathbf{t}}$ on Γ_t
water pressure specified: $p_w = \bar{p}_w$ on Γ_{p_w}	water flux specified: $\tilde{\mathbf{v}}^{ws}\cdot\mathbf{n} = \bar{q}_w$ on Γ_{q_w}
air pressure specified: $p_a = \bar{p}_a$ on Γ_{p_a}	air flux specified: $\tilde{\mathbf{v}}^{as}\cdot\mathbf{n} = \bar{q}_a$ on Γ_{q_a}

where $\bar{\boldsymbol{u}}$ is the prescribed displacement vector for the solid skeleton, $\bar{p}_w$ and $\bar{p}_a$ are the prescribed pore water and air pressure, $\bar{\mathbf{t}}$ is the prescribed traction vector, $\bar{q}_w$ and $\bar{q}_a$ are the prescribed values of the flux on a unit area with unit normal vector $\mathbf{n}$ on the permeable boundaries Γ_{q_w} and Γ_{q_a}. The boundaries hold

$$\begin{aligned} \Gamma_u \cup \Gamma_t &= \Gamma_{p_w} \cup \Gamma_{q_w} = \Gamma_{p_a} \cup \Gamma_{q_a} = \Gamma \\ \Gamma_u \cap \Gamma_t &= \Gamma_{p_w} \cap \Gamma_{q_w} = \Gamma_{p_a} \cap \Gamma_{q_a} = \varnothing \end{aligned} \tag{4.30}$$

The initial conditions are stated by

$$\mathbf{u} = \mathbf{u}_0,\ p_w = p_{w0},\ p_a = p_{a0}\ (\text{in } \Omega \text{ at } t = 0) \tag{4.31}$$

4.4 Weak Form and Spatial Discretization of Governing Equations

Taking into account the arbitrary test function $\delta\mathbf{u}$ and the traction specified boundary condition over the domain Ω, the weak form of the momentum balance equation can be obtained as

$$\int_\Omega \mathrm{div}\boldsymbol{\sigma} \cdot \delta\mathbf{u}\,\mathrm{d}\Omega + \int_\Omega \rho\mathbf{b} \cdot \delta\mathbf{u}\,\mathrm{d}\Omega - \int_\Omega \rho\ddot{\mathbf{u}} \cdot \delta\mathbf{u}\,\mathrm{d}\Omega + \int_{\Gamma_t} \left(\bar{\mathbf{t}} - \boldsymbol{\sigma} \cdot \mathbf{n}\right) \cdot \delta\mathbf{u}\,\mathrm{d}\Gamma = 0 \tag{4.32}$$

Applying the Gauss Divergence Theorem,

$$\int_\Omega \mathrm{div}\boldsymbol{\sigma}\cdot\delta\mathbf{u}\,\mathrm{d}\Omega = \int_{\Gamma_t}\boldsymbol{\sigma}\cdot\mathbf{n}\cdot\delta\mathbf{u}\,\mathrm{d}\Gamma - \int_\Omega \boldsymbol{\sigma}\cdot\nabla\left(\delta\mathbf{u}\right)\mathrm{d}\Omega \tag{4.33}$$

Substituting Eqs. (3.1), (3.2) and (4.33), the weak form of the momentum balance equation can be obtained as

$$\begin{aligned}&\int_\Omega \rho\ddot{\mathbf{u}}\cdot\delta\mathbf{u}\mathrm{d}\Omega + \int_\Omega \boldsymbol{\sigma}'\cdot\nabla\left(\delta\mathbf{u}\right)\mathrm{d}\Omega - \int_\Omega\left(1-nS_{rw}\right)p_a\mathbf{I}\cdot\nabla\left(\delta\mathbf{u}\right)\mathrm{d}\Omega \\ &\quad - \int_\Omega nS_{rw}p_w\mathbf{I}\cdot\nabla\left(\delta\mathbf{u}\right)\mathrm{d}\Omega - \int_{\Gamma_t}\bar{\mathbf{t}}\cdot\delta\mathbf{u}\,\mathrm{d}\Gamma - \int_\Omega\rho\mathbf{b}\cdot\delta\mathbf{u}\,\mathrm{d}\Omega = 0\end{aligned} \tag{4.34}$$

where $\delta\mathbf{u}$ denotes the virtual displacement of the solid skeleton.

Similarly, considering the arbitrary test function δp_w and the water flux specified boundary condition, the weak form of mass balance equations for the pore water can be obtained as

$$\begin{aligned}&\int_\Omega \delta p_w S_{rw}\,\mathrm{div}\,\dot{\mathbf{u}}\,\mathrm{d}\Omega + \int_\Omega \delta p_w\left(\frac{nS_{rw}}{K_w}-\frac{1}{\Gamma}\right)\dot{p}_w\mathrm{d}\Omega + \int_\Omega \delta p_w\frac{1}{\Gamma}\dot{p}_a\mathrm{d}\Omega + \\ &\int_{\Gamma_{q_w}}\delta p_w\bar{q}_w\mathrm{d}\Gamma - \int_\Omega \mathrm{grad}\delta p_w\cdot\tilde{\mathbf{v}}^{ws}\mathrm{d}\Omega = 0\end{aligned} \tag{4.35}$$

and considering the arbitrary test function δp_a and the air flux specified boundary condition, neglecting the spatial gradient of the air density, the weak form of mass balance equations for the pore air can be obtained as

$$\int_\Omega \delta p_a \left(1-S_{rw}\right) \operatorname{div} \dot{\mathbf{u}}\, \mathrm{d}\Omega + \int_\Omega \delta p_a \frac{1}{\Gamma} \dot{p}_w \mathrm{d}\Omega + \int_\Omega \delta p_a \left[\frac{n\left(1-S_{rw}\right)}{p_a} - \frac{1}{\Gamma}\right] \dot{p}_a \mathrm{d}\Omega +$$

$$\int_{\Gamma_{q_a}} \delta p_a \bar{q}_a \mathrm{d}\Gamma - \int_\Omega \operatorname{grad} \delta p_a \cdot \tilde{\mathbf{v}}^{as} \mathrm{d}\Omega = 0 \tag{4.36}$$

For the finite element discretization of Equations (4.34)–(4.36), the global shape function $\mathbf{N_u}$, $\mathbf{N_{p_w}}$ and $\mathbf{N_{p_a}}$ are used for the approximation of the displacement field, pore water pressure, and pore air pressure fields in the whole domain, respectively

$$\mathbf{u} = \mathbf{N_u U},\ p_w = \mathbf{N_{p_w} P_w},\ p_a = \mathbf{N_{p_a} P_a} \tag{4.37}$$

where $\mathbf{U}$, $\mathbf{P_w}$ and $\mathbf{P_a}$ are the global vectors of the nodal values for the displacement of the solid skeleton, pore water pressure, and pore air pressure. After discretizing the weak form of the non-linear partial differential equations (4.34)–(4.36) using a standard finite element procedure, the following fully coupled algebraic equations can be derived

$$\mathbf{M_s}\ddot{\mathbf{U}} + \int_\Omega \mathbf{B}^{\mathrm{T}} \boldsymbol{\sigma}' d\Omega - \mathbf{H_{sw}} \mathbf{P_w} - \mathbf{H_{sa}} \mathbf{P_a} = \mathbf{F_s} \tag{4.38}$$

$$\mathbf{M_w}\ddot{\mathbf{U}} + \mathbf{C_{ws}}\dot{\mathbf{U}} + \mathbf{C_{ww}}\dot{\mathbf{P}}_\mathbf{w} + \mathbf{C_{wa}}\dot{\mathbf{P}}_\mathbf{a} + \mathbf{H_{ww}}\mathbf{P_w} = \mathbf{F_w} \tag{4.39}$$

$$\mathbf{M_a}\ddot{\mathbf{U}} + \mathbf{C_{as}}\dot{\mathbf{U}} + \mathbf{C_{aw}}\dot{\mathbf{P}}_\mathbf{w} + \mathbf{C_{aa}}\dot{\mathbf{P}}_\mathbf{a} + \mathbf{H_{aa}}\mathbf{P_a} = \mathbf{F_a} \tag{4.40}$$

where the coefficient matrices are

Mass matrix $\qquad \mathbf{M_s} = \int_\Omega \mathbf{N_u}^{\mathrm{T}} \rho \mathbf{N_u} \mathrm{d}\Omega$

Solid-water coupling matrix $\mathbf{H}_{\mathbf{sw}} = \int_{\Omega} \mathbf{B}^{\mathrm{T}} n S_{rw} \mathbf{m} \mathbf{N}_{\mathbf{p_w}} \mathrm{d}\Omega$

Solid-air coupling matrix $\mathbf{H}_{\mathbf{sa}} = \int_{\Omega} \mathbf{B}^{\mathrm{T}} \left(1 - n S_{rw}\right) \mathbf{m} \mathbf{N}_{\mathbf{p_a}} \mathrm{d}\Omega$

Load vector $\mathbf{F}_{\mathbf{s}} = \int_{\Gamma_t} \mathbf{N}_{\mathbf{u}}^{\mathbf{T}} \overline{\mathbf{t}} \, \mathrm{d}\Gamma + \int_{\Omega} \mathbf{N}_{\mathbf{u}}^{\mathbf{T}} \rho \mathbf{b} \mathrm{d}\Omega$

Water seepage matrix $\mathbf{M}_{\mathbf{w}} = \int_{\Omega} \left(\nabla \mathbf{N}_{\mathbf{p_w}}\right)^{\mathbf{T}} \rho_w \frac{\mathbf{k} k_{rw}}{\boldsymbol{\mu}_{\mathbf{w}}} \mathbf{N}_{\mathbf{u}} \mathrm{d}\Omega$

Water-solid coupling matrix $\mathbf{C}_{\mathbf{ws}} = \int_{\Omega} \mathbf{N}_{\mathbf{p_w}}^{\mathbf{T}} S_{rw} \mathbf{m}^{\mathbf{T}} \mathbf{B} \mathrm{d}\Omega$

Water compressibility matrix $\mathbf{C}_{\mathbf{ww}} = \int_{\Omega} \mathbf{N}_{\mathbf{p_w}}^{\mathbf{T}} \left(\frac{n S_{rw}}{K_w} - \frac{1}{\Gamma} \right) \mathbf{N}_{\mathbf{p_w}} \mathrm{d}\Omega$

Water-air coupling matrix $\mathbf{C}_{\mathbf{wa}} = \int_{\Omega} \mathbf{N}_{\mathbf{p_w}}^{\mathbf{T}} \frac{1}{\Gamma} \mathbf{N}_{\mathbf{p_w}} \mathrm{d}\Omega$

Water permeability matrix $\mathbf{H}_{\mathbf{ww}} = \int_{\Omega} \left(\nabla \mathbf{N}_{\mathbf{p_w}}\right)^{\mathbf{T}} \frac{\mathbf{k} k_{rw}}{\boldsymbol{\mu}_{\mathbf{w}}} \nabla \mathbf{N}_{\mathbf{p_w}} \, \mathrm{d}\Omega$

Load vector for water phase $\mathbf{F}_{\mathbf{w}} = \int_{\Omega} \left(\nabla \mathbf{N}_{\mathbf{p_w}}\right)^{\mathbf{T}} \rho_w \frac{\mathbf{k} k_{rw}}{\boldsymbol{\mu}_{\mathbf{w}}} \mathbf{b} \mathrm{d}\Omega - \int_{\Gamma_{q_w}} \mathbf{N}_{\mathbf{p_w}}^{\mathbf{T}} \overline{q}_w \mathrm{d}\Gamma$

Air seepage matrix $\mathbf{M}_{\mathbf{a}} = \int_{\Omega} \left(\nabla \mathbf{N}_{\mathbf{p_a}}\right)^{\mathbf{T}} \rho_a \frac{\mathbf{k} k_{ra}}{\boldsymbol{\mu}_{\mathbf{a}}} \mathbf{N}_{\mathbf{u}} \, \mathrm{d}\Omega$

Air-solid coupling matrix $\mathbf{C}_{\mathbf{as}} = \int_{\Omega} \mathbf{N}_{\mathbf{p_a}}^{\mathbf{T}} \left(1 - S_{rw}\right) \mathbf{m}^{\mathbf{T}} \mathbf{B} \mathrm{d}\Omega$

Air compressibility matrix $\mathbf{C}_{\mathbf{aa}} = \int_{\Omega} \mathbf{N}_{\mathbf{p_a}}^{\mathbf{T}} \left[\frac{n\left(1 - S_{rw}\right)}{p_a} - \frac{1}{\Gamma} \right] \mathbf{N}_{\mathbf{p_a}} \mathrm{d}\Omega$

Air-water coupling matrix $\mathbf{C}_{\mathbf{aw}} = \int_{\Omega} \mathbf{N}_{\mathbf{p_a}}^{\mathbf{T}} \frac{1}{\Gamma} \mathbf{N}_{\mathbf{p_w}} \mathrm{d}\Omega$

Air permeability matrix $\mathbf{H}_{\mathbf{aa}} = \int_{\Omega} \left(\nabla \mathbf{N}_{\mathbf{p_a}}\right)^{\mathbf{T}} \frac{\mathbf{k} k_{ra}}{\boldsymbol{\mu}_{\mathbf{a}}} \nabla \mathbf{N}_{\mathbf{p_a}} \, \mathrm{d}\Omega$

Load vector for air phase $\mathbf{F_a} = \int_\Omega \left(\nabla \mathbf{N_{p_a}}\right)^{\mathrm{T}} \rho_a \frac{\mathbf{k}k_{ra}}{\boldsymbol{\mu}_\mathbf{a}} \mathbf{b} \mathrm{d}\Omega - \int_{\Gamma_{q_a}} \mathbf{N}_{\mathbf{p_a}}^{\mathrm{T}} \bar{q}_a \mathrm{d}\Gamma$

$\boldsymbol{B}$ is strain operator relating strain vector to total nodal displacements

$\mathbf{m} = \begin{bmatrix} 1 & 1 & 1 & 0 & 0 & 0 \end{bmatrix}^T$

4.5 Time Integration

In order to integrate the spatially discretized finite element equations in the time domain, Equation (4.38)-(4.40) can be written in residual matrix form as

$$\mathbf{M}\ddot{\mathbf{x}} + \mathbf{C}\dot{\mathbf{x}} + \mathbf{H}\mathbf{x} + \mathbf{P} = \mathbf{F} \tag{4.41}$$

where $\mathbf{x} = \begin{Bmatrix} \mathbf{U} & p_w & p_a \end{Bmatrix}^T$ denotes the basic unknown variable vector, $\mathbf{M}$ is the mass matrix, $\mathbf{C}$ is the damping matrix, $\mathbf{H}$ is the pore fluid stiffness, $\mathbf{P} = \left\{ \int_\Omega \mathbf{B}^{\mathrm{T}} \boldsymbol{\sigma}' \mathrm{d}\Omega \quad 0 \quad 0 \right\}^T$ respents the internal force vector for the solid skeleton, $\mathbf{F}$ is the external force vector. The residual dynamic equations is solved using implicit Hilber-Hughes-Taylor α - method (Hilber et al. 1977) which is an implicit continuation of the Newmark β method. The method is unconditionally stable and second-order accurate (Hughes 1987) with the time-integration parameters $-\frac{1}{3} \le \alpha \le 0$, $\gamma = \frac{1}{2}(1-2\alpha)$, $\beta = \frac{1}{4}(1-\alpha)^2$. This method has been utilized to study the dynamics of saturated soils and unsaturated soils by many researchers (Muraleetharan et al. 1994, Muraleetharan et al. 2004,

Ravichandran and Muraleetharan 2009, Ravichandran et al. 2015). So Equation (4.41) can be written as

$$\mathbf{f}_{eff} = \mathbf{M}\ddot{\mathbf{x}}_{n+1} + (1+\alpha)\mathbf{C}\dot{\mathbf{x}}_{n+1} - \alpha\mathbf{C}\dot{\mathbf{x}}_{n} + (1+\alpha)\mathbf{H}\mathbf{x}_{n+1} - \alpha\mathbf{H}\mathbf{x}_{n} + (1+\alpha)\mathbf{P}_{n+1} - \alpha\mathbf{P}_{n} - (1+\alpha)\mathbf{F}_{n+1} + \alpha\mathbf{F}_{n} \tag{4.42}$$

where

$$\dot{\mathbf{x}}_{n+1} = \dot{\mathbf{x}}_{n} + \Delta t\left[(1-\gamma)\ddot{\mathbf{x}}_{n} + \gamma\ddot{\mathbf{x}}_{n+1}\right]$$

$$\mathbf{x}_{n+1} = \mathbf{x}_{n} + \Delta t\dot{\mathbf{x}}_{n} + \Delta t^{2}\left[(0.5-\beta)\ddot{\mathbf{x}}_{n} + \beta\ddot{\mathbf{x}}_{n+1}\right]$$

where n is the nth discrete time t_n, $\Delta t = t_{n+1} - t_n$ is time step.

Nonlinear Equation (4.42) is solved using Newton-Raphson method. The resulting equation can be written as

$$\mathbf{M}^{i}_{eff}\Delta\ddot{\mathbf{x}}^{i+1} + \mathbf{f}^{i}_{eff} = 0 \tag{4.43}$$

where $\mathbf{M}_{eff}$ is the effective stiffness which is given by:

$$\mathbf{M}^{i}_{eff} = \left[\mathbf{M} + (1+\alpha)\gamma\Delta t\mathbf{C} + (1+\alpha)\beta\Delta t^{2}\mathbf{H} + (1+\alpha)\beta\Delta t^{2}\mathbf{K}_{T}\right]^{i} \tag{4.44}$$

where $\mathbf{K}_T$ is the global tangent stiffness matrix, which is given as

$$\mathbf{K}_T = \frac{d\left(\int_\Omega \mathbf{B}^T \boldsymbol{\sigma}' \mathrm{d}\Omega\right)}{d\mathbf{x}} = \int_\Omega \mathbf{B}^T \mathbf{D}\mathbf{B}\mathrm{d}\Omega \tag{4.45}$$

These equations are implemented into a two dimensional FORTRAN finite element computer code, U_DYSAC2 (Muraleetharan and Wei 1999b) with solid displacements, pore water pressure and pore air pressure as nodal variables. The solution procedure used is given in Table 4.1.

Table 4.1 Solution procedure for dynamic analysis

Data: $\boldsymbol{u}_0$, p_{w0}, p_{a0}

Loop over time steps: $n \in [0, NT]$, $n\Delta t \in [0, T]$

Given time step size $\Delta t = t_{n+1} - t_n$ and solution at t_n, find solution at t_{n+1}

Loop over iteration steps: i

$i = 0$

Predictor phase

Calculate: $\ddot{\mathbf{x}}_{n+1} = 0$

$$\dot{\mathbf{x}}_{n+1} = \dot{\mathbf{x}}_n + (1-\gamma)\Delta t \ddot{\mathbf{x}}_n$$

$$\mathbf{x}_{n+1} = \mathbf{x}_n + \Delta t \dot{\mathbf{x}}_n + (0.5-\beta)\Delta t^2 \ddot{\mathbf{x}}_n$$

For *every element*

For *every quadrature points*

Calculate $\Delta\boldsymbol{\varepsilon}_{n+1}$, Δp_w, Δp_a, Δs_c

Call constitutive model to calculate $\boldsymbol{\sigma}'$ and $\boldsymbol{D}_T$

Calculate $\mathbf{K}_T$, ρ, n, S_{rw}, $k_{r\beta}$, $n_{w,n+1}$

$$\mathbf{M},\ \mathbf{C},\ \mathbf{H},\ \int_\Omega \mathbf{B}^T \boldsymbol{\sigma}' \mathrm{d}\Omega,\ \mathbf{F}$$

Calculate $\mathbf{M}_{eff}^i$ and $\mathbf{f}_{eff}^i$, solve $\Delta\ddot{\mathbf{x}}^{i+1} = -\left(\mathbf{M}_{eff}^i\right)^{-1} \mathbf{f}_{eff}^i$

Corrector phase

Calculate: $\ddot{\mathbf{x}}_{n+1}^{i+1} = \ddot{\mathbf{x}}_{n+1}^i + \Delta\ddot{\mathbf{x}}^{i+1}$

$$\dot{\mathbf{x}}_{n+1}^{i+1} = \dot{\mathbf{x}}_{n+1}^i + \Delta t \gamma \Delta\ddot{\mathbf{x}}^{i+1}$$

$$\mathbf{x}_{n+1}^{i+1} = \mathbf{x}_{n+1}^i + \Delta t^2 \gamma \Delta\ddot{\mathbf{x}}^{i+1}$$

Repeat For *every element*

For *every quadrature points*

Calculate $\mathbf{f}_{eff}^i$

Check convergence: $\dfrac{\left\| \boldsymbol{f}_{eff}^{i+1} \right\|}{\left\| \boldsymbol{f}_{eff}^{0} \right\|} \le \varepsilon_1$ and $\dfrac{\left\| \Delta\ddot{\mathbf{x}}^{i+1} \right\|}{\left\| \Delta\ddot{\mathbf{x}}^{1} \right\|} \le \varepsilon_2$

$i \leftarrow i+1$

$n \leftarrow n+1$

End

CHAPTER 5 INCORPORATING HYDRAULIC HYSTERESIS IN DYNAMIC ANALYSIS

5.1 Introduction

One common assumption made in the numerical analysis of dynamic behavior of unsaturated soils presented in the literature review in Chapter 2 is the use of a single function to describe the relationship between degree of saturation and the matric suction, i.e., SWCC. SWCC plays an important role in describing the behavior of unsaturated soils. Experimental investigations have shown that the SWCC is not a single curve, but a series of curves exhibiting hysteresis as the soil undergoes wetting and drying. Although some progress has been made to account for the hydraulic hysteresis of SWCCs in the numerical analysis of dynamic behavior of unsaturated soils, it is apparent that more research is needed.

This chapter is intended to study the effect of the hydraulic hysteresis on the dynamic behavior of unsaturated soils. This is accomplished by utilizing the numerical model developed in Chapter 4 to simulate the dynamic behavior, including the hydraulic hysteresis in SWCCs. A recently developed model based on the bounding surface plasticity theory (Liu and Muraleetharan 2006, 2012a) to describe the SWCCs was implemented into U_DYSAC2. Instead of using the coupled hydro-mechanical

constitutive model CM4USS, as a first step, a simplified bounding surface elastoplastic model (Muraleetharan and Nedunuri 1998) is utilized to describe the stress-strain behavior of unsaturated soils in this chapter.

In order to demonstrate the performance of the modified U_DYSAC2, comparisons between the numerical results and the experimental results of drying-wetting of a Dune sand column are provided. U_DYSAC2 with the hydraulic hysteresis and a single SWCC (drying bound) are then used to analyze the problem of an unsaturated embankment subjected to base shaking. The effect of the hydraulic hysteresis on the dynamic behavior of unsaturated soils is highlighted by comparing the predicted horizontal and vertical displacements, pore water pressure, pore air pressure, and suction at various locations of the embankment from the analyses with and without hydraulic hysteresis.

Portions of this chapter have been published in Zhang and Muraleetharan (2017).

5.2 Numerical Model

5.2.1 Finite Element Formulation

The governing equations are given in Chapter 4. A number of comprehensive elastoplastic constitutive models, which employ the mean net stress ($\boldsymbol{\sigma}^N = \boldsymbol{\sigma} - p_a \mathbf{I}$) and matric suction ($s_c = p_a - p_w$) as stress variables, have been developed to deal with the stress-strain behavior of unsaturated soils (Alonso et al. 1990, Vaunat et al. 2000,

Wheeler et al. 2003, Sheng et al. 2004, Sheng et al. 2008a), with $\mathbf{I}$ being the second-order unit tensor. In this chapter, a generalized elastoplastic constitutive model (Muraleetharan and Nedunuri 1998) which uses net stress and suction is used to define the stress strain behavior of unsaturated soils. The model is developed within the framework of critical state soil mechanics principles and bounding surface concepts. The suction effect was incorporated based on the concepts for unsaturated soils proposed by Alonso et al. (1990), Wheeler and Sivakumar (1995), and Wheeler (1996). The model has been employed to represent the elastoplastic behavior of unsaturated soils (Ravichandran 2009, Ravichandran and Muraleetharan 2009). The stress variable in this chapter is defined as follows:

$$\boldsymbol{\sigma}^{N} = \boldsymbol{\sigma} - p_a \mathbf{I} \tag{5.1}$$

where $\boldsymbol{\sigma}$ is the total stress tensor, $\boldsymbol{\sigma}^{N}$ is the net stress sensor. The fully coupled algebraic equation (4.38) should be modified as:

$$\mathbf{M_s}\ddot{\mathbf{U}} + \int_{\Omega} \mathbf{B}^{\mathbf{T}} \boldsymbol{\sigma}^{\mathbf{N}} d\Omega - \mathbf{H_{sa}} \mathbf{P_a} = \mathbf{F_s} \tag{5.2}$$

where $\mathbf{H_{sa}} = \int_{\Omega} \mathbf{B}^{\mathrm{T}} \mathbf{m} \mathbf{N_{p_a}} d\Omega$ which is different from the definition in Eq. (4.38).

5.2.2 Implementation of Hysteretic Soil Water Characteristic Curves

The hysteretic model for SWCCs based on the bounding surface plasticity theory (Liu and Muraleetharan 2006, 2012a) is adopted to describe the hydraulic behavior. The review of this model is given in Chapter 3. Because Γ is highly nonlinear, the Newton-Raphson method is employed to update the volume fraction of water for given incremental suction Δs_c in the implementation of the hysteretic SWCCs in the code U_DYSAC2. The details of the algorithm are shown in Table 5.1. The derivation of $\partial\Gamma/\partial n_w$ is given in Appendix A. The drying or wetting path should be determined according to incremental suction Δs_c before updating $\partial\Gamma/\partial n_w$. A tolerance value of $TOL = 10^{-9}$ is used in this research.

5.3 Validation

To evaluate the performance of the modified U_DYSAC2 for simulating hysteretic flow in unsaturated soils, an experiment with slow drainage-rewetting reported by Gillham et al. (1979) was simulated. The experiment involved a 60 cm high, initially saturated, Dune sand column. It was allowed to drain and then rewetted by regulating the water pressure at the bottom of the sand column as shown in Fig. 5.1. The initial condition for the sand column was a linear water pressure variation from 0 kPa at the top to 5.886 kPa at the bottom. The top and lateral boundaries were impermeable to water flow. All the boundaries were prescribed with zero pore air pressure. The water content distribution along the column was measured at different times. More details about the experiment can be found in Gillham et al. (1979).

The saturated hydraulic conductivity of water employed in the simulation is 6.5×10^{-5} m/s. The material properties of the Dune sand are given in Table 5.2. The solid skeleton stress-strain behavior was simulated using an elastic model. The parameters for SWCCs model were calibrated from the test results as shown in Fig. 5.2 with $n_{ws} = 0.301$, $n_{wr} = 0.094$, $b_3 = 34.0$, $d_3 = 7.9$, $b_2 = 20.4$, $d_2 = 4.1$, $\Gamma^e = -1700$ kPa, and $H = 5.0$. The simulations run with hysteretic SWCCs, non-hysteretic SWCC corresponding to the drying boundary, and non-hysteretic SWCC corresponding to the wetting boundary, which are referred to as H, NHD, and NHW simulations, respectively, are summarized and compared. The predicted water pressure head and water content are compared with the measured data at elevation 21 cm, 33 cm and 49 cm in Fig. 5.3 and Fig. 5.4. Results show that the H simulations in general agree with the experimental results. Comparison of the pressure head and water content at different elevations for H and NHD simulations exhibits essentially the same results during the drying phase but shows a substantial deviation during the wetting phase. Marked differences between the H and NHW simulations are observed, especially during the drying phase. The predicted water contents profile is plotted in Fig. 5.5 for comparison with the experimental results. The predicted water content profile with hysteresis lies between the profiles for the NHD and NHW simulations and generally agrees well with the measured results at all the measured time instances. At the time of $t = 68$ min, the top half of the column is continuing to drain and the hydraulic path is moving along the drying boundary, resulting in essentially identical predicted volumetric water contents for the H and NHD simulations and smaller volumetric water content for the NHW simulation. The lower 30 cm of the column is in the wetting phase and the

hydraulic path is moving along the wetting scanning curve, therefore the predicted water content for the H simulation agrees well with experimental results. At $t = 125$ min, comparison of the H and NHD simulations indicate fairly close correspondence at the upper 2 cm and lower 32 cm of the column, but shows a greater discrepancy at other parts. The upper 2 cm is still in the drying phase and the predicted water contents for the H and NHD simulations are the same. The lower parts are in the saturated state while other parts of the column are in the wetting phase. So the NHD simulation indicates a gross overestimation of the water content. The predicted hydraulic paths at different elevations are shown in Fig. 5.6 and the above described differences can be observed in these curves.

5.4 Dynamic Analysis of an Unsaturated Soil Embankment

5.4.1 Finite Element Model

A compacted unsaturated soil embankment made of Minco Silt subjected to base shaking was considered to highlight the differences between the analyses using hysteretic and a non-hysteretic SWCCs. The drying boundary curve was employed in the non-hysteretic analysis because it is typically used in unsaturated soil analyses. Minco silt is an Oklahoma silt and the engineering properties of Minco silt have been experimentally investigated at the University of Oklahoma (Ananthanathan 2002, Vinayagam 2004, Tan 2005). According to the USCS classification, Minco silt belongs to CL. It is composed of 27% of sand and 73% of fines with a specific gravity

$G_s = 2.69$, Liquid Limit = 30%, and Plastic Limit = 22%. The maximum dry unit weight is about 17.7 kN/m^3, and its optimum moisture content is about 14.6%. The material properties of Minco Silt are shown in Table 5.3. The stress-strain behavior of unsaturated Minco Silt is modeled using a bounding surface elastoplastic model (Muraleetharan and Nedunuri 1998). The model parameters were obtained from Ravichandran (2009). The SWCCs model parameters can be found in Liu and Muraleetharan (2012b). All the constitutive model parameters are summarized in Table 5.4. The height of the unsaturated embankment is 8.5 m and the width is 17.5 m at the base, which decreases to 2 m at the top. The finite element mesh used for the unsaturated soil embankment is shown in Fig. 5.7, which is discretized into 190 two-dimensional four-node quadrilateral elements with 212 nodes. The initial void ratio and degree of saturation are 0.815 and 65%, respectively. With the assumption that the initial suction is on the drying boundary curve and the initial pore air pressure is 0.0 kPa, the initial pore water pressure is -29.2 kPa. The boundary conditions are as follows: the base of the embankment is impervious to both water and air and is constrained in the vertical and horizontal directions to the base. On all other sides of the embankment zero traction is specified and water and air are allowed to drain freely (i.e., the pore water and pore air pressure are kept constant at the initial values). The initial stresses were obtained by performing a quasi-static analysis to "turn-on" the gravity loads under aforementioned boundary conditions. Only the initial stresses at the end of the quasi-static analysis shown in Fig. 5.9 are utilized, while the same values for the degree of saturation, pore water pressure, void ratio, and nodal coordinates as the initial ones are adopted. The embankment is subjected to a horizontal base motion as shown in Fig. 5.8.

5.4.2 Results and Discussion

The dynamic simulation results with and without hysteresis are investigated by comparing the predicted horizontal and vertical displacements, pore water pressure, pore air pressure, and suction at various locations of the embankment. In these figures, the solid lines refer to the predicted results with non-hysteretic SWCC (NH), whereas the dashed lines refer to the predicted results with hysteretic SWCCs (H).

Figs. 5.10, 5.11, and 5.12 present the time histories of the predicted horizontal and vertical displacements at nodes N97 and N112, which are located at a height of 5.0 m on the sides of the embankment, and at node N210, which is located at the top surface of the embankment (see Fig. 5.7). Although the predicted displacements in these two analyses show similar trends at these three nodes, the final vertical displacements are smaller at nodes N97 and N112 than that at node N210. The comparative plots of the vertical displacement history at these three nodes indicate that the vertical displacements predicted in the case of the H simulation are similar to those predicted for the case of the NH simulation at the beginning of shaking, whereas the differences between these two simulations consistently increase as the time increases. The largest difference is observed at node N210. The final horizontal displacement at node N97 and N112 is slightly larger than that at node N210. No noticeable differences in predicted horizontal displacements by the H and NH simulations are observed at these three nodes. Although the difference in vertical displacements between these two simulations is less than 8%, the incorporation of the hydraulic hysteresis in the fully coupled flow-

deformation analysis provides a valuable insight into the understanding of dynamic behavior of unsaturated soils.

The predicted pore air and water pressure, suction, and volumetric water content at elements E8 and E63 are compared in Fig. 5.13 and Fig. 5.14, respectively. The pore water and pore air pressures display the ascending trend during shaking at these two selected elements. It was also found by Khoei and Mohammadnejad (2011) that the excess pore water and air pressure at various locations of the lower San Fernando Dam during the 1971 earthquake displayed the same trend. At element E63, the amplitude of pore water and air pressures are smaller than those at element E8. Compared to the NH simulation, the H simulation predicts a larger increase in the pore water pressure and a smaller increase in pore air pressure, which leads to a larger reduction in suction. At the end of shaking, the suction is about 71.2% and 85.9% lower than that in NH analysis at E63 and E8, respectively. Larger amplitude of fluctuation in the pore water and air pressure due to the base shaking is observed at E63. The comparison of the suction distribution at the end of dynamic analysis $t = 12.6$ s is shown in Fig. 5.15. The comparison of the suction contours of these two analyses indicates a noticeable discrepancy. The predicted suctions in H simulation are lower than those in the analysis without hysteresis, especially in the center region of the embankment around the base. It can be concluded that the suction is overestimated in the dynamic analysis without considering the hydraulic hysteresis. This is consistent with the explanation reported by Shahbodagh-Khan et al. (2015) that a larger change in excess pore water pressure and suction levels was observed in the simulation with hydraulic hysteresis. For problems in which more wetting and drying cycles are created during dynamic loading, the

differences in suction between analyses with and without hysteresis are expected to be even larger. Fig. 5.16 presents the comparison of the volumetric water content distribution at the end of dynamic analysis $t = 12.6$ s. There is no significant difference in volumetric water content between these two analyses.

The time history of the predicted suction illustrates that the embankment undergoes a general increasing trend in soil moisture with some drying and wetting cycles. Fig. 5.17 illustrates how the hydraulic paths move on the SWCCs during shaking. Both analyses start from the same point on the drying boundary curve (Point A in Fig. 5.17). The drying and wetting during shaking occurs along different scanning curves (hydraulic path ADE) in the analysis with hydraulic hysteresis, while for the analysis without hysteresis, the point remains on and move along the drying bound curve (hydraulic path ABC).

It must be pointed out that, for a Minco silt unsaturated embankment, the predicted values in displacements using a single SWCC are reasonable, probably due to small incremental values in volumetric water content during shaking. However, it is not appropriate for predicting the suction. For different SWCC types and different soil types, additional research is needed.

5.5 Summary

A hysteresis model for SWCCs based on the bounding surface plasticity theory is implemented into the finite element code U_DYSAC2. The modified code is validated against experimental results for a soil column subjected to drying and wetting

cycles. The proposed model is then applied to study the dynamic behavior of an unsaturated soil embankment subjected to base shaking. Predictions using the hysteretic and non-hysteretic SWCCs are presented and compared.

Simulations results show that the vertical displacements predicted by considering the hydraulic hysteresis are larger than those predicted by the analysis without hysteresis, but there is no significant differences in horizontal displacements between these two analyses. It can also be concluded that both the hysteresis and non-hysteresis analyses predict increases in pore water and pore air pressures during shaking. The predicted suction reduction is, however, larger for analysis with hysteresis. The volumetric water content is slightly overestimated in the analysis without hysteresis. The state of the soil moved along different scanning curves during shaking in the analysis with hysteresis, while it moved along the boundary drying curve in the analysis without hysteresis. This difference can result in large differences in dynamic response and therefore it is important to take into account the hydraulic hysteresis in the dynamic analysis of unsaturated soils. Although further studies in other soils are needed to be conducted to validate the conclusions previously mentioned, the fully coupled flow-deformation analysis developed in this research provides valuable insight into the dynamic behavior of unsaturated soils including the hydraulic hysteresis.

Table 5.1 Local solution procedure of SWCCs

Step	Description
	Known: $n_{w,n}$, $\Delta s_c = s_{c,n+1} - s_{c,n}$ and $\Gamma\left(n_{w,n}, s_{c,n}\right)$
	Search: $n_{w,n+1}$
1	Determine the drying-wetting path according to Δs_c
2	Set $n_{w,n+1}^{(0)} = n_{w,n} + \Delta s_c \Big/ \Gamma\left(n_{w,n}, s_{c,n}\right)$
3	For $i <$ max iteration number, compute $\Gamma\left(n_{w,n+1}^{(i)}, s_{c,n+1}\right)$ and the residual $r = n_{w,n+1}^{(i)} - n_{w,n} - \Delta s_c \Big/ \Gamma\left(n_{w,n+1}^{(i)}, s_{c,n+1}\right)$
4	Check convergence: given a tolerance value TOL, if $\lvert r \rvert \le TOL$ go to Step 6
5	If $\lvert r \rvert > TOL$, compute $\delta n_{w,n+1}^{(i)} = -r \Big/ \left(1 + \frac{\Delta s_c}{\Gamma^2} \frac{\partial \Gamma}{\partial n_w}\right)$ $n_{w,n+1}^{(i+1)} = n_{w,n+1}^{(i)} + \delta n_{w,n+1}^{(i)}$ Go to Step 3
6	Update $n_{w,n+1} = n_{w,n+1}^{(i)}$

Table 5.2 Material properties for Dune sand

Properties	Symbol	Value	Unit
Young's modulus	E	6	MPa
Poisson ratio	v	0.2	-
Porosity	n	0.301	-
Density of solid skeleton	ρ_s	2600	kg/m^3
Density of water	ρ_w	1000	kg/m^3
Density of air	ρ_a	1.22	kg/m^3
Bulk modulus of air	K_a	1×10^2	kPa
Bulk modulus of water	K_w	2.2×10^6	kPa
Intrinsic permeability	k	6.6×10^{-12}	m^2
Viscosity of water	μ_w	1×10^{-6}	kPa·s
Viscosity of air	μ_a	1.8×10^{-8}	kPa·s
Empirical parameter	m	0.83	-
Gravitational acceleration	g	9.81	m/s^2

Table 5.3 Material properties for Minco silt

Properties	Symbol	Value	Unit
Porosity	n	0.4132	-
Density of solid skeleton	ρ_s	2680	kg/m^3
Density of water	ρ_w	1000	kg/m^3
Density of air	ρ_a	1.22	kg/m^3
Bulk modulus of air	K_a	1.01×10^{2}	kPa
Bulk modulus of water	K_w	2.2×10^{6}	kPa
Intrinsic permeability	k	1.04×10^{-13}	m^2
Viscosity of water	μ_w	1×10^{-6}	kPa·s
Viscosity of air	μ_a	1.8×10^{-8}	kPa·s
Material parameter	m	6.02	-

Table 5.4 Model parameters for Minco silt

Symbol	Physical meaning	Value
SWCCs Model Parameters		
b_2	Location of bounding wetting curve in n_w - s_c space	8.6
d_2		0.7
b_3	Location of bounding drying curve in n_w - s_c space	100
d_3		0.5
I^e	Capillary elastic modulus (kPa)	-2500
H	Hardening shape parameter	5.0
n_{ws}	Saturated volumetric water content	0.413
n_{wr}	Residual volumetric water content	0.001
Traditional Model Parameters		
λ	Slope of isotropic consolidation line o	0.04
κ	Slope of elastic rebound line	0.004
M_c	Slope of critical state line (CSL) in compression	1.268
M_e/M_c	Ratio of extension to compression value of M	1.0
ν	Poisson ratio	0.2
P_L	Transitional stress	33.8
Bounding Surface Configuration Parameters		
T	Parameter defining ellipse 2	0.01
R_c	Bounding surface shape parameter in compression	2.41
R_e/R_c	Ratio of triaxial extension to triaxial compression value of R	1.0
A_c	Value of parameter defining hyperbola in compression	0.05
A_e/A_c	Ratio of triaxial extension to triaxial compression value of A	1.0
S	Elastic nucleus paramter	1.03
C	Projection center parameter	0.0
Hardening Parameters		
m	Hardening parameter	0.02
h_c	Shape hardening parameter in compression	0.8
h_e/h_c	Ratio of extension to compression value of h	1.0
h_2	Shape hardening parameter on the I-axis	0.8
Suction Related parameters		
$\mu(s_c)$	Intersection of CSL on the J-axis	4.703
$N(s_c)$	Value of specific volume at reference pressure	1.752
$\alpha(s_c)$	Parameters accounting for variation of air void ratio	0.089
$A(s_c)$	with suction	0.359
$r(s_c)$	Parameters accounting for variation of λ with suction	3.0
$\beta(s_c)$		0.5

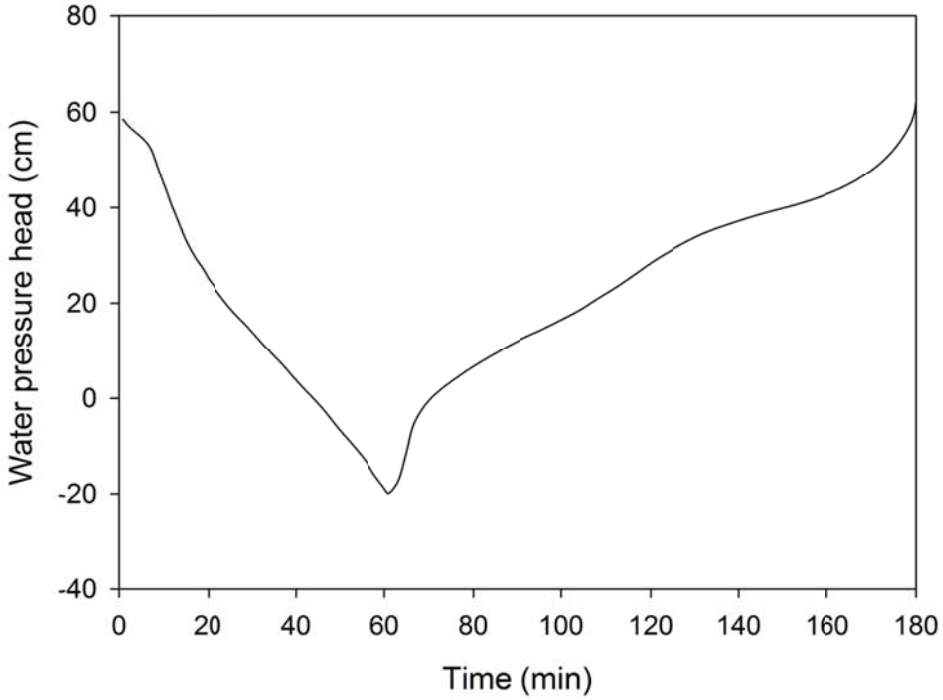

Fig. 5.1 Time history of water pressure head applied at the bottom of the Dune sand column

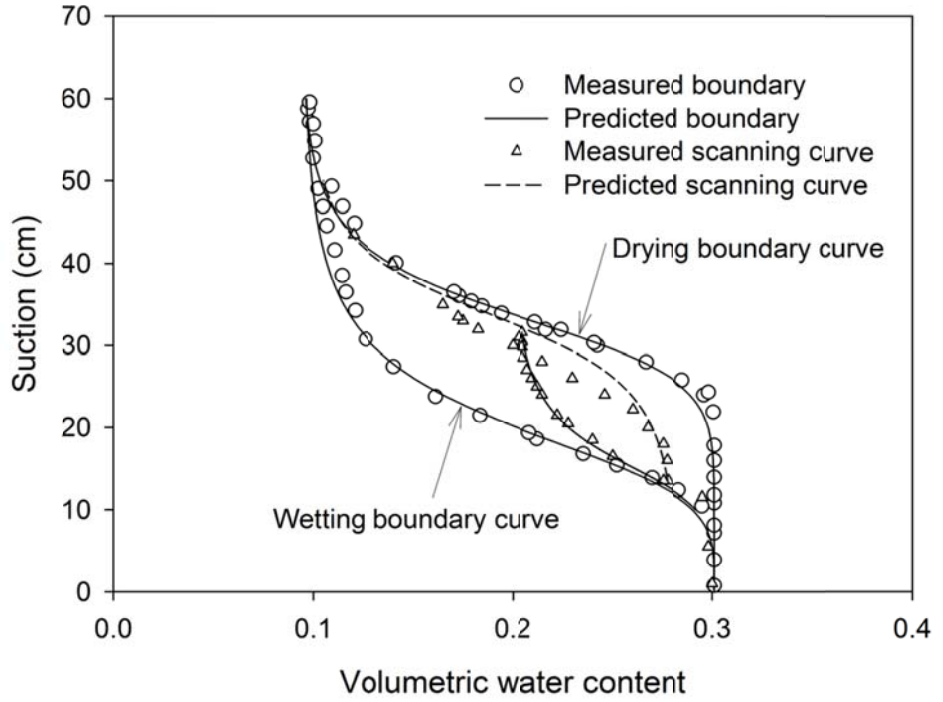

Fig. 5.2. Soil water characteristic curves of Dune sand

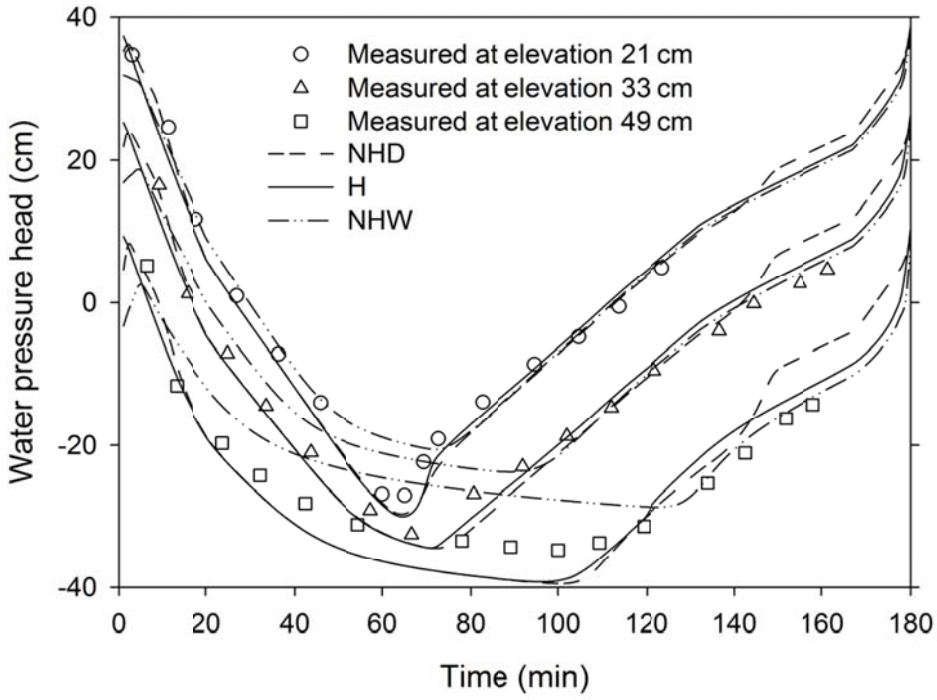

Fig. 5.3 Comparisons between measured and predicted water pressure head at different elevations

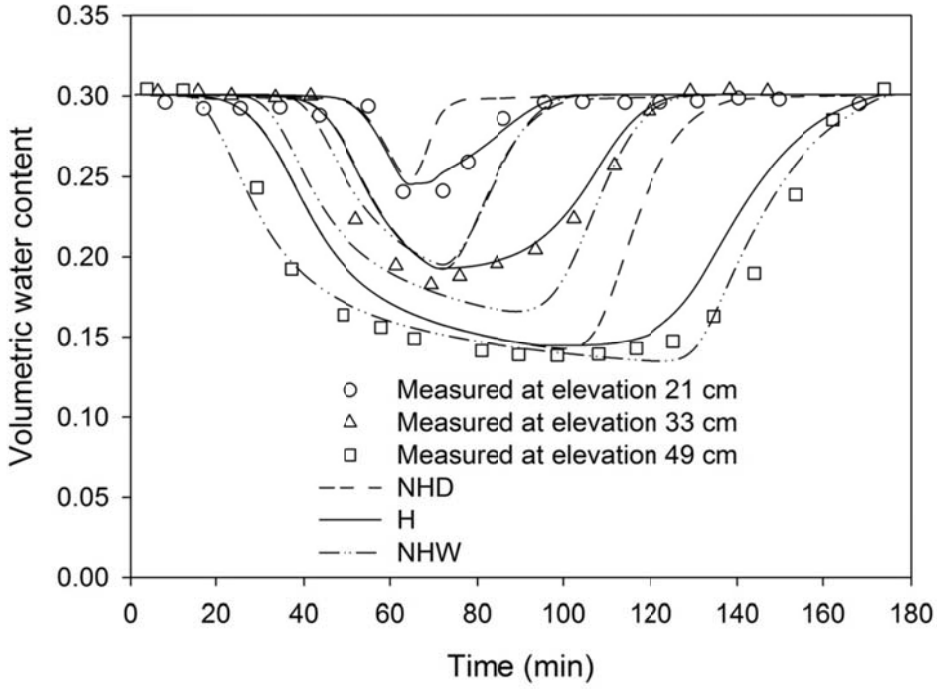

Fig. 5.4 Comparisons between measured and predicted water content at different elevations

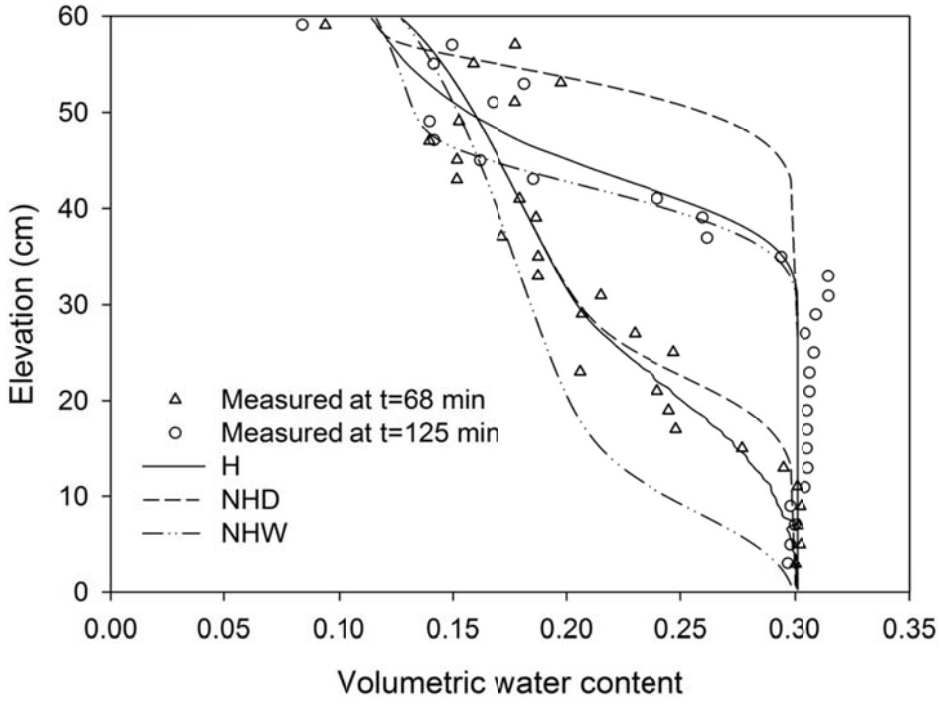

Fig. 5.5 Comparisons of measured and predicted water content profiles

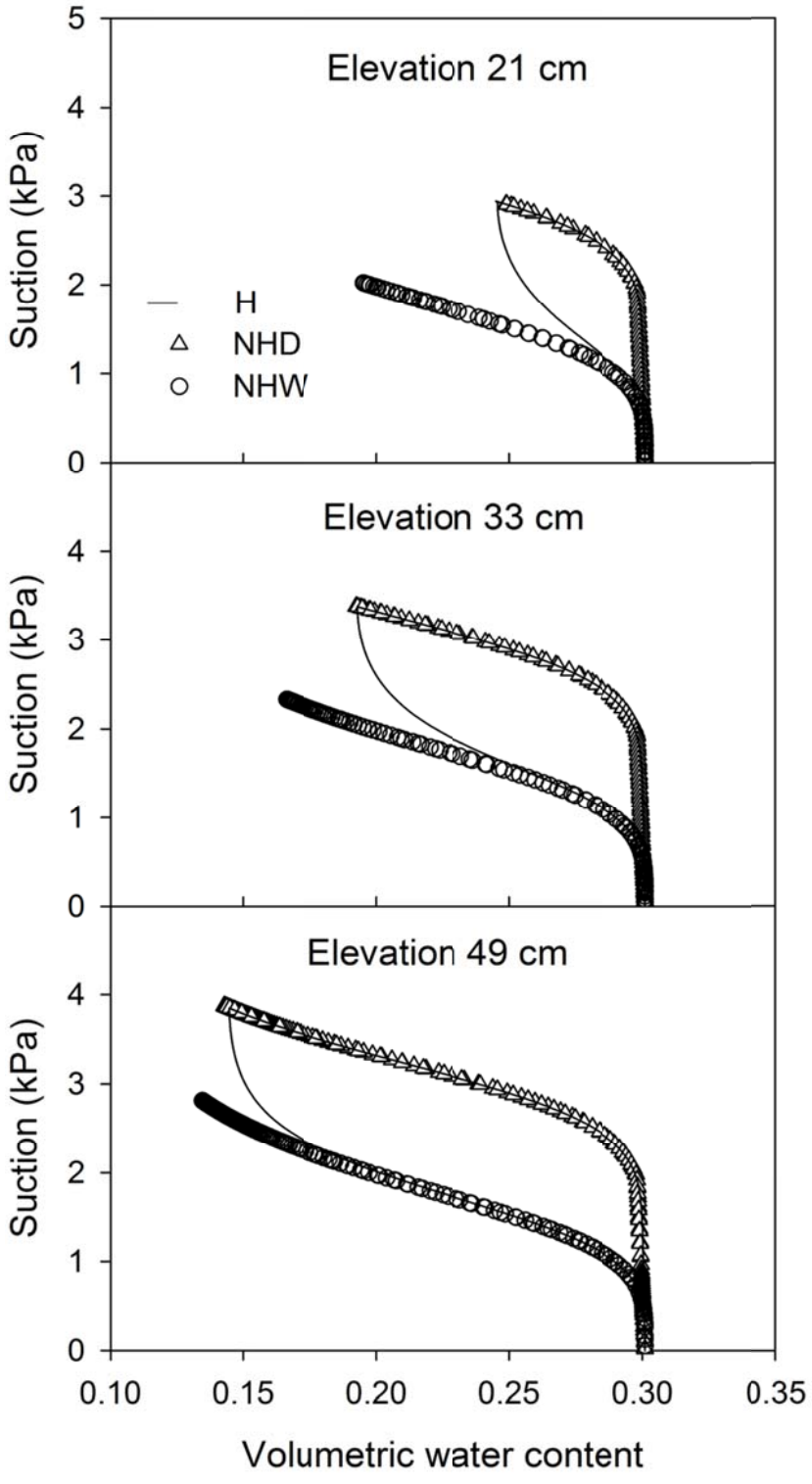

Fig. 5.6 Predicted hydraulic path at different elevations

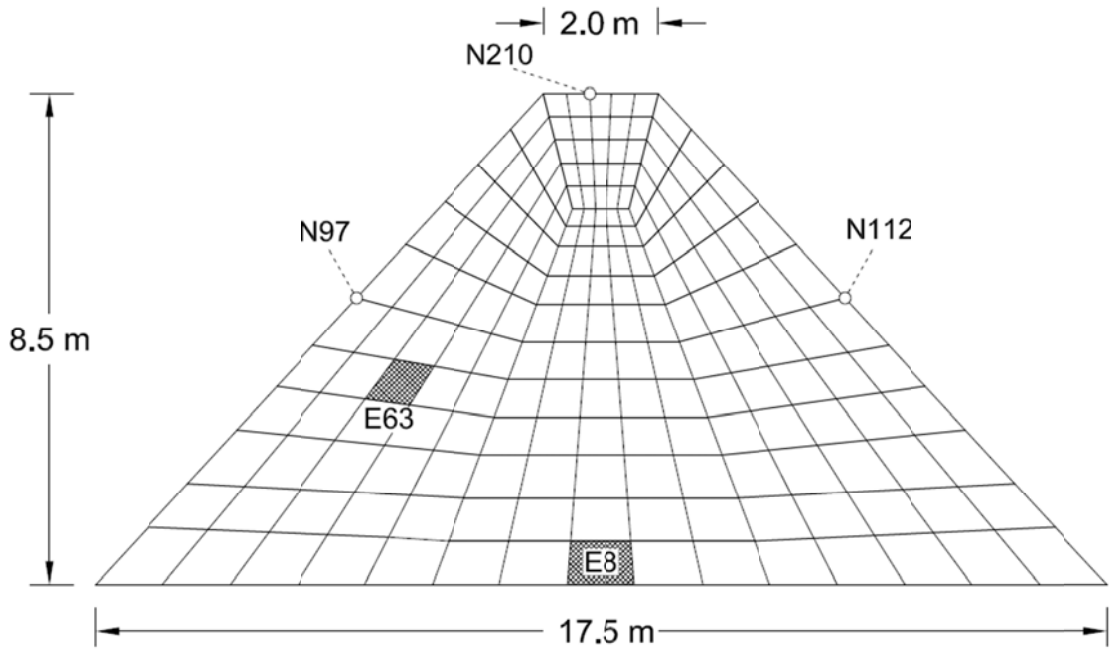

Fig. 5.7 Finite element mesh of the unsaturated soil embankment

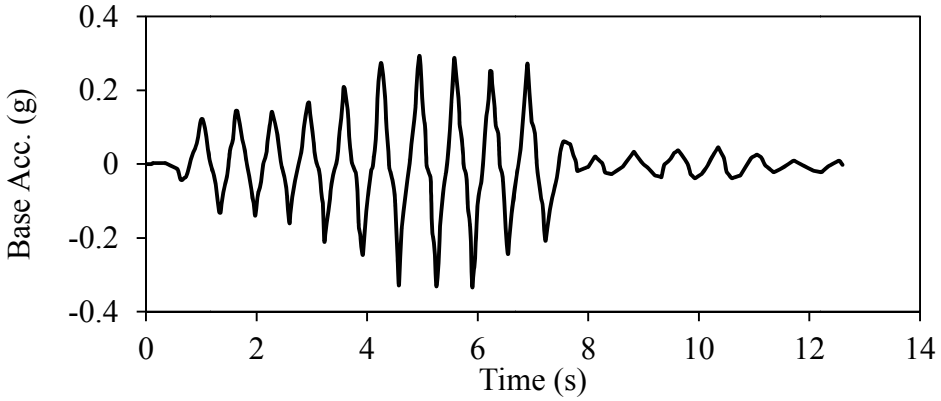

Fig. 5.8 Input horizontal base acceleration for the unsaturated soil embankment

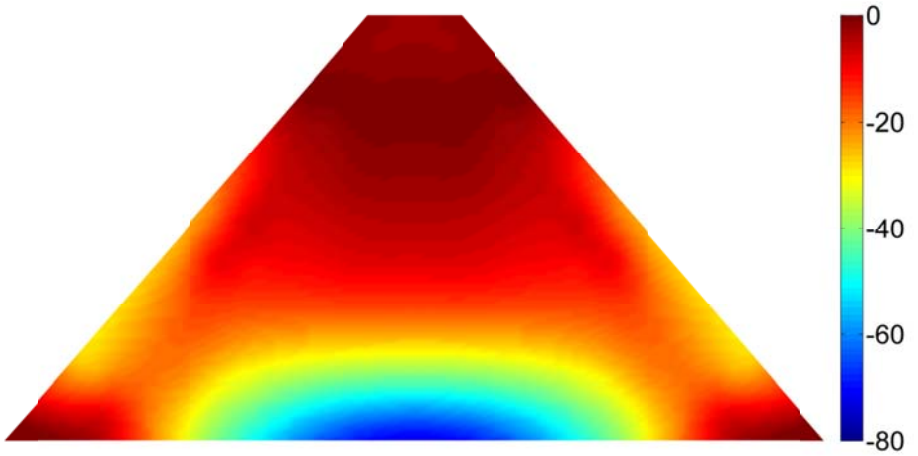

a) Contours of σ_x (kPa)

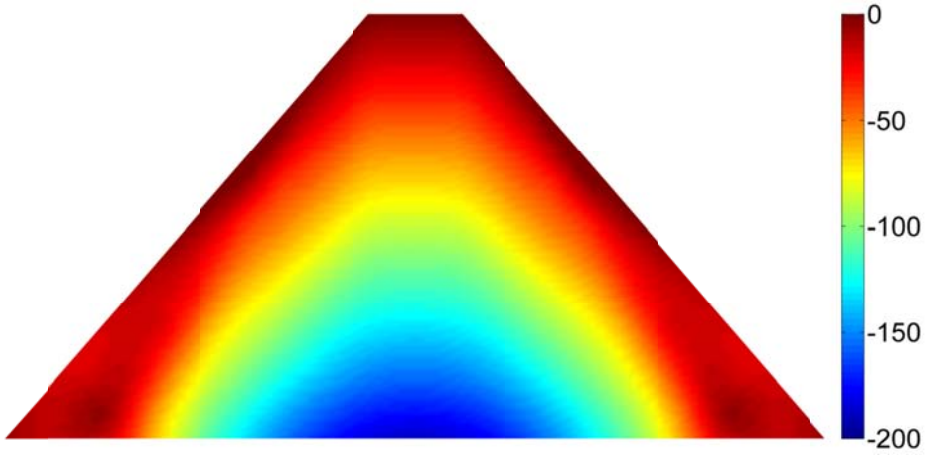

b) Contours of σ_y (kPa)

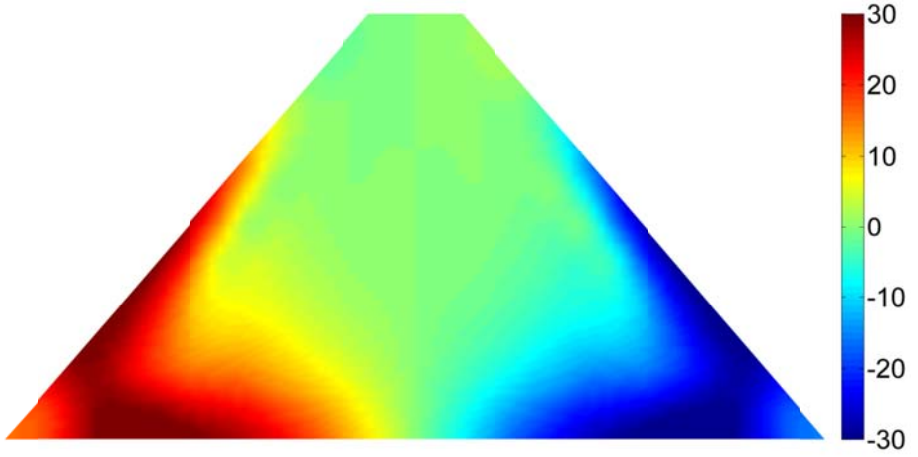

c) Contours of τ_{xy} (kPa)

Fig. 5.9 Initial stress contours for dynamic analysis

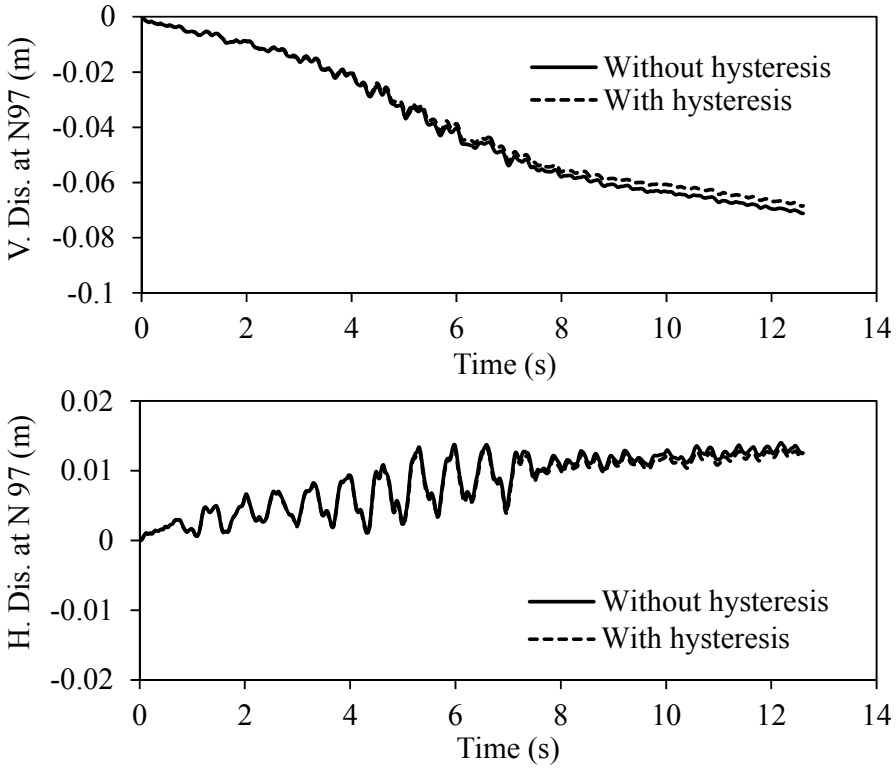

Fig. 5.10 Time histories of vertical and horizontal displacements at node N97

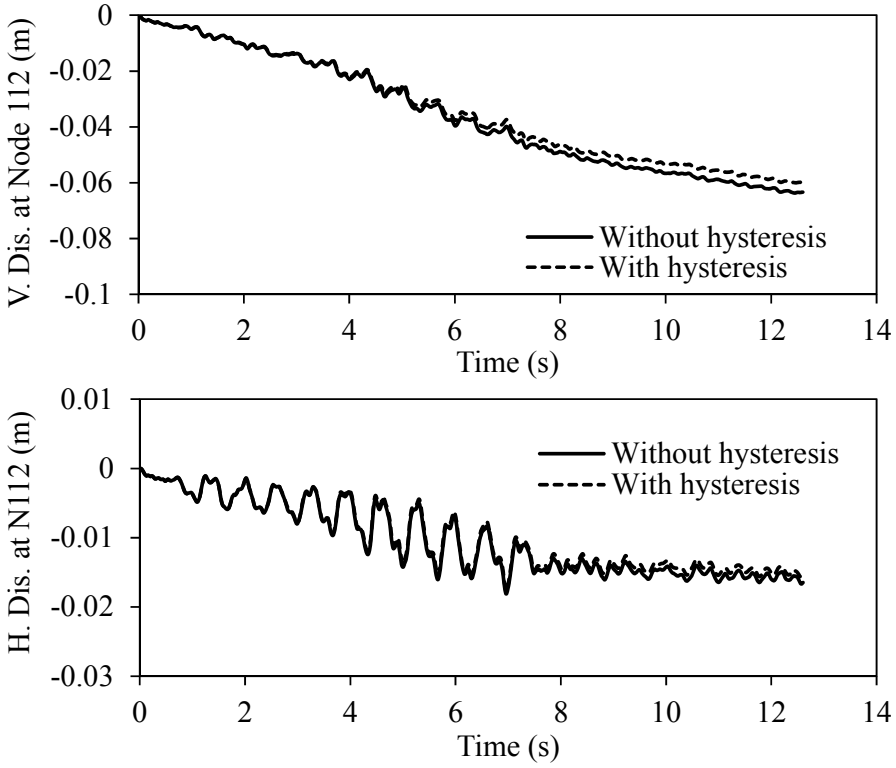

Fig. 5.11. Time histories of vertical and horizontal displacements at node N112

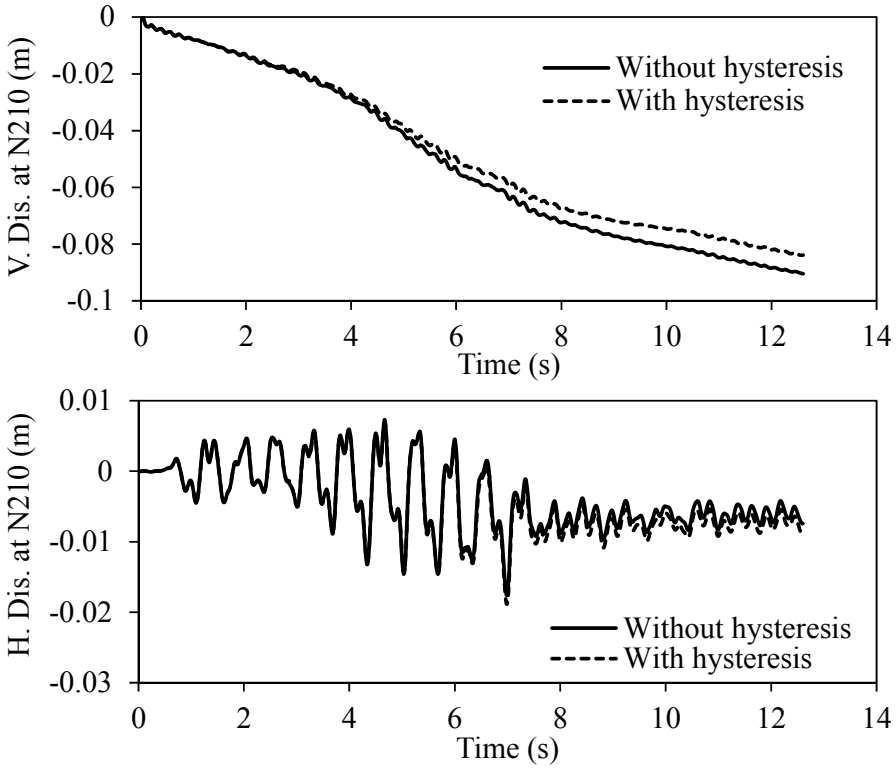

Fig. 5.12. Time histories of vertical and horizontal displacements at node N210

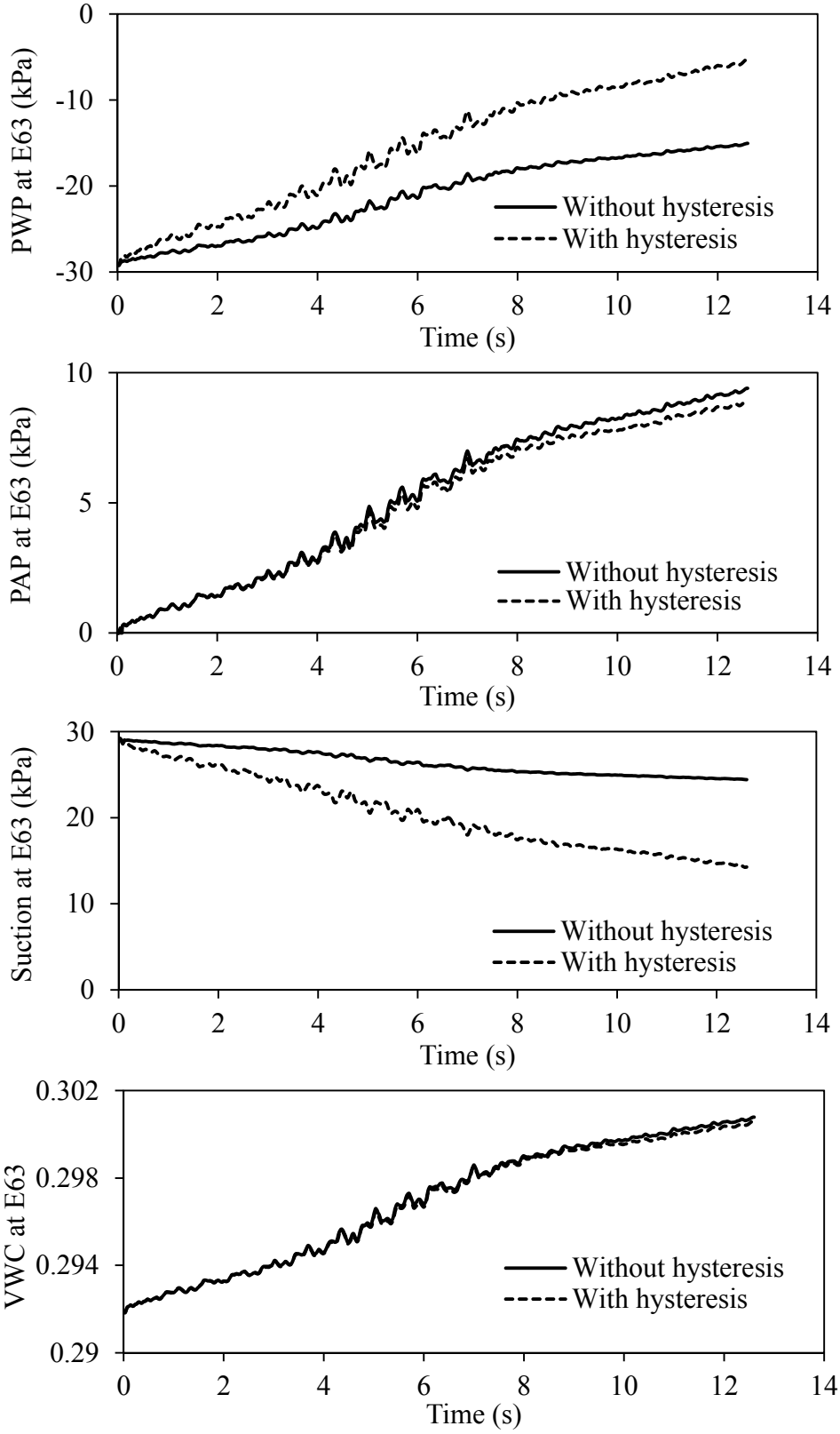

Fig. 5.13. Time histories of pore water and air pressure, suction and volumetric water content at element E63

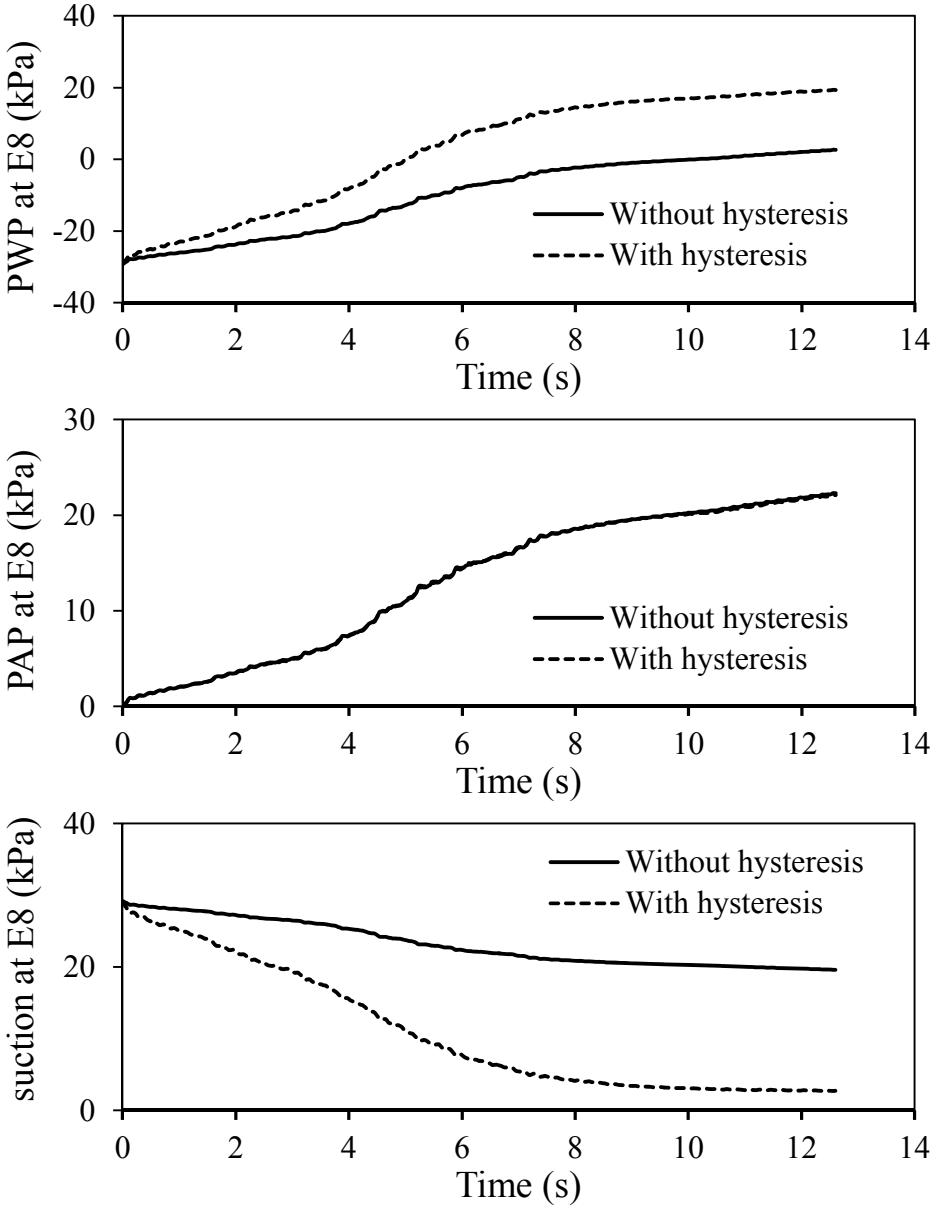

Fig. 5.14. Time histories of pore water pressure, pore air pressure and suction at element E8

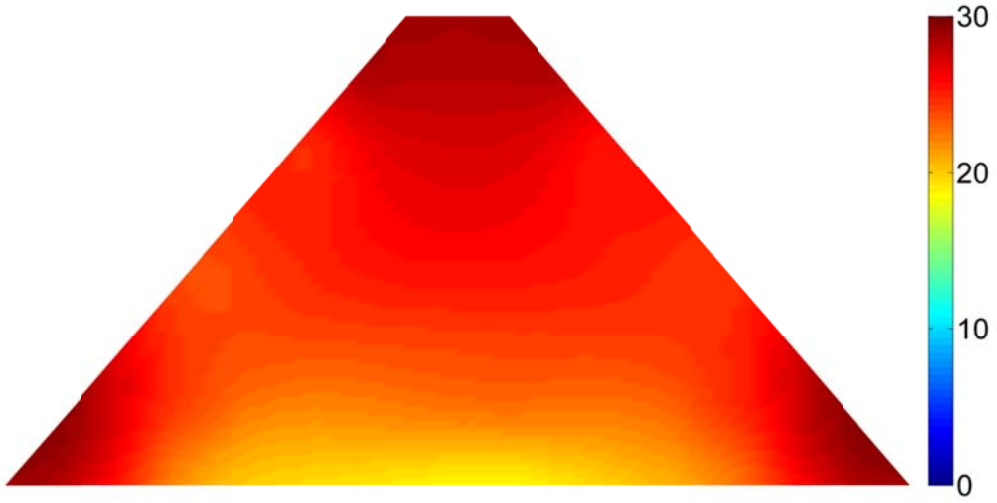

a) Without hysteresis

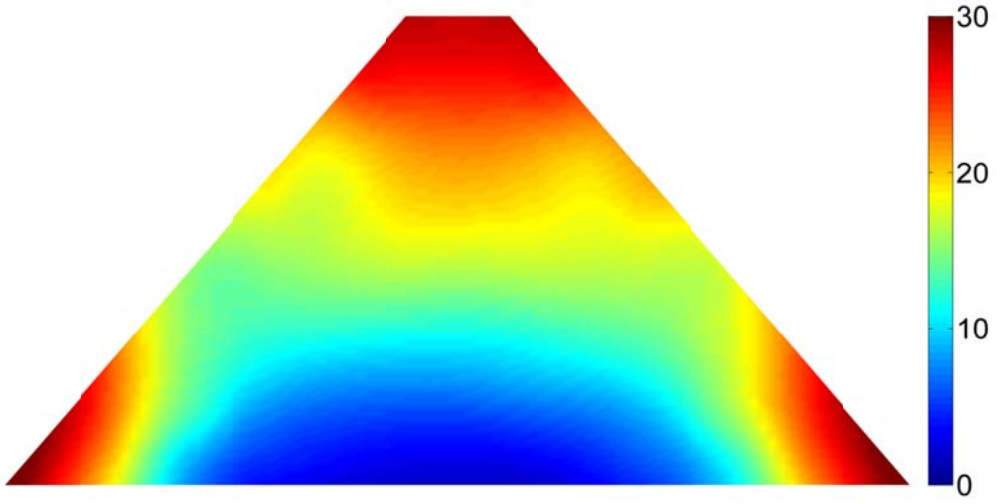

b) With hysteresis

Fig. 5.15 Distribution of suction (kPa) at 12.6 s

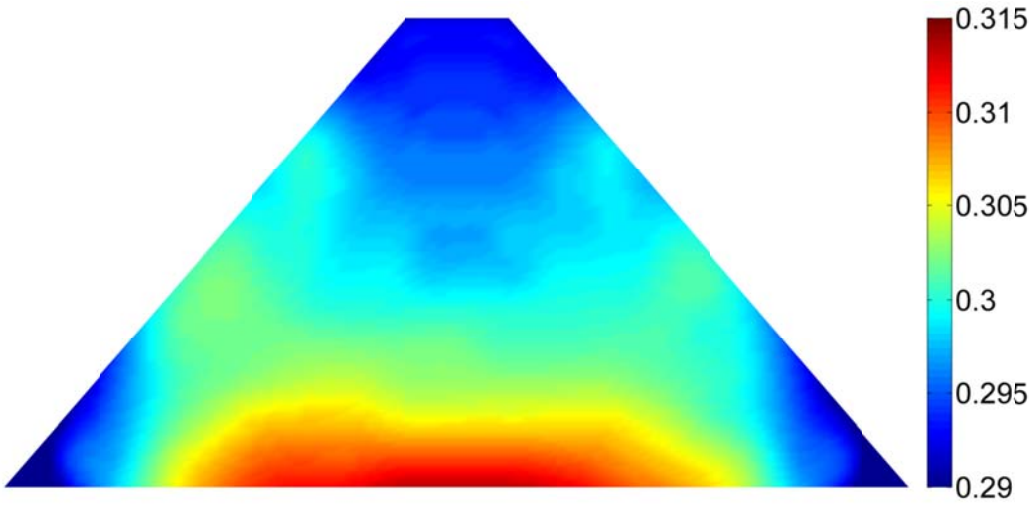

a) Without hysteresis

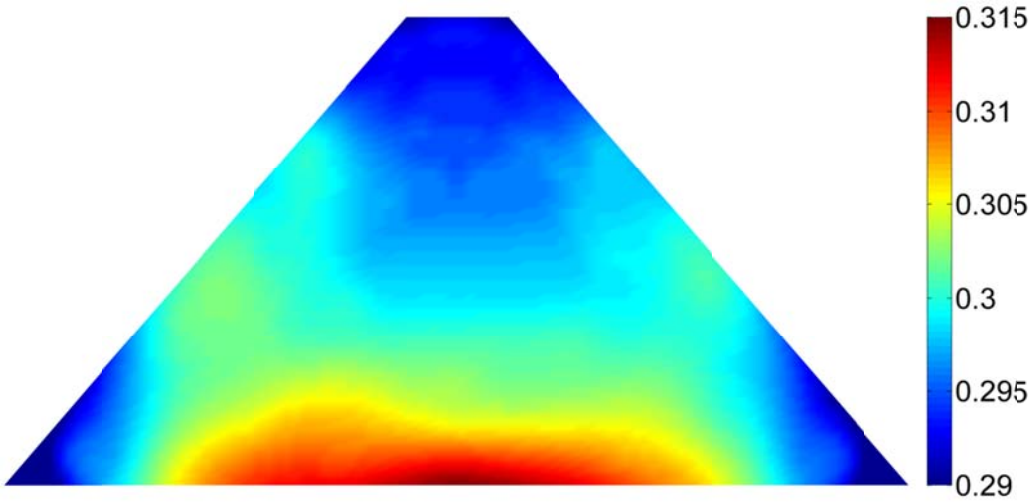

b) With hysteresis

Fig. 5.16 Distribution of volumetric water content at 12.6 s

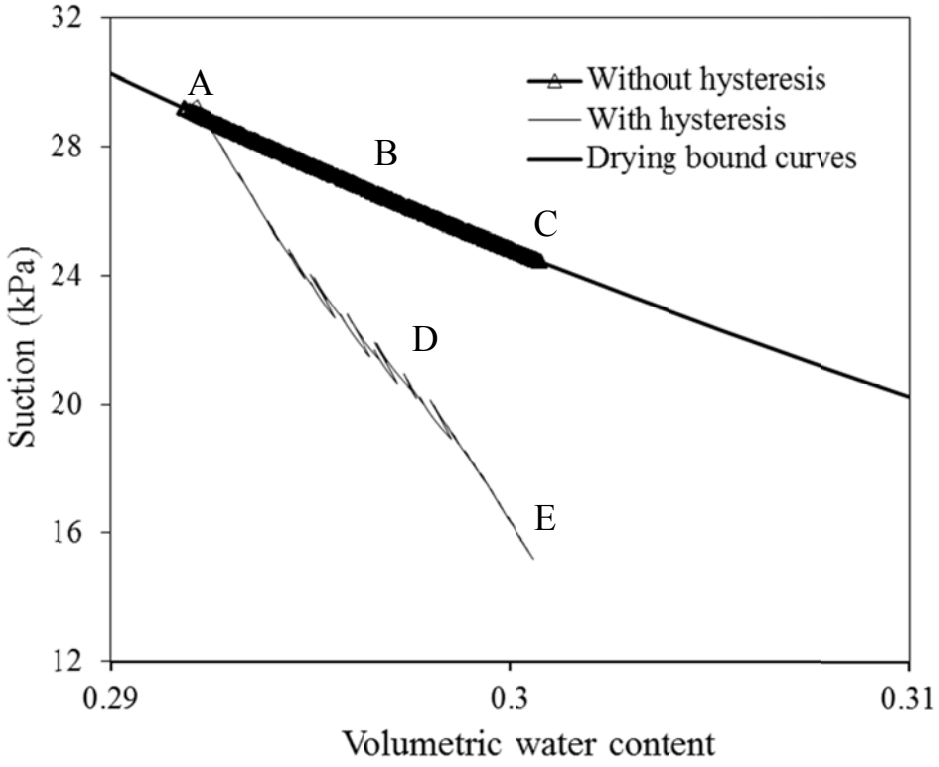

Fig. 5.17 Movement of hydraulic states at E63 on the SWCCs (Only portions of the bounding curves are shown)

CHAPTER 6 IMPLEMENTATION OF CM4USS AND VALIDATION

6.1 Introduction

CM4USS is implemented into U_DYSAC2 for predicting the seismic behavior of geotechnical engineering structures. The validation of implementation is provided using numerical examples. The effects of the degree of saturation and relative density on the liquefaction potential of level ground unsaturated sand deposits subjected to earthquakes are studied.

6.2 Implicit Integration of CM4USS

The solid displacements, pore water pressure, and pore air pressure are taken as nodal variables in the fully coupled equations developed in Chapter 4. The incremental displacements and pore air and water pressure can be obtained from the governing equations in every time step of the finite element analysis. The increments of strain $\Delta\boldsymbol{\varepsilon}$ at every integration points within every element can be determined using Eq. (4.9). The increments of suction Δs_c can be obtained using the incremental pore air and water pressure. The stress-strain state (I_n , $\mathbf{s}_n$, $\boldsymbol{\varepsilon}_n$, $s_{c,n}$, $n_{w,n}$), strain increment ($\Delta\boldsymbol{\varepsilon}$), and

suction increment (Δs_c) for the current time step t_n are assumed to be completely known. The updated values of I_{n+1}, $\mathbf{s}_{n+1}$, $n_{w,n+1}$ and internal variables for time step t_{n+1} are obtained from the respective known values at time t_n for a given increment of strain ($\Delta\boldsymbol{\varepsilon}$) and suction (Δs_c). The incremental strain and suction definied below can be obtained by solving the finite element equations,

$$\Delta\boldsymbol{\varepsilon}_{n+1} = \boldsymbol{\varepsilon}_{n+1} - \boldsymbol{\varepsilon}_n,\ \Delta s_{c,n+1} = s_{c,n+1} - s_{c,n} \tag{6.1}$$

The implicit integration algorithm, i.e., the closest point projection method (CPPM), which is a generalization of the backward Euler return rule to an arbitrary convex yield surface has been previously used in some unsaturated soil constitutive models (e.g., Macari et al., 2003). CPPM is adopted to integrate the constitutive model in this research.

In the predictor /multi-corrector algorithm, the constitutive model is called to solve all the quantities at time t_{n+1}. It is different from the assumption in Liu and Muraleetharan (2012b) that stress-strain state, strain increment, and volume fraction of water increment are given at time t_n . So the integration process in Liu and Muraleetharan (2012b) is modified. The integration procedure of numerical implementation of CM4USS is shown in Table 6.1.

6.2.1 Elastic Predictor

$$I_{n+1}^{trial} = \left[\left(I_n \right)^{(1-b_1)} + \frac{K_0 \left(1-b_1\right)}{p_{ref}^{b_1}} \Delta\varepsilon_{v,n+1} \right]^{1/(1-b_1)} \tag{6.2}$$

$$\mathbf{s}_{n+1}^{trial} = \mathbf{s}_n + 2G_0 \left(\frac{I_{n+1}}{p_{ref}} \right)^{d_1} \Delta\boldsymbol{\varepsilon}_{q,n+1} \tag{6.3}$$

$$n_{w,n+1}^{trial} = n_{w,n} + \frac{\Delta s_{c,n+1}}{\Gamma^e} \tag{6.4}$$

$$\boldsymbol{\alpha}_{n+1}^{trial} = \boldsymbol{\alpha}_n, \; m_{n+1}^{trial} = m_n \tag{6.5}$$

$$\text{Wetting: } s_{c0w,\,n+1}^{trial} = s_{c0w,n} \quad \text{Drying: } s_{c0d,\,n+1}^{trial} = s_{c0d,n} \tag{6.6}$$

If the yield surface function $f\left(\boldsymbol{\sigma}', s_c; \boldsymbol{\alpha}, m\right) < 0$, then the trial stress state is accepted as the new stress state. If $f\left(\boldsymbol{\sigma}', s_c; \boldsymbol{\alpha}, m\right) > 0$, it is necessary to correct the elastic predictions by simultaneously satisfying all the rate equations.

6.2.2 Plastic Corrector

The plastic correction is done by making all of the following residual vectors zero considering the trial stresses as the initial condition (m represents the step number in the iteration).

$$\bar{R}_1 = I_{n+1}^{(m)} - \left[\left(I_n \right)^{(1-b_1)} + \frac{K_0 \left(1-b_1\right)}{p_{ref}^{b_1}} \left(\Delta\varepsilon_{v,n+1} - \Delta\varepsilon_{v,n+1}^{p(m)} \right) \right]^{1/(1-b_1)} \tag{6.7}$$

$$\bar{R}_2 = \Delta\varepsilon_{v,n+1}^{p(m)} - \Lambda_{n+1}^{(m)} D_{n+1}^{(m)} \tag{6.8}$$

$$\bar{\mathbf{R}}_3 = \mathbf{s}_{n+1}^{(m)} - \mathbf{s}_n - 2G_{n+1}^{(m)}\left(\Delta\boldsymbol{\varepsilon}_{q,n+1} - \Delta\boldsymbol{\varepsilon}_{q,n+1}^{p(m)}\right) \tag{6.9}$$

$$\bar{\mathbf{R}}_4 = \Delta\boldsymbol{\varepsilon}_{q,n+1}^{p(m)} - \Lambda_{n+1}^{(m)}\mathbf{n}_{n+1}^{(m)} \tag{6.10}$$

$$\bar{R}_5 = \Delta n_{w,n+1}^{p(m)} - \Delta s_{c,n+1} / \Gamma_{n+1}^{p(m)} \tag{6.11}$$

$$\bar{\mathbf{R}}_6 = \boldsymbol{\alpha}_{n+1}^{(m)} - \boldsymbol{\alpha}_n - \Lambda_{n+1}^{(m)} h_{n+1}^{(m)} \mathbf{b}_{n+1}^{(m)} \tag{6.12}$$

$$\bar{R}_7 = m_{n+1}^{(m)} - m_n - c_m\left(1+e_0\right)\Lambda_{n+1}^{(m)} D_{n+1}^{(m)} - c_v\left(\frac{s_{c,n+1}^{(m)} n_{w,n+1}^{(m)}}{p_{ref}}\right)^{\varpi} \Delta n_{w,n+1}^{p(m)} \tag{6.13}$$

$$\bar{\mathbf{R}}_8 = \mathbf{F}_{n+1}^{(m)} - \mathbf{F}_n + \Lambda_{n+1}^{(m)} c_f < -D_{n+1}^{(m)} > \left(F_{\max}\mathbf{n}_{n+1}^{(m)} + \mathbf{F}_{n+1}^{(m)}\right) \tag{6.14}$$

$$\bar{R}_9 = s_{c0w,n+1}^{(m)} - s_{c0w,n} \exp\left[\zeta v_{n+1}^{(m)} \Delta\varepsilon_{v,n+1}^{p(m)} - \frac{1}{d_2}\frac{\left(n_{ws,n+1} - n_{wr,n+1}\right)\Delta n_{w,n+1}^{p(m)}}{\left(n_{ws,n+1} - n_{w,n+1}^{(m)}\right)\left(n_{w,n+1}^{(m)} - n_{wr,n+1}\right)}\right] \tag{6.15}$$

$$\bar{R}_{10} = s_{c0d,n+1}^{(m)} - s_{c0d,n} \exp\left[\zeta v_{n+1}^{(m)} \Delta\varepsilon_{v,n+1}^{p(m)} - \frac{1}{d_3}\frac{\left(n_{ws,n+1} - n_{wr,n+1}\right)\Delta n_{w,n+1}^{p(m)}}{\left(n_{ws,n+1} - n_{w,n+1}^{(m)}\right)\left(n_{w,n+1}^{(m)} - n_{wr,n+1}\right)}\right] \tag{6.16}$$

$$\bar{R}_{11} = \sqrt{\mathbf{r}_{n+1}^{(m)} : \mathbf{r}_{n+1}^{(m)}} - \sqrt{\frac{2}{3}} m_{n+1}^{(m)} I_{n+1}^{(m)} \sqrt{1 - \left(I_{n+1}^{(m)} / I_0\right)^{\beta}} \tag{6.17}$$

Equations (6.7)-(6.17) represents a system of nonlinear equations with unknowns

$$\mathbf{U} = \{ I_{n+1}^{(m)}, \Delta\varepsilon_{v,n+1}^{p(m)}, \mathbf{s}_{n+1}^{(m)}, \Delta\boldsymbol{\varepsilon}_{q,n+1}^{p(m)}, \Delta n_{w,n+1}^{p(m)}, \boldsymbol{\alpha}_{n+1}^{(m)}, m_{n+1}^{(m)}, \mathbf{F}_{n+1}^{(m)}, s_{c0w,n+1}^{(m)}, s_{c0d,n+1}^{(m)}, \Lambda_{n+1}^{(m)} \} \tag{6.18}$$

The implicit step-by-step integration procedure of the constitutive model CM4USS is given in Table 6.1.

6.2.3 Stress Update Algorithm

When $f\left(I_{n+1}^{trial}, \mathbf{s}_{n+1}^{trial}, s_{c,n+1}^{trial}; \boldsymbol{\alpha}_{n+1}^{trial}, m_{n+1}^{trial}\right) > 0$ and $\Delta s_{c,n+1} = 0$, the current skeleton stress state is on the yield surface. In order to obtain the incremental stress, plastic strains, and internal variables, the residual vector $\bar{\mathbf{R}}^1$ and unknown vector $\mathbf{U}^1$ need to be solved as follows:

$$\bar{\mathbf{R}}^1 = \{\bar{R}_1, \bar{R}_2, \bar{\mathbf{R}}_3, \bar{\mathbf{R}}_4, \bar{\mathbf{R}}_6, \bar{R}_7, \bar{\mathbf{R}}_8, \bar{R}_{11}\} \tag{6.19}$$

$$\mathbf{U}^1 = \{I_{n+1}^{(m)}, \Delta\varepsilon_{v,n+1}^{p(m)}, \boldsymbol{s}_{n+1}^{(m)}, \Delta\boldsymbol{\varepsilon}_{q,n+1}^{p(m)}, \boldsymbol{\alpha}_{n+1}^{(m)}, \Delta m_{n+1}^{(m)}, \mathbf{F}_{n+1}^{(m)}, \Lambda_{n+1}^{(m)}\} \tag{6.20}$$

The Jacobian matrix is $\mathbf{T}^1 = \dfrac{\partial \bar{\mathbf{R}}^1}{\partial \mathbf{U}^1}$. The incremental unknown vector $\Delta\mathbf{U}^{1(m)}_{n+1} = \{\Delta I_{n+1}^{(m)}, \Delta^2\varepsilon_{v,n+1}^{p(m)}, \Delta\mathbf{s}_{n+1}^{(m)}, \Delta^2\boldsymbol{\varepsilon}_{q,n+1}^{p(m)}, \Delta\boldsymbol{\alpha}_{n+1}^{(m)}, \Delta m_{n+1}^{(m)}, \Delta\mathbf{F}_{n+1}^{(m)}, \Delta\Lambda_{n+1}^{(m)}\}$ is a 28×28 matrix, and given by $\Delta\mathbf{U}^{1(m)}_{n+1} = -\left(\mathbf{T}^1\right)^{-1}\bar{\mathbf{R}}^{1(m)}_{n+1}$. The plastic corrector is triggered under constant suction, so effect of the mechanical and hydraulic behavior on the evolution of the wetting and drying bound suctions (s_{c0w} and s_{c0d}) is computed by

$$s_{c0d,n+1}^{(m)} = s_{c0d,n}\exp\left[\zeta v_{n+1}^{(m)}\Delta\varepsilon_{v,n+1}^{p(m)} - \frac{1}{d_3}\frac{\left(n_{ws,n+1} - n_{wr,n+1}\right)\Delta n_{w,n+1}^{p(m)}}{\left(n_{ws,n+1} - n_{w,n+1}^{(m)}\right)\left(n_{w,n+1}^{(m)} - n_{wr,n+1}\right)}\right] \tag{6.21}$$

$$s_{c0w,n+1}^{(m)} = s_{c0w,n}\exp\left[\zeta v_{n+1}^{(m)}\Delta\varepsilon_{v,n+1}^{p(m)} - \frac{1}{d_2}\frac{\left(n_{ws,n+1} - n_{wr,n+1}\right)\Delta n_{w,n+1}^{p(m)}}{\left(n_{ws,n+1} - n_{w,n+1}^{(m)}\right)\left(n_{w,n+1}^{(m)} - n_{wr,n+1}\right)}\right] \tag{6.22}$$

When $f\left(I_{n+1}^{(0)}, \mathbf{s}_{n+1}^{(0)}, s_{c,n+1}^{(0)}; \boldsymbol{\alpha}_{n+1}^{(0)}, m_{n+1}^{(0)}\right) < 0$ and $\Delta s_{c,n+1} \neq 0$, the current skeleton stress state is inside the yield surface. In order to obtain the increment of stress, plastic strains, and internal variables, the residual vector $\bar{\mathbf{R}}^2$ and unknown vector $\mathbf{U}^2$ need to be solved.

$$\bar{\mathbf{R}}^2 = \{\bar{R}_5, \bar{R}_7, \bar{R}_9, \bar{R}_{10}\} \tag{6.23}$$

$$\mathbf{U}^2 = \{\Delta n_{w,n+1}^{p(m)}, \Delta m_{n+1}^{(m)}, s_{c0w,n+1}^{(m)}, s_{c0d,n+1}^{(m)}\} \tag{6.24}$$

The Jacobian matrix $\mathbf{T}^2 = \dfrac{\partial \bar{\mathbf{R}}^2}{\partial \mathbf{U}^2}$. The incremental unknown vector $\Delta \mathbf{U}^{2(m)}_{n+1} = \{\Delta^2 n_{w,n+1}^{p(m)}, \Delta m_{n+1}^{(m)}, \Delta s_{0w,n+1}^{(m)}, \Delta s_{0d,n+1}^{(m)}\}$ is a 4×4 matrix and given by $\Delta \mathbf{U}^{2(m)}_{n+1} = -\left(\mathbf{T}^2\right)^{-1} \bar{\mathbf{R}}^{2(m)}_{n+1}$.

When $f\left(I_{n+1}^{(0)}, \mathbf{s}_{n+1}^{(0)}, s_{c,n+1}^{(0)}; \boldsymbol{\alpha}_{n+1}^{(0)}, m_{n+1}^{(0)}\right) > 0$ and $\Delta s_{c,n+1} \neq 0$, the current skeleton stress state is on the yield surface. In order to obtain the increment of stress and plastic strains and internal variables, the residual vector $\bar{\mathbf{R}}^3$ and unknown vector $\mathbf{U}^3$ need to be solved.

$$\bar{\mathbf{R}}^3 = \{\bar{R}_1, \bar{R}_2, \bar{\mathbf{R}}_3, \bar{\mathbf{R}}_4, \bar{R}_5, \bar{\mathbf{R}}_6, \bar{R}_7, \bar{\mathbf{R}}_8, \bar{R}_9, \bar{R}_{10}, \bar{\mathbf{R}}_{11}\} \tag{6.25}$$

$$\mathbf{U}^3 = \{I_{n+1}^{(m)}, \Delta \boldsymbol{\varepsilon}_{v,n+1}^{p(m)}, \mathbf{s}_{n+1}^{(m)}, \Delta \boldsymbol{\varepsilon}_{q,n+1}^{p(m)}, \Delta n_{w,n+1}^{p(m)}, \boldsymbol{\alpha}_{n+1}^{(m)}, m_{n+1}^{(m)}, \mathbf{F}_{n+1}^{(m)}, s_{c0w,n+1}^{(m)}, s_{c0d,n+1}^{(m)}, \Lambda_{n+1}^{(m)}\} \tag{6.26}$$

The Jacobian matrix is $\mathbf{T}^3 = \dfrac{\partial \bar{\mathbf{R}}^3}{\partial \mathbf{U}^3}$. The incremental unknown vector $\Delta \mathbf{U}^{3(m)}_{n+1} = \{\Delta I_{n+1}^{(m)}, \Delta^2 \boldsymbol{\varepsilon}_{v,n+1}^{p(m)}, \Delta \mathbf{s}_{n+1}^{(m)}, \Delta^2 \boldsymbol{\varepsilon}_{q,n+1}^{p(m)}, \Delta n_{w,n+1}^{p(m)}, \Delta \boldsymbol{\alpha}_{n+1}^{(m)}, \Delta m_{n+1}^{(m)}, \Delta \mathbf{F}_{n+1}^{(m)}, s_{c0w,n+1}^{(m)}, s_{c0d,n+1}^{(m)}, \Delta \Lambda_{n+1}^{(m)}\}$ is a

31×31 matrix and given by $\Delta \mathbf{U}_{n+1}^{3(m)} = -\left(\mathbf{T}^3\right)^{-1} \overline{\mathbf{R}}_{n+1}^{3(m)}$.

Because the s_c is known at time t_n, the mean intergranular confining stress I is related to the volumetric water content n_w^p. To avoid repetition, only the derivatives of $\mathbf{T} = \dfrac{\partial \overline{\mathbf{R}}}{\partial \mathbf{U}}$ different from those presented in Liu (2009) are included in this dissertation and shown in APPENDIX B.

6.3 Validation

6.3.1 1D Drying and Wetting of an Elastoplastic Soil Column

This simulation involving drying and wetting cycles was conducted to investigate the capability of the proposed model for predicting the hysteresis behavior. The numerical example presented in this section involved a 1 m high Nevada sand column with an initial degree of saturation of 94% and void ratio of 0.754 ($D_r = 50\%$). The bottom of the sand column was drained and subjected to a time history of pore water pressure $p_w(t)$ as shown in Fig. 6.1. The top and lateral boundaries were impervious to water and air. All the nodes were horizontally constrained and the ones at the bottom were also fixed vertically. The material properties for the unsaturated elastoplastic soil are shown in Table 6.2. The CM4USS parameters for Nevada sand were obtained from Table 3.2. The permeability of water k_w is 6.6×10^{-5} m/s for saturated soil (Arulmoli et al. 1992). Figs. 6.2, 6.3, and 6.4 present the predicted pore water pressure, suction, and volumetric water content, respectively, at different

elevations. The maximum volumetric water content at the end of the wetting stage is slightly smaller than that at the end of the previous wetting stage. The volumetric water content is not fully recovering due to the hydraulic hysteresis. The predicted hydraulic path at E2 and E20 is shown in Fig. 6.5. The hydraulic path is moving along the drying boundary curve in the first drying stages and then along different scanning curves in the following drying and wetting stages. The proposed model appears to be quite versatile to simulate the hydraulic hysteresis behavior.

6.3.2 Unsaturated Elastoplastic Soil under Uniform Loading

An unsaturated elastoplastic soil under uniform loading was analyzed to further explore the implementation of CM4USS. The finite element mesh is shown in Fig. 6.6. For the upper boundary, the air and water drainage were allowed. The remaining boundaries were imperious to air and water. The bottom boundary was constrained vertically and horizontally and the lateral boundaries were constrained horizontally. A time history of the uniform loading applied on the top boundary is shown in Fig. 6.6. The CM4USS parameters and the material properties were the same as those used in the analysis of 1D drying and wetting of a soil column problem.

The time history of the predicted vertical displacements at Node 42 and Node 21 are illustrated in Fig. 6.7. The displacements reach the maximum value at $t = 1$ min with a only minuscule change after that. Fig. 6.8, 6.9, and Fig. 6.10 show the time histories of the predicted pore water pressure, suction, and volumetric water content, respectively. It can be seen that pore water pressure and volumetric water content increase during the

loading and then decreases after $t = 1$ min. Suction displays an opposite trend. The predicted time histories of the pore water pressure, suction, volumetric water content, and displacements are reasonable.

6.3.3 Seismic Response of Level Ground Deposits of an Unsaturated Sand

Several simulations of level ground deposits of an unsaturated sand were conducted. A 10 m vertical column consisting of 20 elements subjected to the base motion is shown in Fig. 6.11. The elements are labeled from E1 (base) to E20 (top surface). The soil is assumed to be Nevada sand. Two relative densities of 40% and 60% corresponding to initial void ratios 0.798 and 0.712 were studied. Due to the lack of test results for SWCCs of Nevada sand at $D_r = 40\%$ and $D_r = 60\%$, all the SWCCs parameters except n_{ws} at $D_r = 40\%$ and $D_r = 60\%$ were assumed to be the same as those at $D_r = 50\%$. The n_{ws} at $D_r = 40\%$ and $D_r = 60\%$ were 0.44 and 0.416, respectively, which were obtained from the initial void ratios. All other CM4USS parameters are shown in Table 3.2. The material properties for Nevada sand are shown in Table 6.2. The boundary conditions are as follows: (1) the base motion was applied as a force vector that is equal to the base acceleration multiplied by the negative of the mass matrix, the base was impervious to both water and air and the bottom nodes were constrained in the vertical and horizontal directions relative to the base, (2) the lateral sides were impervious to both water and air and the displacements were connected to each other at a given depth level ensuring that the movements were identical, and (3) free drainage for water and air (i.e., the pore water and pore air pressure were kept constant as the initial values) and

zero tractions were specified on the top surface. The time history of the horizontal base motion (Fig. 6.12) recorded in the centrifuge experiment No.1 in the VELACS project by Taboada and Dobry (1993) was considered as the base motion. The maximum input horizontal acceleration is 0.23g.

A quasi-static application of gravity was analyzed to obtain the initial stress state. A large value of the permeability coefficient and a small value of bulk modulus of water were used in order to avoid pore water pressure generation and change in degree of saturation during the quasi-static analysis. Only the stresses at the end of quasi-static analysis served as the initial stresses for the subsequent dynamic analysis, while the same values for the degree of saturation, void ratio, and nodal coordinates as the initial ones were adopted. In order to study the influence of degree of saturation and relative density on the liquefaction potential of a level ground deposit of an unsaturated sand, five different degrees of saturation (60%, 85%, 90%, 95% and 98%) and two relative densities (40% and 60%) were examined and the results from selected elements along the soil profile are described below.

The time histories of predicted horizontal acceleration in elements E20, E16, and E12 along the soil profile at degrees of saturation of 98% and 85% are shown in Fig. 6.13. The predicted accelerations are slightly amplified at different depths and the extent of amplifications increases slightly towards the ground surface. This amplification in acceleration magnitude from the base to the top surface was consistent with the centrifuge test results of an unsaturated sand deposit during shaking observed by Ghayoomi et al. (2011). It is to be noted that the amplification is observed in the first three seconds of the shaking in E20 at 98% degree of saturation and the motion is

considerably reduced afterwards. The motion continues to be strong in E20 at 85% degree of saturation through the shaking. The significant reduction in the acceleration in E20 at 98% degree of saturation after three seconds is due to the occurrence of liquefaction.

Fig. 6.14 displays the time histories of the predicted horizontal displacements (H. dis.) and vertical displacement (V. dis.) at selected nodes N42 ($y = 10$ m), N34 ($y = 8$ m), N26 ($y = 6$ m), and N18 ($y = 4$ m) along the soil profile at a degree of saturation of 98%. The maximum permanent horizontal displacement (7.8 cm) and vertical displacement (2 cm) occur at the top surface (N42, $y = 10$ m). Smaller horizontal displacements are observed at other elevations. The time histories of horizontal and vertical displacements at the top surface of the soil column at different degrees of saturation are compared in Fig. 6.15 and Fig. 6.16, respectively. The final horizontal displacements at the top surface after shaking are larger in the wetter soils, except the case of 98% degree of saturation. For 98% degree of saturation, larger horizontal displacements are predicted earlier in the shaking. It can be seen form Fig. 6.16 that the vertical displacement is significantly influenced by the degree of saturation and the higher the degree of saturation, the lower the vertical displacement. It can also be seen from Fig. 6.16 that the effect of the degree of saturation on the vertical displacement is more pronounced for high values of degree of saturation. For example, a 3% drop (from 98% to 95%) in degree of saturation results in about 58.2% increase in the vertical displacement, while there is only 7.4% increase in vertical displacement when degree of saturation changes from 90% to 85%. While the horizontal displacements are influenced by stiffness of the sand, the collapse of air-filled voids causes the vertical displacement

during shaking. Larger air voids lead to larger settlements for lower degrees of saturation. This finding is consistent with Sawada et al. (2006) for triaxial tests on unsaturated sandy soils under irregular wave forms. After shaking, only a slight time-dependent vertical displacement is observed because of the dissipation of excess pore water pressure.

The variations of mean intergranular stress versus shear stress in selected elements for 98% degree of saturation and 40% relative density are described in Fig. 6.17. A cyclic decrease in mean intergranular stress towards zero can be observed due to the reduction in suction in many of the elements (see Fig. 6.18).

Fig. 6.19 and Fig. 6.20 compare the time histories of pore water and air pressure in E16 at different degrees of saturation. The pore water and air pressure in E16 increase during the shaking at different degrees of saturation and dissipate slightly at 98% and 95% degrees of saturation. For the soils with a higher degree of saturation, larger pore water pressure and pore air pressure are generated.

Fig. 6.21 shows the time histories of normalized vertical intergranular stress (VIS), σ_v'/σ_{v0}' (σ_v' is vertical intergranular stress), in selected elements along soil profiles at degree of saturation of 98%. In Chapter 3, the soil is assumed to have reached initial liquefaction when the effective mean stress reaches a value of 10% of the initial value because it is difficult to precisely discern the value of zero in effective mean stress in testing and simulations. In this section, the soil is assumed to have reached initial liquefaction when the normalized VIS reaches a value of 5% of the initial value, i.e., $\sigma_v'/\sigma_{v0}' = 0.05$. The normalized VIS at E19, E18, E17, and E16 are less than 0.05 and liquefaction occurs at $t = 2.1$, 3.4 , 4.5, and 7.0 s, respectively. Liquefaction is

observed down to a depth of 2.5 m. Following the initial liquefaction the normalized VIS time histories are characterized by a small fluctuation about value of zero. To study the effect of degree of saturation, the time histories of the normalized VIS in E19 and E16 at different degrees of saturation are compared in Fig. 6.22. For element E19 at degrees of saturation of 98%, 95%, 90%, and 85%, liquefaction occurs after approximately 2.1 s, 4.2 s, 7.4 s, and 9.9 s, respectively. However, the liquefaction is only observed in E16 at a degree of saturation of 98% after 6.8 s. For an unsaturated element at a given elevation, the normalized VIS increases as the degree of saturation decreases at a given time of the shaking. It indicates that the lower the degree of saturation and the higher the initial VIS, the higher liquefaction resistance. The minimum normalized VIS in the soil column at different degrees of saturation during the shaking is compared in Fig. 6.23. It can be seen that the thickness of liquefied layer decreases as degree of saturation decreases. For example, the thickness of liquefied layer is about 2.5 m for the sand layer with 98% degree of saturation, while the thickness of liquefied layer at a $S_r =$ 95%, 90% and 85% are about 2 m, 1m, and 0.9m, respectively.

In order to show the effect of relative density on the dynamic responses, the predicted results for the unsaturated sand layer at a relative density $D_r = 60\%$ with different degrees of saturation are also presented. The time histories of predicted horizontal acceleration in selected elements E12, E16, and E20 along the soil profile at degrees of saturation of 98% and 85% are shown in Fig. 6.24. The amplification is also observed at different depths. It is to be noticed that in E20 with 98% degree of saturation, the amplification is observed in the first four seconds of the shaking. A

reduction to the acceleration in E20 is observed after 4.7 seconds, while the reduction is observed after two seconds for the sandy deposit with 98% degree of saturation and 40% relative density (Fig. 6.13). Compared with the results at 40% relative density, it can be concluded that the liquefaction resistance increases with an increase in relative density.

The time histories of pore water pressure and pore air pressure in E16 with 98% and 85% degree of saturation at 40% and 60% relative density are compared in Fig. 6.25. It can be seen that slightly larger pore water pressure and pore air pressure in E16 are generated for 98% degree of saturation during the shaking. The differences in the pore water and air pressures between these two relative densities are negligible for 85% degree of saturation. Fig. 6.26 compares the time histories of normalized vertical VIS in E19 at degrees of saturation of 98%, 95%, 90%, 85%, and 60%. It can be seen that liquefaction is not observed at degree of saturation of 85%, while liquefaction occurs at 85% degree of saturation and 40% relative density (Fig. 6.22). For an unsaturated element at a given elevation, the normalized VIS increases as the degree of saturation decreases at a given time of the shaking. It indicates that the lower the degree of saturation, the higher liquefaction resistance. The time histories of normalized vertical intergranular stress in different elements at 98% and 85% degree of saturation for the 40% and 60% relative density are compared in Fig. 6.27. For the sand layer with a higher degree of saturation (98%), the effect of relative density on the normalized vertical intergranular stress is insignificant. The normalized vertical intergranular stress of the sand layer in case of lower degree of saturation (85%) for 40% relative density is smaller than that for 60% relative density. This indicates that the liquefaction resistance of unsaturated sand layer increases with the increase in the relative density. The

minimum normalized vertical intergranular stress in the soil column at different degrees of saturation during the shaking is compared in Fig. 6.28. The trend that the thickness of liquefied layer decreases as degree of saturation decreases is also observed. For example, the thickness of liquefied layer is about 2.5 m for the sand layer with 98% degree of saturation. The thickness of liquefied layer at a $S_r = 95\%$ is about 1.5 m, which is smaller than 2 m thick liquefied layer at $S_r = 95\%$ and $D_r = 40\%$.

The simulation results on seismic response of unsaturated sands level ground using the aforementioned finite element procedure show that the liquefaction resistance of unsaturated sands layer is influenced by degree of saturation and relative density, which are consistent with those predicted using CM4USS in a single element level. Valuable insights such as depths of liquefaction are, however, gained through the analyses of the boundary value problems.

6.4 Summary

CM4USS is implemented in the fully coupled equations governing the dynamic behavior of unsaturated soils developed in Chapter 4 using the closest point projection method by modifying the integration process in the literature (Liu and Muraleetharan 2012b). Some numerical examples, such as 1D drying and wetting of a soil column, unsaturated elastoplastic soil under uniform loading, and seismic response of level ground unsaturated sand deposits, are performed to validate the performance and capability of the implementation. The effects of the degree of saturation and relative density on the dynamic behavior of unsaturated sands are investigated. The results

demonstrate that the proposed model is capable of predicting the dynamic behavior of unsaturated soils in a boundary/initial value problem.

Table 6.1 Integration procedure of numerical implementation of CM4USS

Known: I_n, $\mathbf{s}_n$, $s_{c,n}$, $\boldsymbol{\varepsilon}_n$, $\Delta\boldsymbol{\varepsilon}$, Δs_c for the current time step t_n

Search: I_{n+1}, $\mathbf{s}_{n+1}$, $n_{w,n+1}$ for time step t_{n+1}

Step 1: Calculate trial stress I_{n+1}^{trial} and s_{n+1}^{trial} assuming purely elastic strain increments

Calculate $s_{c,\,n+1}$ and $n_{\mathrm{w},\,n+1}^{trial}$

Step 2: Check the suction path and yield condition

$f\left(I_{n+1}^{trial}, \mathbf{s}_{n+1}^{trial}, s_{c,n+1}; \boldsymbol{\alpha}_{n+1}^{trial}, m_{n+1}^{trial}\right) < 0$? and $\Delta s_{c,n+1} = 0$?

If YES, then $I_{n+1} = I_{n+1}^{(0)}$, $\mathbf{s}_{n+1} = \mathbf{s}_{n+1}^{(0)}$, $s_{c,\,n+1} = s_{c,\,n+1}^{(0)}$, $n_{\mathrm{w},\,n+1} = n_{\mathrm{w},\,n}$

Exit

Step 3: If $f\left(I_{n+1}^{trial}, \mathbf{s}_{n+1}^{trial}, s_{c,n+1}; \boldsymbol{\alpha}_{n+1}^{trial}, m_{n+1}^{trial}\right) > 0$ and $\Delta s_{c,n+1} = 0$

Solve $\Delta\mathbf{U}_{n+1}^{1(m)} = -\left(\mathbf{T}^1\right)^{-1} \bar{\mathbf{R}}_{n+1}^{1(m)}$.

Step 4: If $f\left(I_{n+1}^{(0)}, \mathbf{s}_{n+1}^{(0)}, s_{c,n+1}^{(0)}; \boldsymbol{\alpha}_{n+1}^{(0)}, m_{n+1}^{(0)}\right) < 0$ and $\Delta s_{c,n+1} \neq 0$

Solve $\Delta\mathbf{U}_{n+1}^{2(m)} = -\left(\mathbf{T}^2\right)^{-1} \bar{\mathbf{R}}_{n+1}^{2(m)}$.

Step 5: If $f\left(I_{n+1}^{trial}, \mathbf{s}_{n+1}^{trial}, s_{c,n+1}; \boldsymbol{\alpha}_{n+1}^{trial}, m_{n+1}^{trial}\right) > 0$ and $\Delta s_{c,n+1} \neq 0$

Solve $\Delta\mathbf{U}_{n+1}^{3(m)} = -\left(\mathbf{T}^3\right)^{-1} \bar{\mathbf{R}}_{n+1}^{3(m)}$.

Step 6: Update I_{n+1}, $\mathbf{s}_{n+1}$, $n_{w,n+1}$ and internal variables, set $n = n+1$

Table 6.2 Material properties for unsaturated elastoplastic Nevada sand

Properties	Symbol	Value	Unit
Density of solid skeleton	ρ_s	2670	kg/m^3
Density of water	ρ_w	1000	kg/m^3
Density of air	ρ_a	1.22	kg/m^3
Bulk modulus of air	K_a	1×10^{2}	kPa
Bulk modulus of water	K_w	2.2×10^{6}	kPa
Intrinsic permeability	k	6.73×10^{-12}	m^2
Viscosity of water	μ_w	1×10^{-6}	kPa·s
Viscosity of air	μ_a	1.8×10^{-8}	kPa·s
Empirical parameter	m	0.8	-

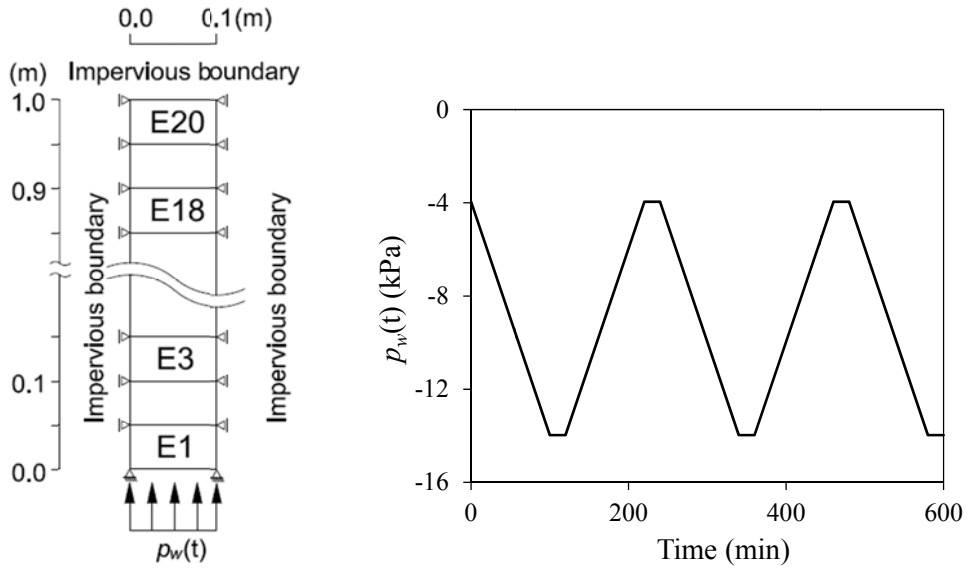

Fig. 6.1 1D drying and wetting of a soil column: problem geometry, finite element mesh and boundary conditions

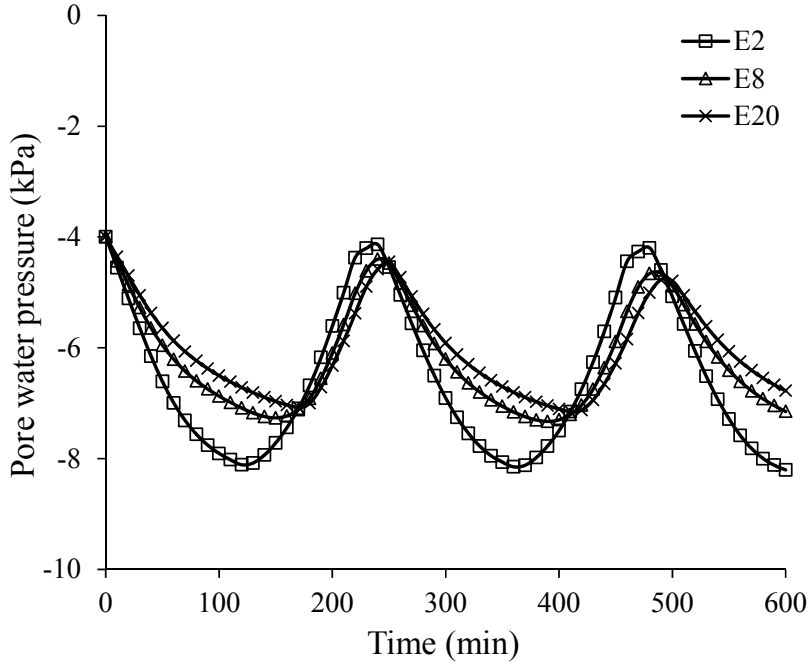

Fig. 6.2 1D drying and wetting of a soil column: predicted pore water pressure at different elevations

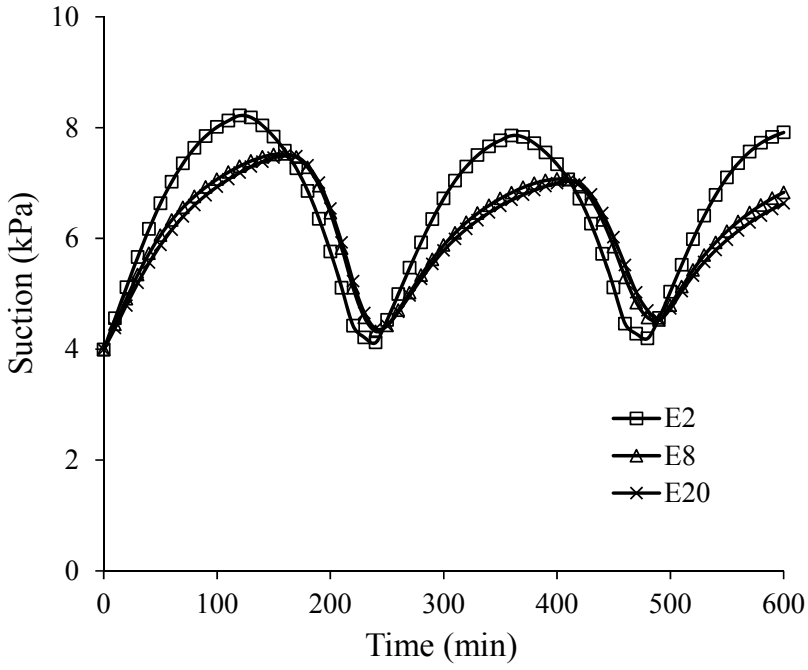

Fig. 6.3 1D drying and wetting of a soil column: predicted suction at different elevations

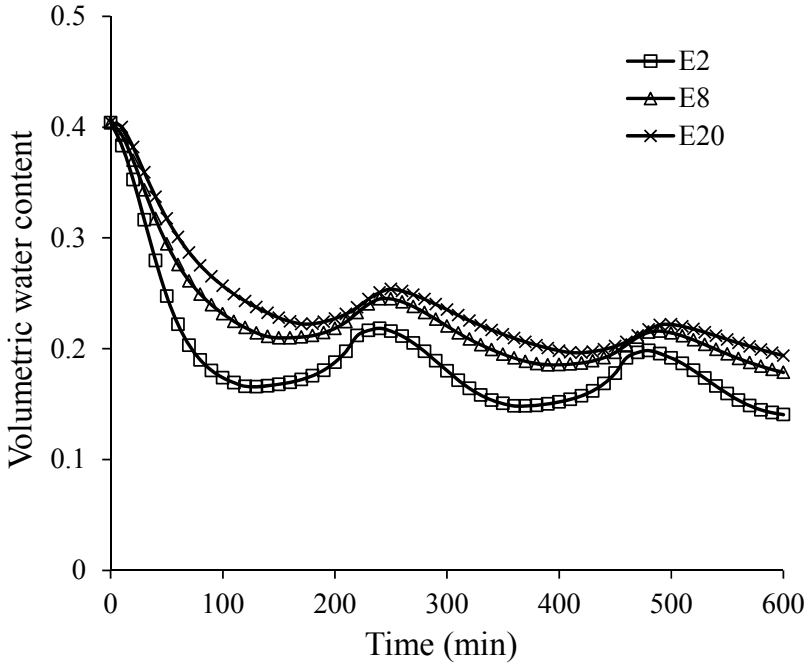

Fig. 6.4 1D drying and wetting of a soil column: predicted volumetric water content at different elevations

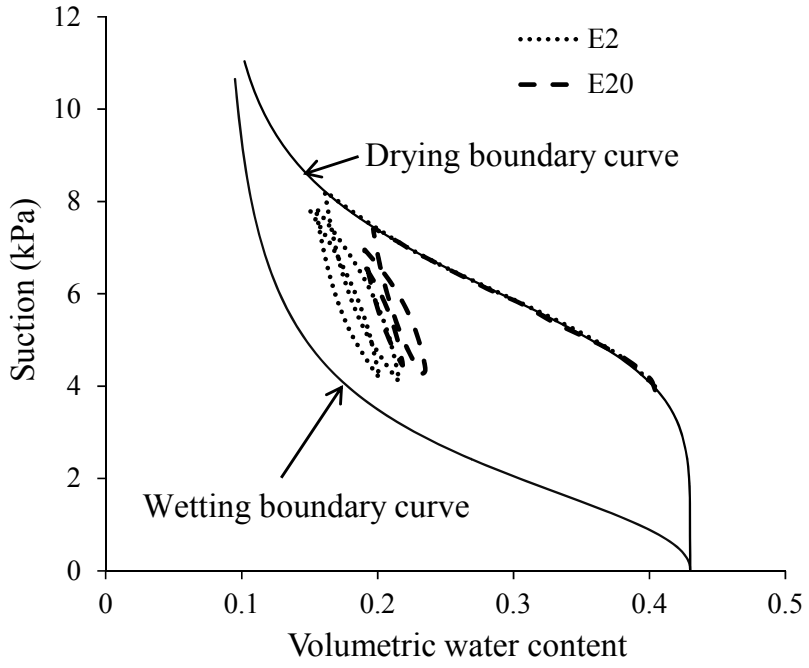

Fig. 6.5 1D drying and wetting of a soil column: predicted hydraulic path at different elevations

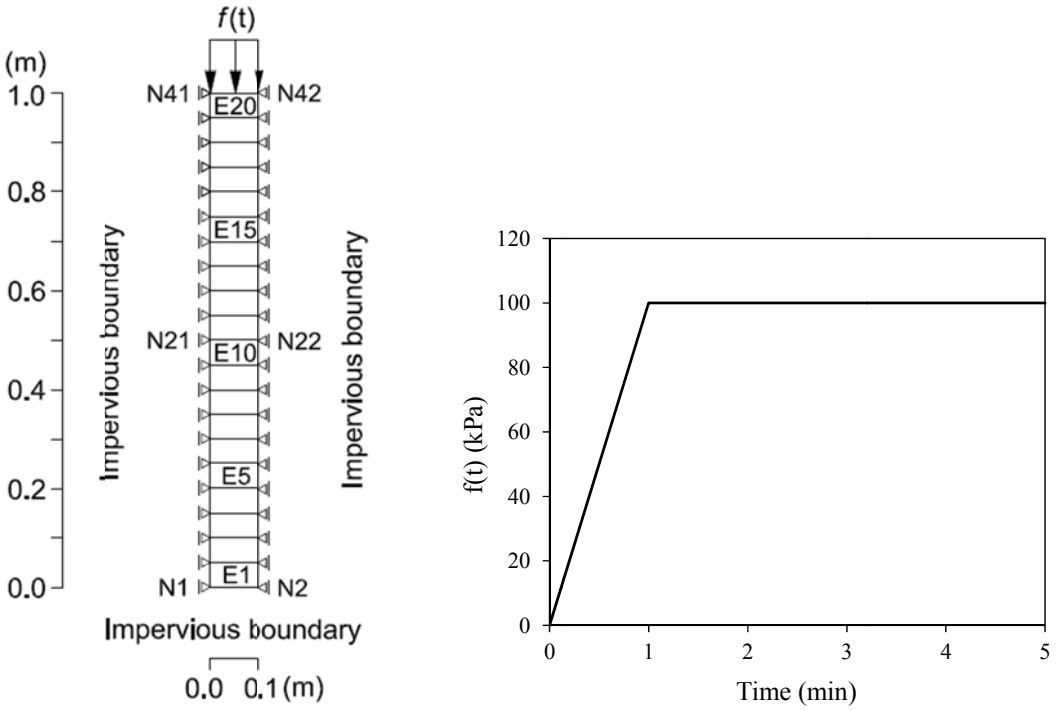

Fig. 6.6 Uniform loading for unsaturated elastoplastic soil: problem geometry, finite element mesh and boundary conditions

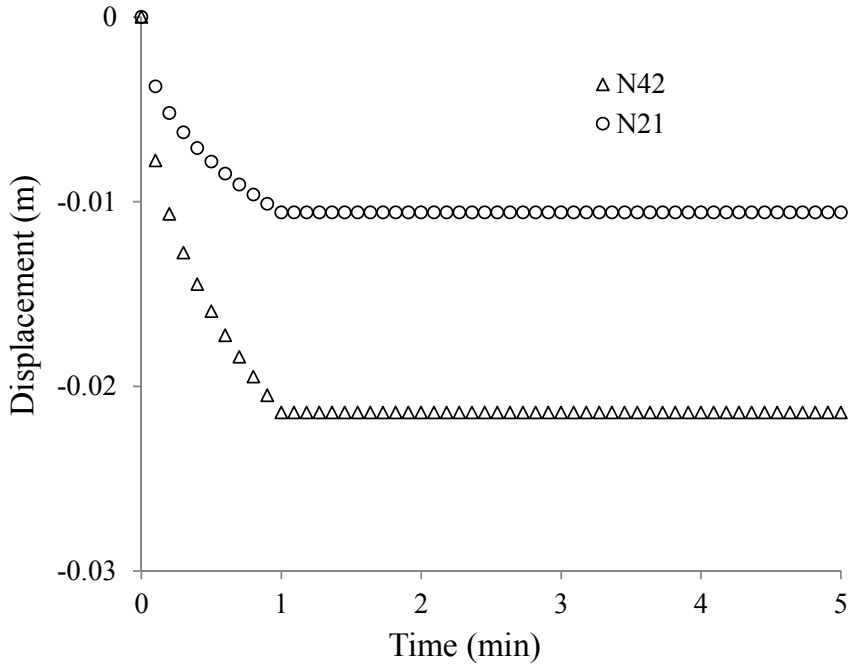

Fig. 6.7 Unsaturated elastoplastic soil under uniform loading: predicted vertical displacements

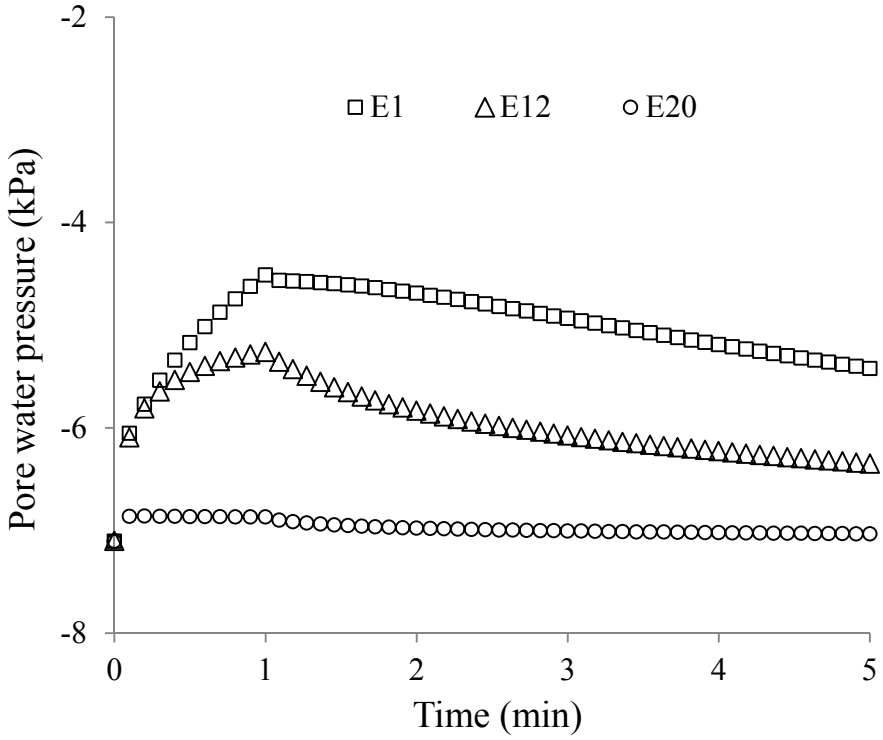

Fig. 6.8 Unsaturated elastoplastic soil under uniform loading: predicted pore water pressure

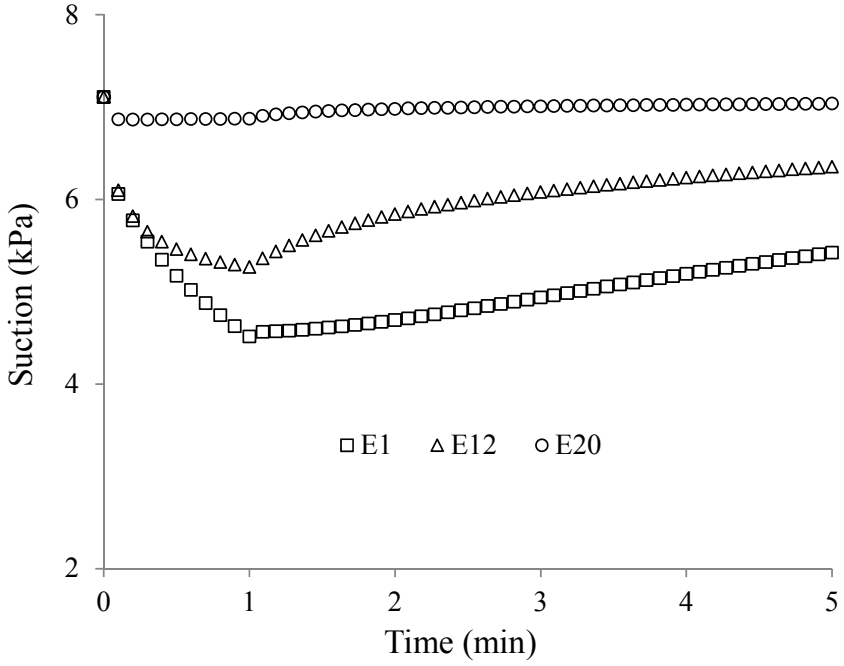

Fig. 6.9 Unsaturated elastoplastic soil under uniform loading: predicted suction

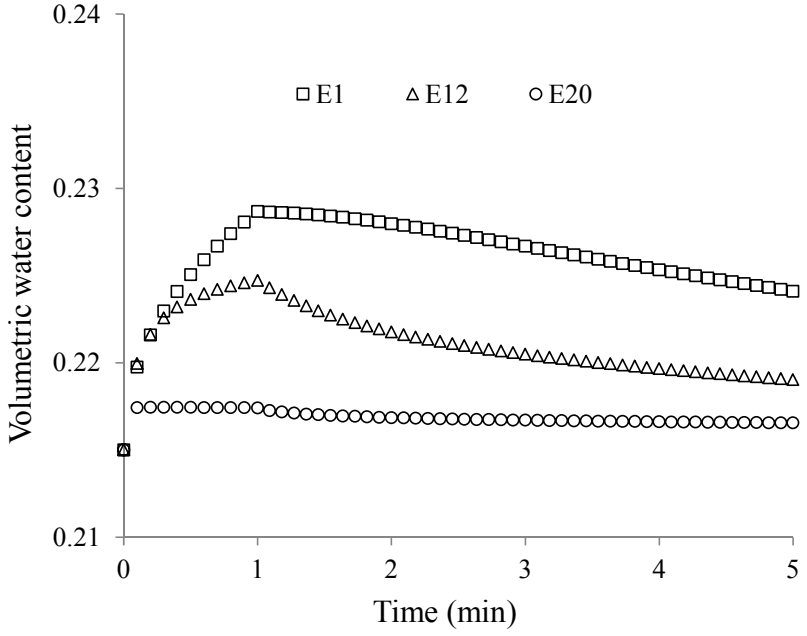

Fig. 6.10 Unsaturated elastoplastic soil under uniform loading: predicted volumetric water content

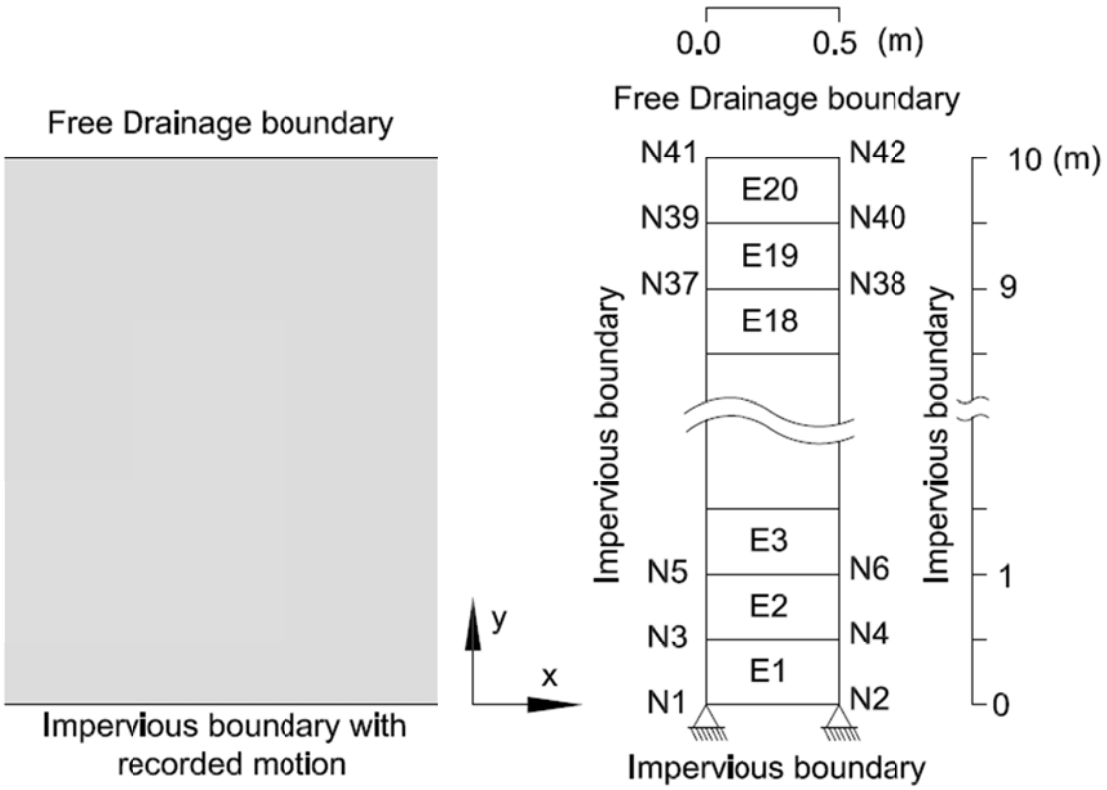

Fig. 6.11 Dynamic response of level ground deposits of an unsaturated sand: problem geometry, finite element mesh and boundary conditions

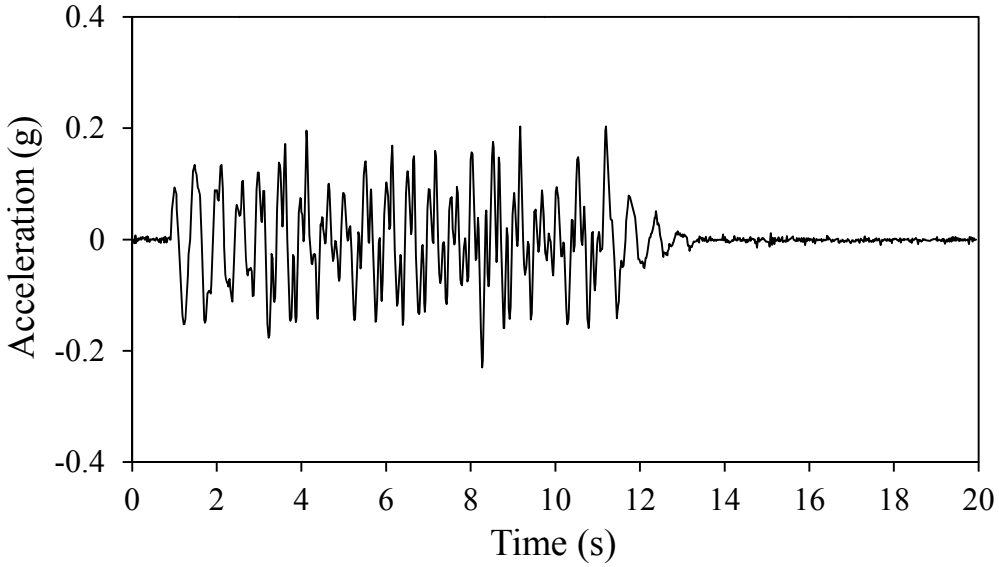

Fig. 6.12 Horizontal input acceleration for the soil column

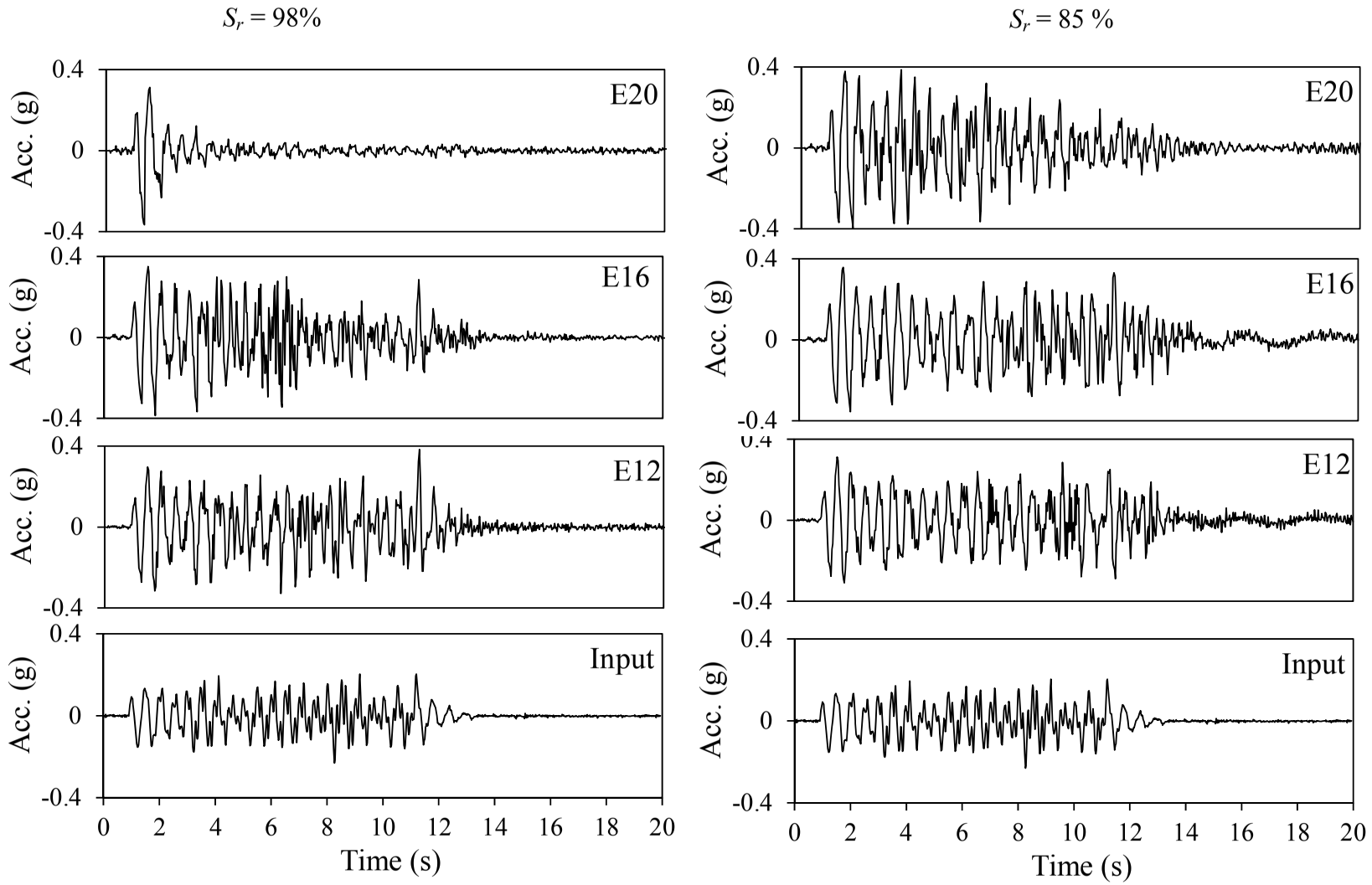

Fig. 6.13 Time histories of accelerations in selected elements at different degrees of saturation for the 40% relative density

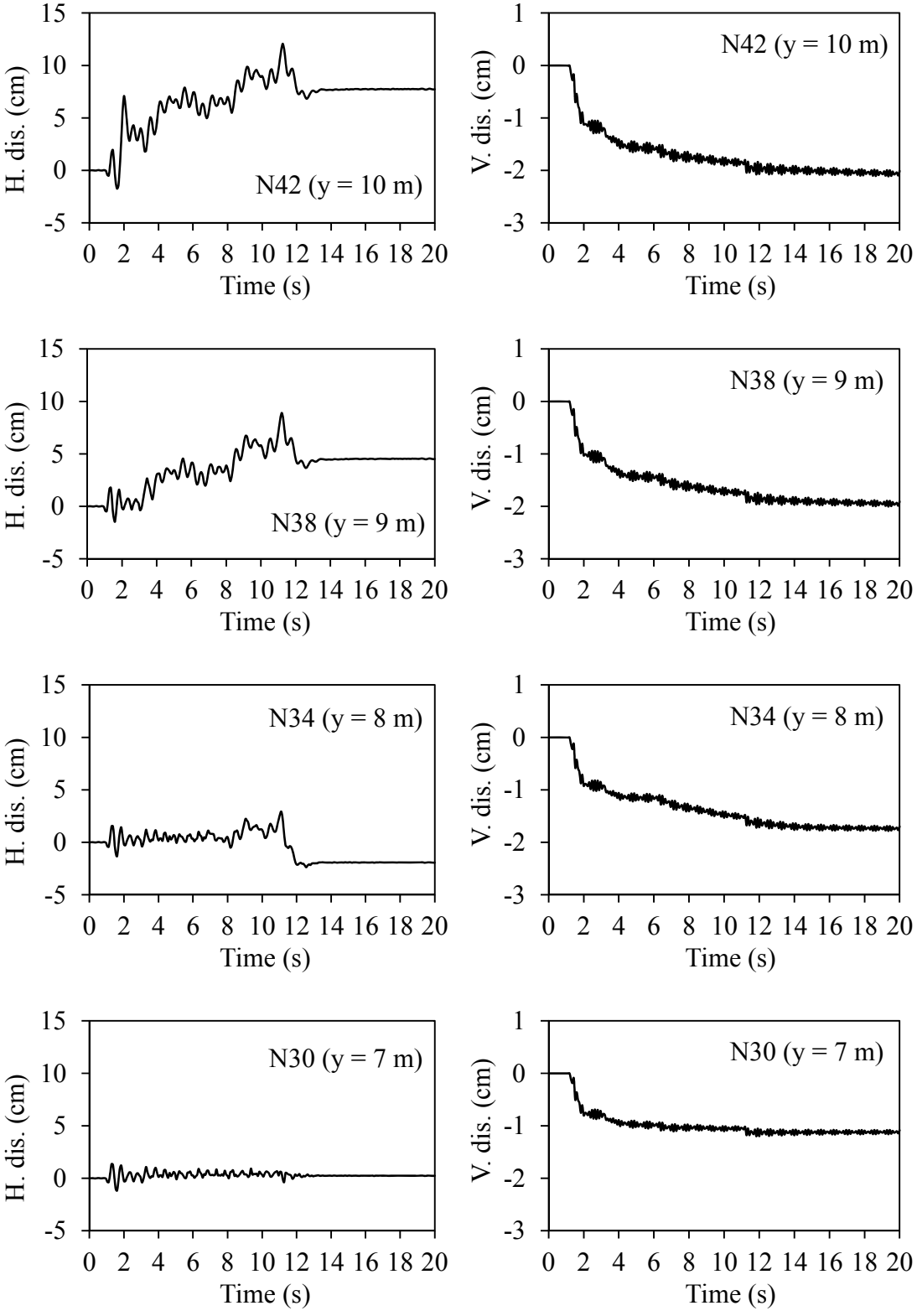

Fig. 6.14 Time histories of horizontal displacements and vertical displacement in selected nodes along soil profiles for the 98% degree of saturation and 40% relative density

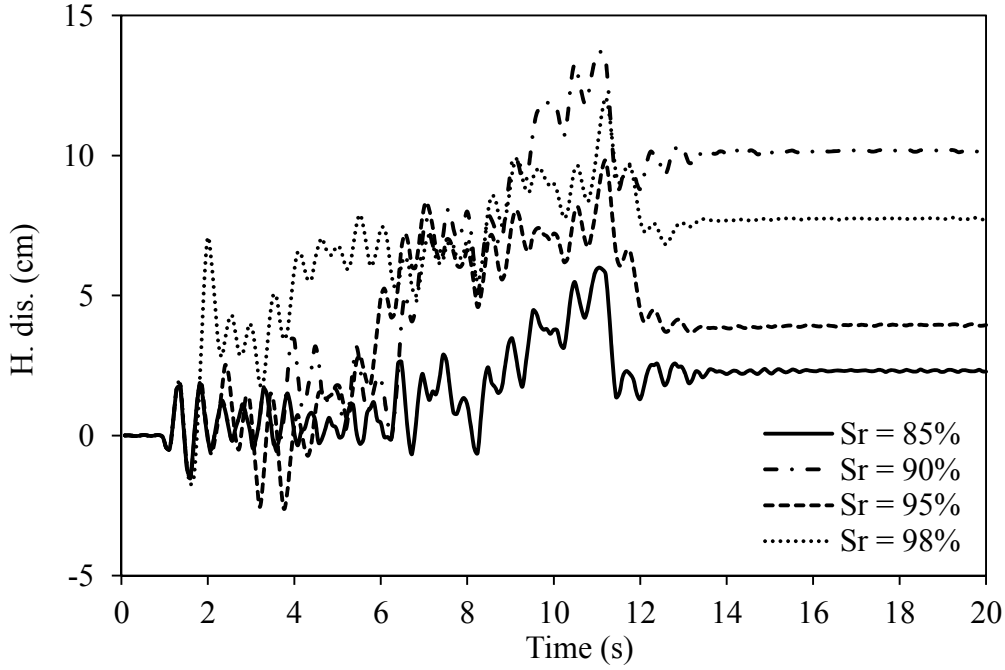

Fig. 6.15 Time histories of horizontal displacements at the top surface at different degrees of saturation for the 40% relative density

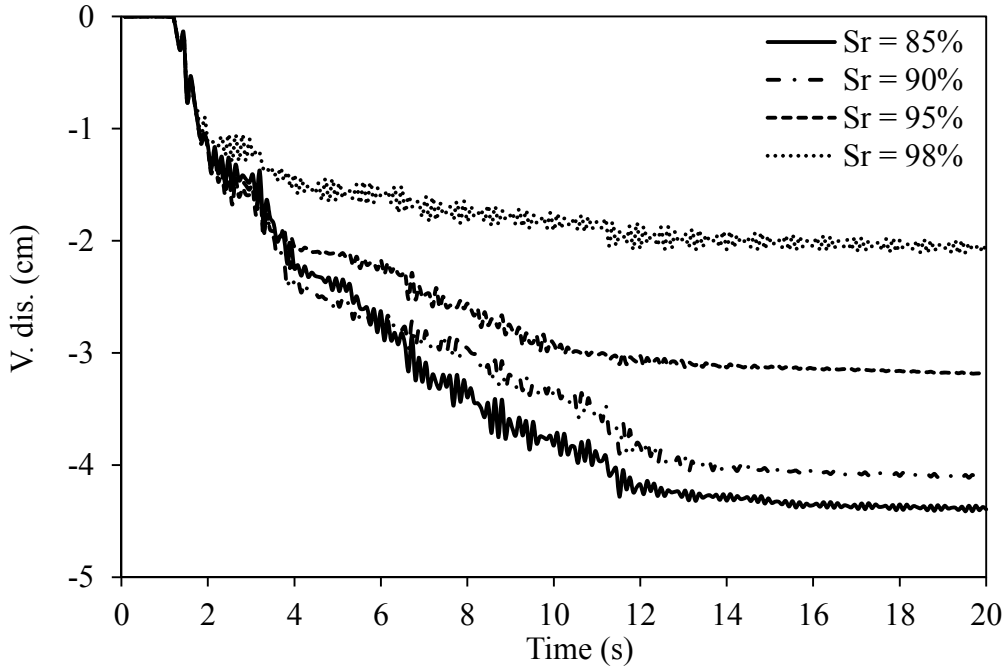

Fig. 6.16 Time histories of vertical displacements at the top surface at different degrees of saturation for the 40% relative density

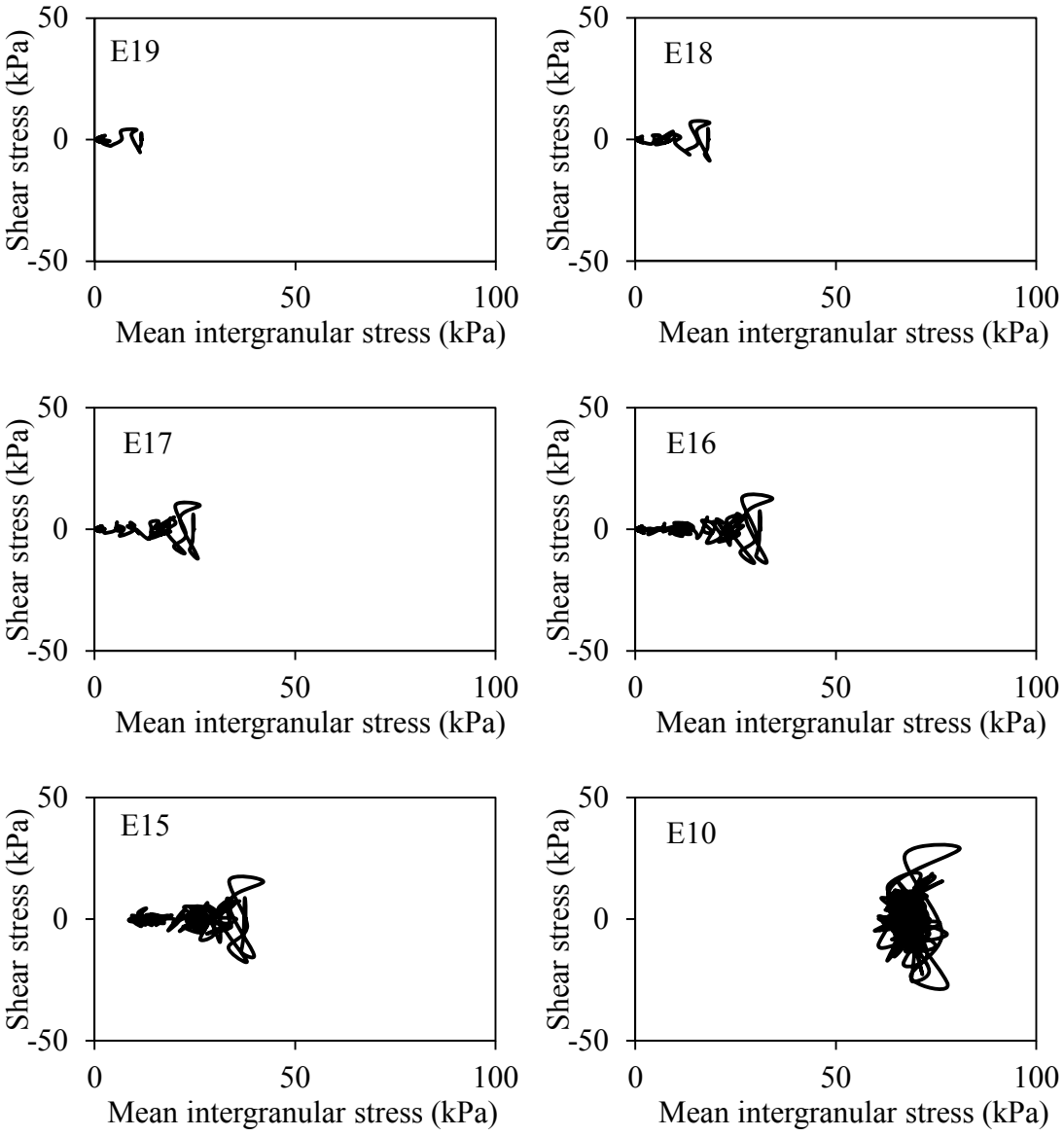

Fig. 6.17 Variations of mean intergranular stress versus shear stress in selected elements for the 98% degree of saturation and 40% relative density

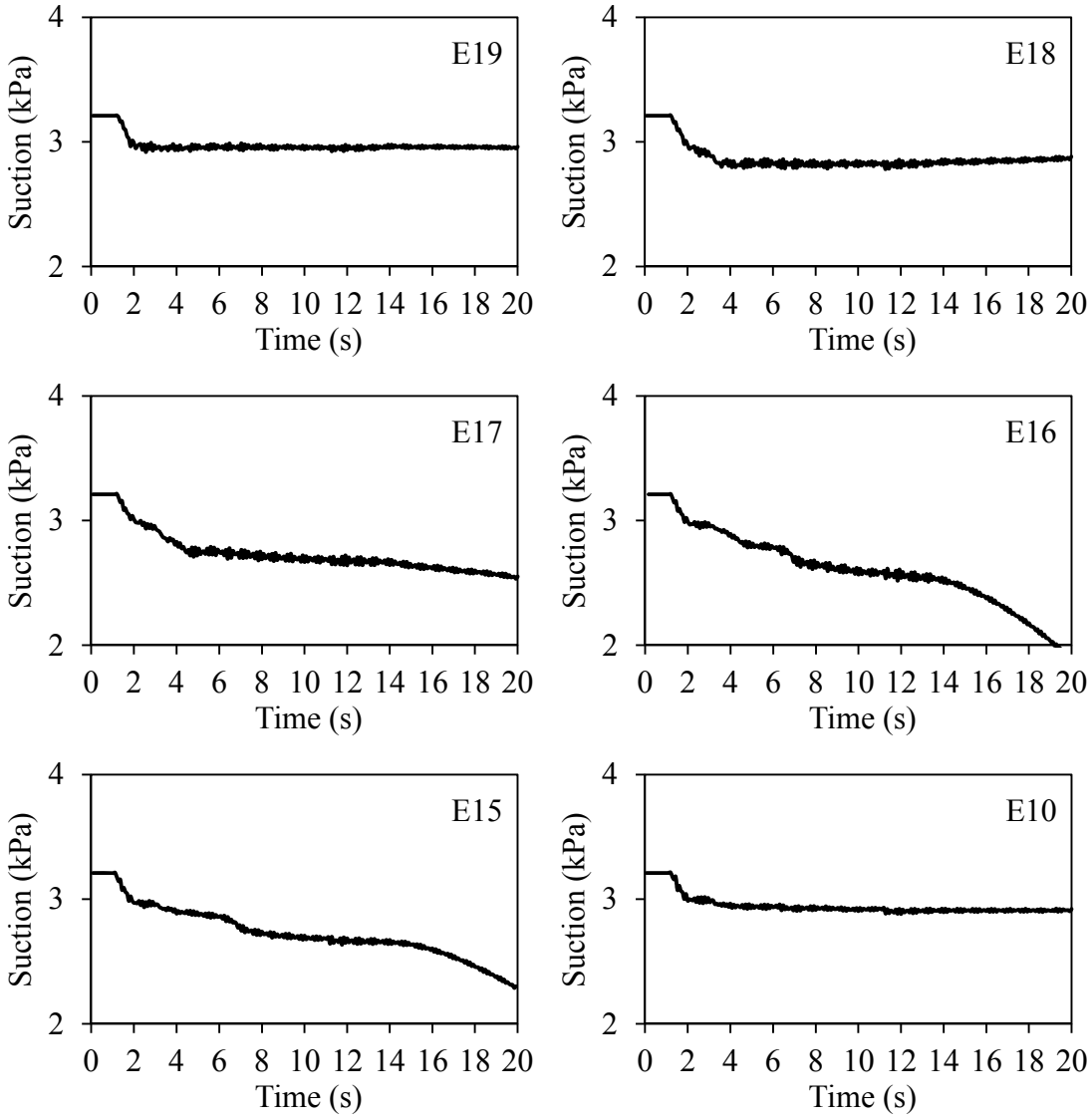

Fig. 6.18 Time histories of suction in selected elements along soil profiles for the 98% degree of saturation for the 40% relative density

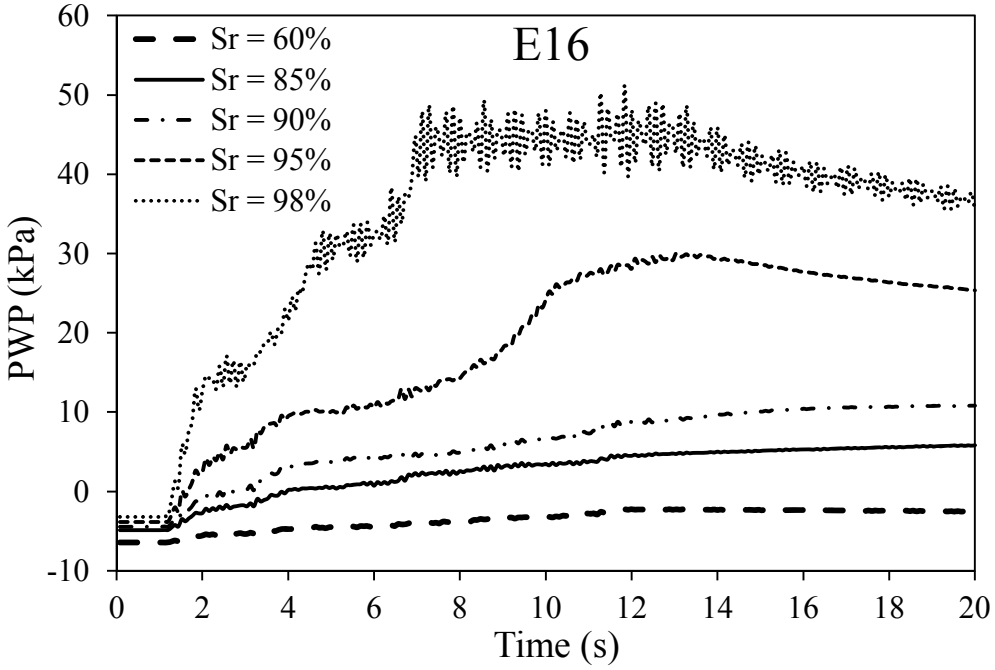

Fig. 6.19 Time histories of pore water pressure at E16 at different degrees of saturation for the 40% relative density

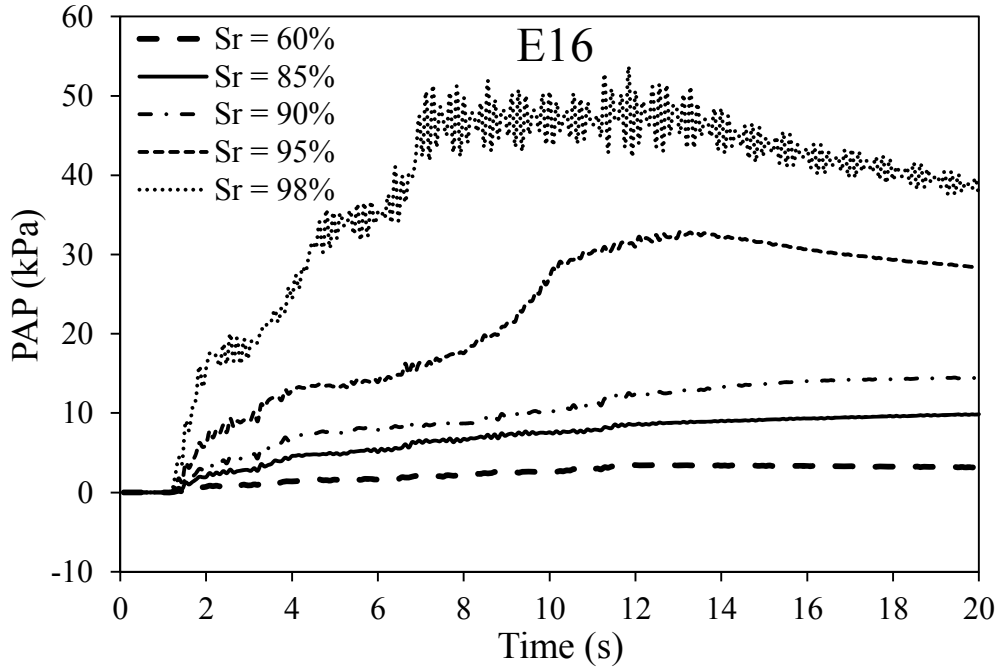

Fig. 6.20 Time histories of pore air pressure at E16 at different degrees of saturation for the 40% relative density

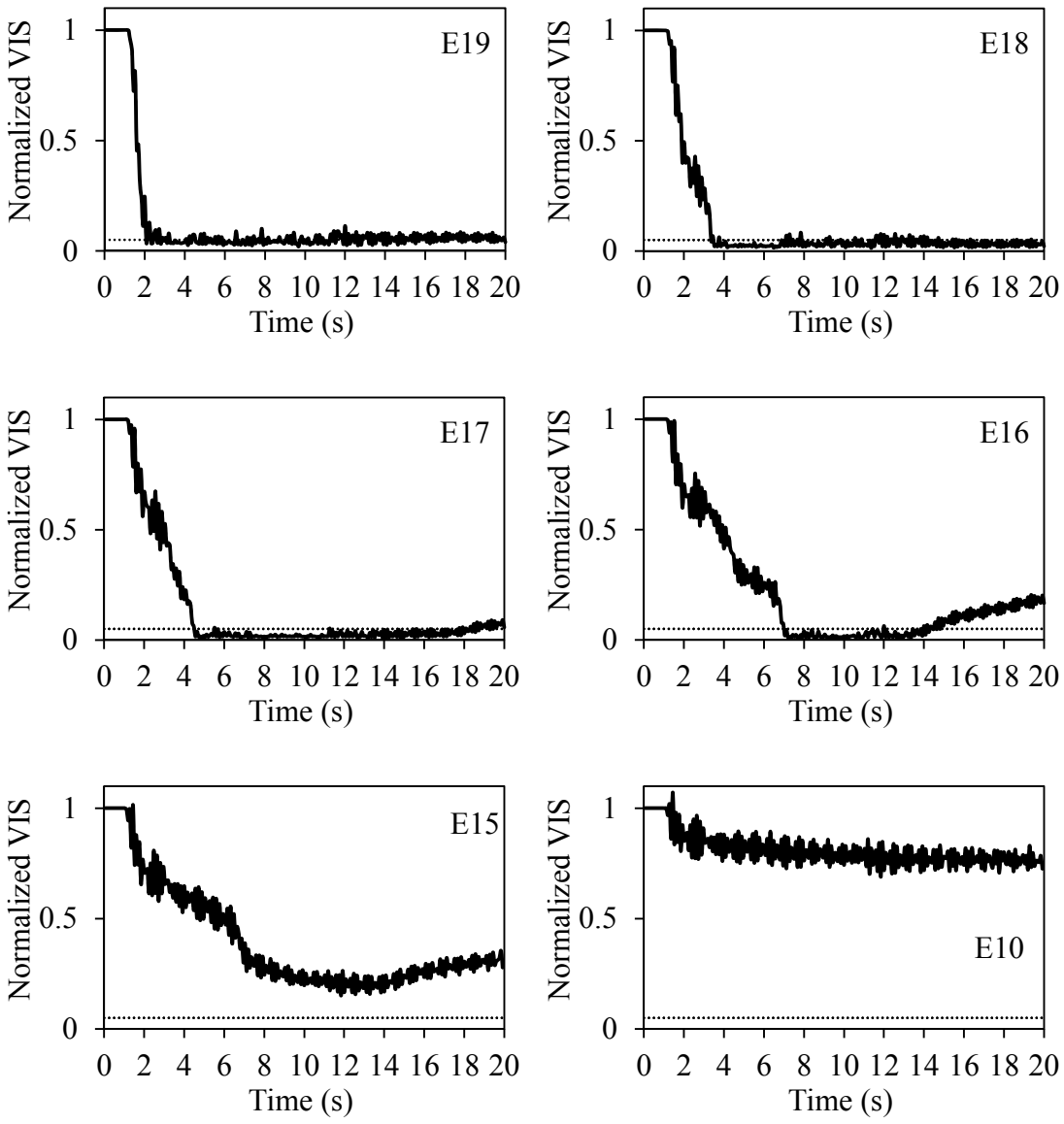

Fig. 6.21 Time histories of normalized vertical intergranular stress in selected elements along soil profiles for the 98% degree of saturation and 40% relative density

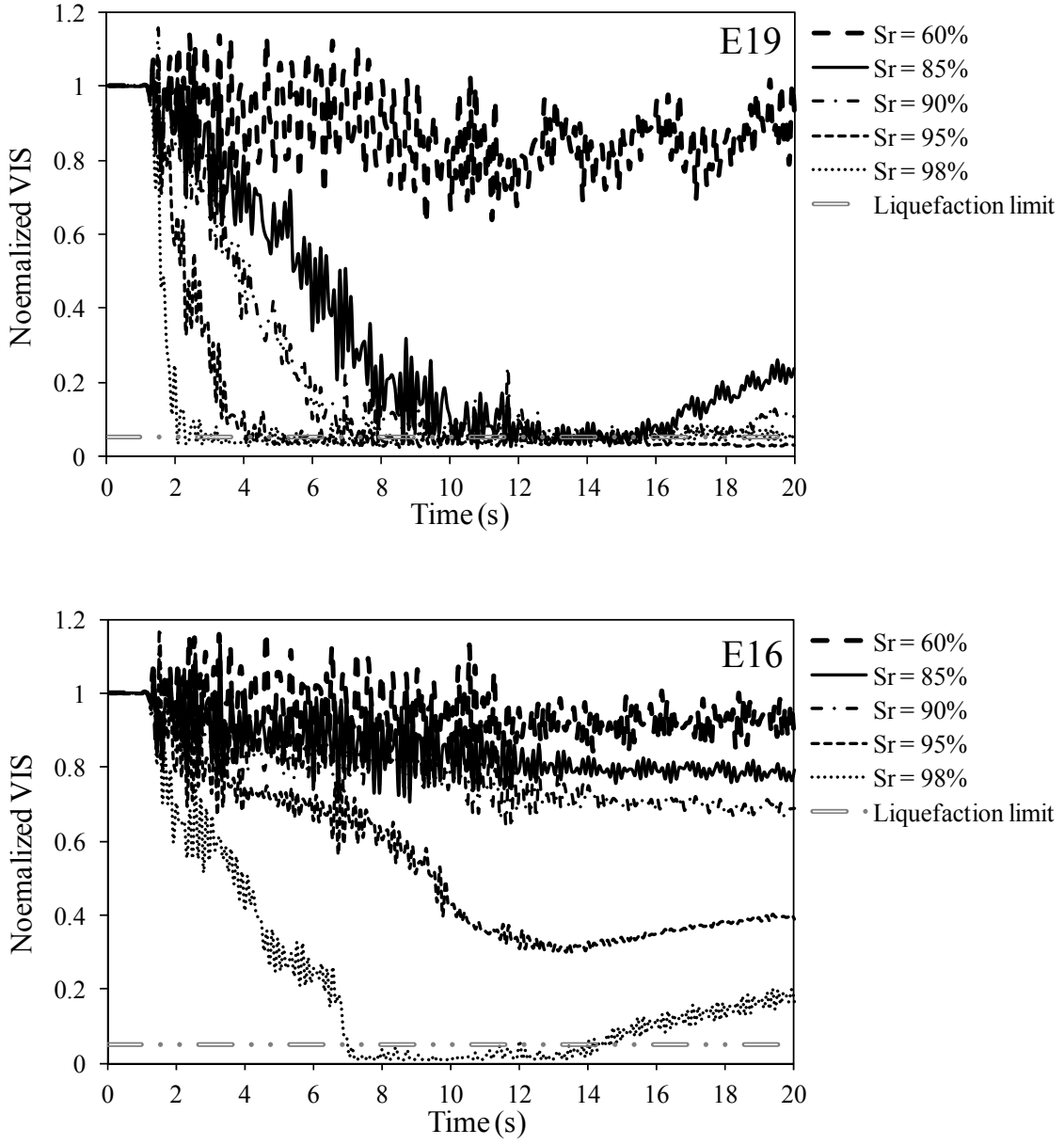

Fig. 6.22 Time histories of normalized vertical intergranular stress at E19 and E16 at different degrees of saturation for the 40% relative density

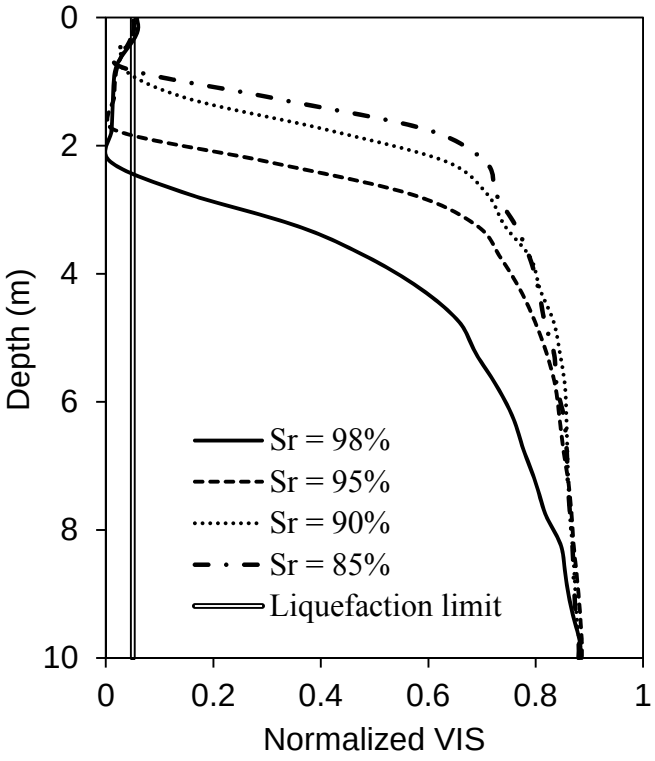

Fig. 6.23 Minimum normalized vertical intergranular stress in the soil column at different degrees of saturation for the 40% relative density during the shaking

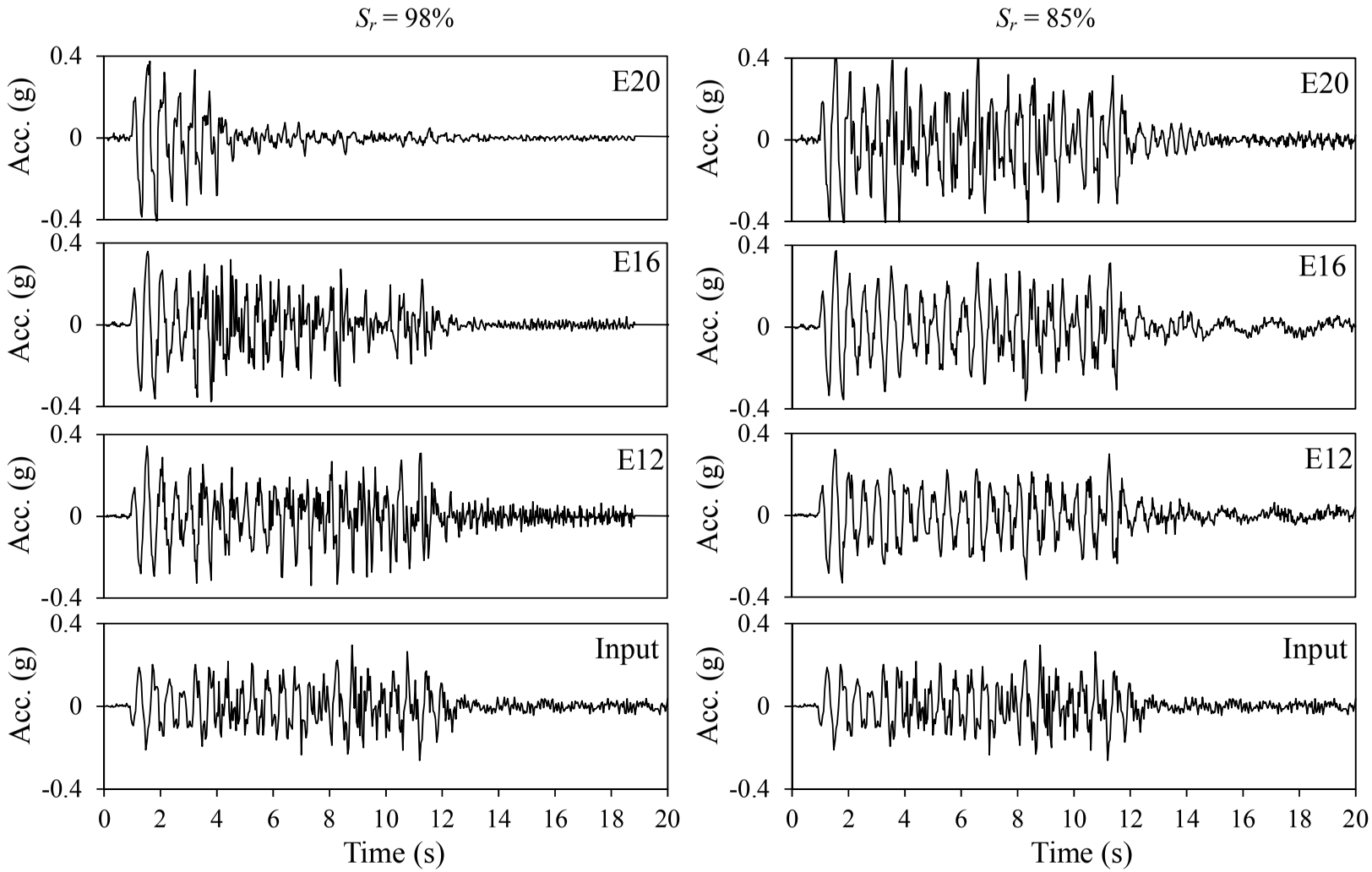

Fig. 6.24 Time histories of accelerations in selected elements at different degrees of saturation for the 60% relative density

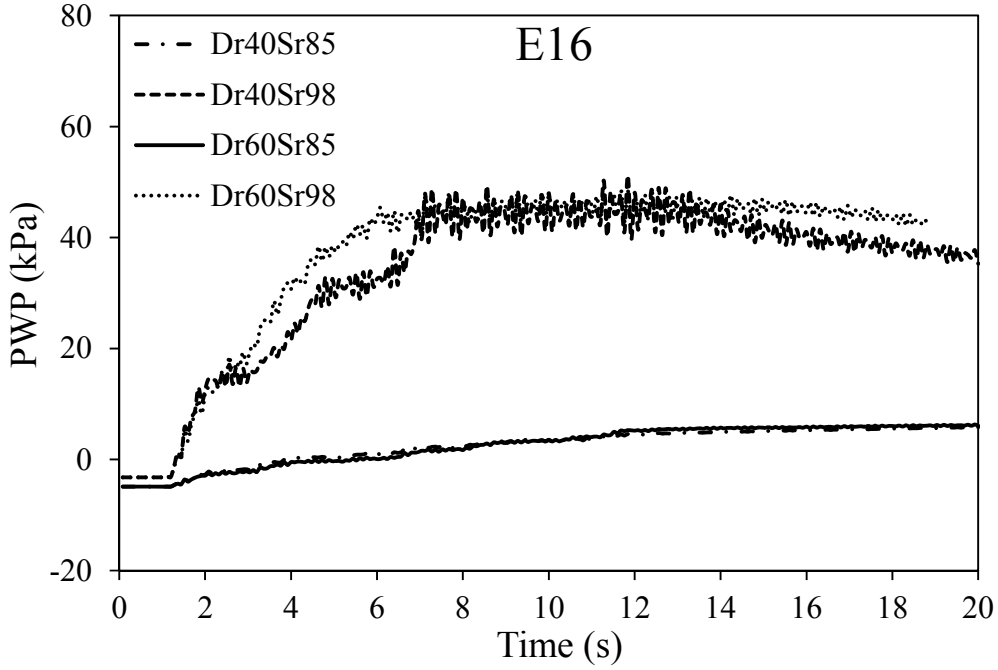

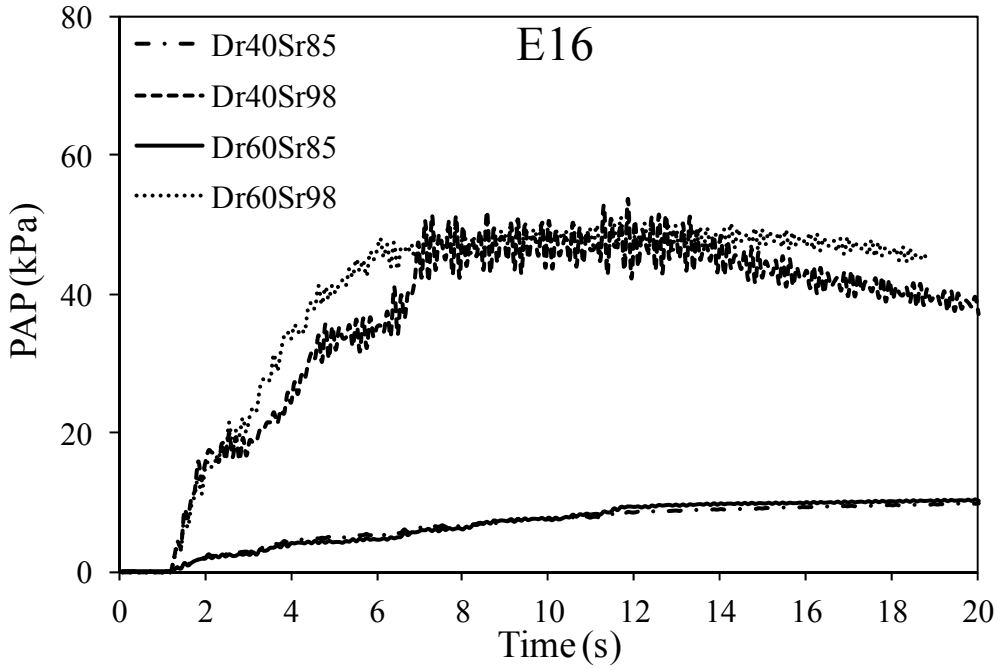

Fig. 6.25 Time histories of pore water pressure and pore air pressure in E16 at 98% and 95% degree of saturation for the 40% and 60% relative density

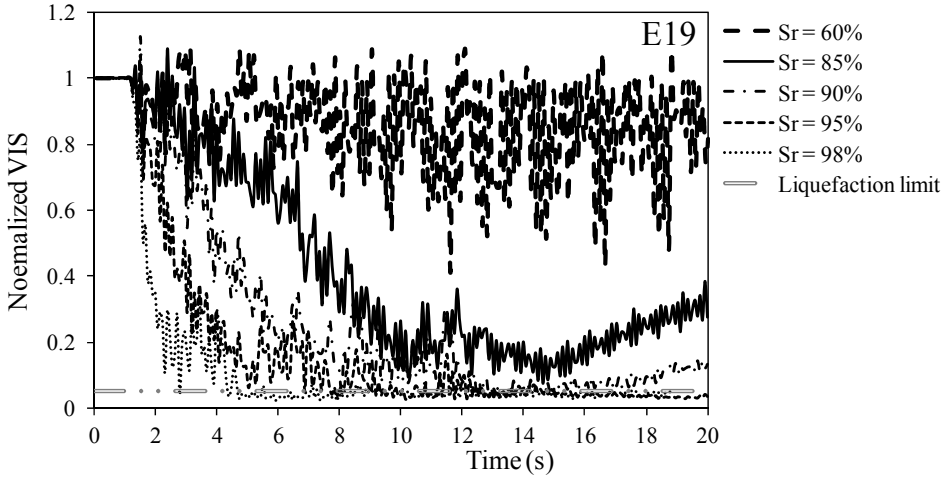

Fig. 6.26 Time histories of normalized vertical intergranular stress at E19 at different degrees of saturation for the 60% relative density

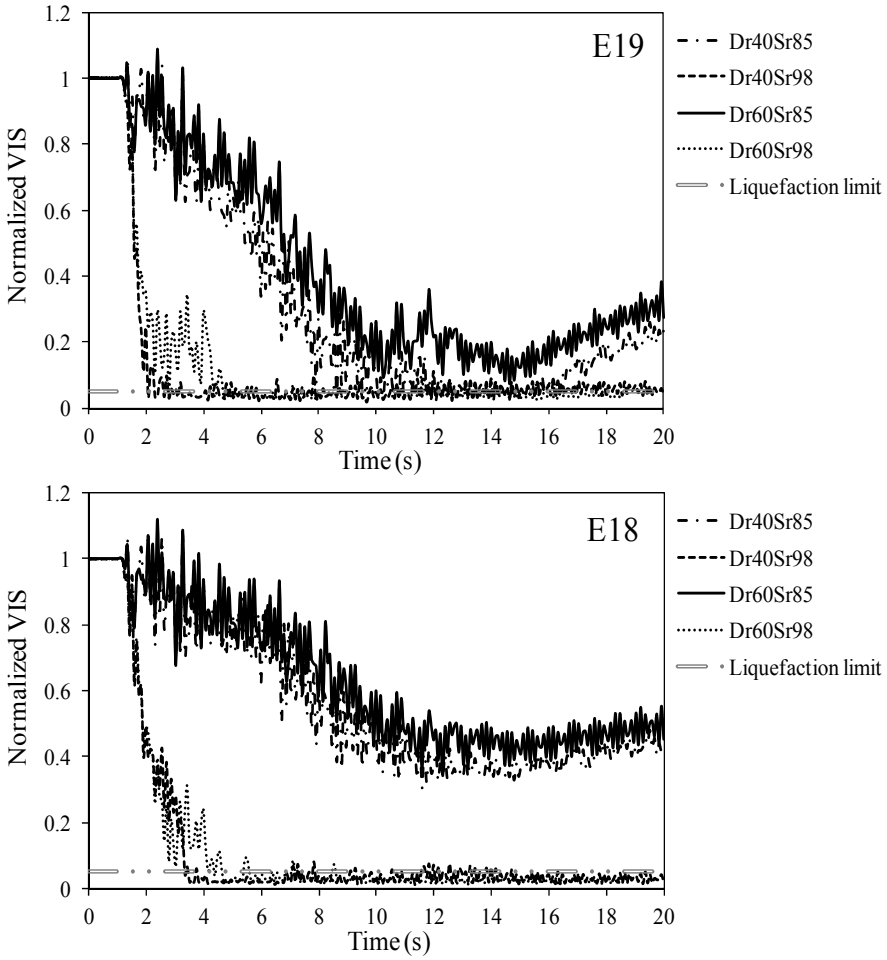

Fig. 6.27 Time histories of normalized vertical intergranular stress in different elements at 98% and 85% degree of saturation for the 40% and 60% relative density

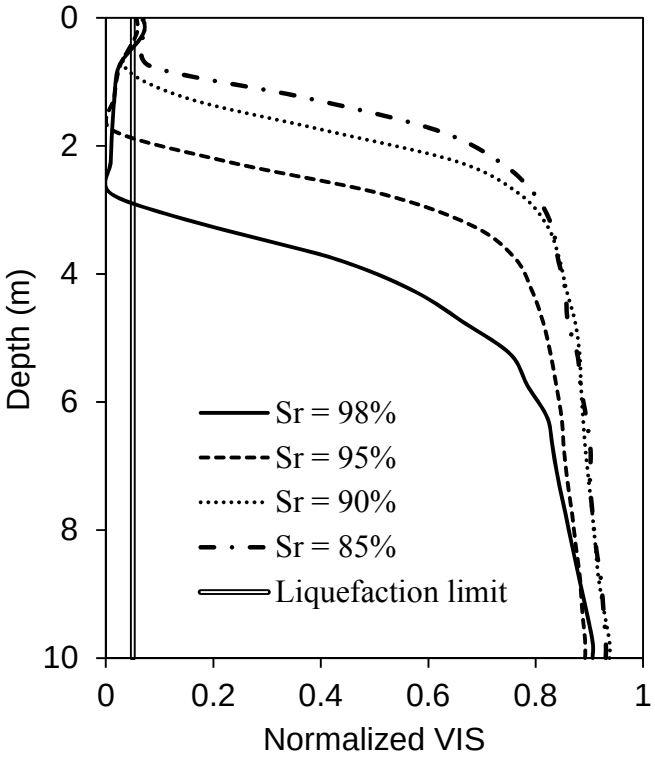

Fig. 6.28 Minimum normalized vertical intergranular stress in the soil column at different degrees of saturation for the 60% relative density during the shaking

CHAPTER 7 SUMMARY, CONCLUSIONS AND RECOMMENDATIONS

7.1 Summary

It has always been of great importance for geotechnical engineers to understand seismic behavior of unsaturated embankments, dams and levees. Although experimental tests provide a reliable method to study to dynamic behavior of different structures, they are costly and time consuming. In recent years, attention has been paid to the development of analytical procedures to provide insight into the dynamic behavior of geotechnical engineering structures. Prediction of fluid flows and deformations during earthquake loading is not only important aspects in the design of new geotechnical soil structures, but also in the seismic evaluation of the existing structures.

The main objective of this study was to implement CM4USS into a finite element code for fully coupled analysis of the hydraulic and mechanical behavior in unsaturated soils subjected to dynamic loading. The main tasks accomplished in this research were: (1) investigation of the effect of initial conditions (degree of saturation, relative density, and confining pressure) on the liquefaction of unsaturated sands and development of a design chart that can be used to evaluate the liquefaction potential of unsaturated sands; (2) study on the effect of the hydraulic hysteresis on the dynamic

response of unsaturated soils using a fully coupled finite element computer code with a hysteretic SWCCs model; and (3) implementation of CM4CSS into a fully coupled finite element computer code using an implicit integration algorithm and validation of the implementation using numerical examples on unsaturated soils subjected to dynamic loading. The research conclusions are summarized in this chapter and recommendations for further research are provided.

7.2 Conclusions

The following conclusions can be drawn from the results in this study:

(1). The simulation using CM4USS on undrained stress-controlled cyclic triaxial tests confirm that liquefaction indeed occurs in unsaturated sands.

(2). CM4USS was used to predict the number of cycles to cause liquefaction through simulations of a series of undrained cyclic tests on unsaturated Toyoura sand and reasonable comparisons were obtained with measured results.

(3). The liquefaction resistance of unsaturated sands is influenced by degree of saturation, relative density, and initial effective stress. The liquefaction resistance increases with a decrease in the initial degree of saturation and increases in relative density and initial effective confining pressure. When the degree of saturation is near 100%, the effect of the degree of saturation on the liquefaction resistance is more significant.

(4). A liquefaction potential design chart for sands that separates liquefaction from no-liquefaction is developed based on the simulation results. The degree of saturation, relative density and initial effective confining pressure were incorporated into this design chart.

(5). The vertical displacements of the unsaturated embankment predicted by considering the hydraulic hysteresis were larger than those predicted by the analysis without hysteresis, but there was no significant difference in horizontal displacements between these two analyses. Both the hysteresis and non-hysteresis analyses predicted the increases in pore water and pore air pressures during shaking. The predicted suction reduction was, however, larger for the analysis with hysteresis.

(6). The implementation of CM4USS into U_DYSAC2 is validated by simulating several boundary value problems.

(7). The simulation results on a level ground site of unsaturated Nevada sand deposit subjected to base shaking showed that the liquefaction of an unsaturated sand deposit was influenced by degree of saturation and relative density, which were consistent with those predicted using CM4USS in a single element level.

(8). The amplification of acceleration magnitude was observed at different depths and the extent of amplifications increased slightly towards the ground surface.

(9). The thickness of liquefied zone in unsaturted soils was influenced by the degree of saturation. The thickness of liquefied layer decreased as degree of saturation decreased.

7.3 Recommendations

The following potential research areas are worthy of future research:

(1). The liquefaction potential design chart was developed based on the simulated results of Toyoura sand and Nevada sand. More studies for other sands and non-plastic silts are needed to improve the design chart developed in this research.

(2). Although the liquefaction of unsaturated sands has important practical applications, it has not attracted considerable attention in the geotechnical engineering community. More experimental and theoretical research on liquefaction in unsaturated sands and silts are needed. A series of dynamic centrifuge tests on a variety of different unsaturated sands under different conditions is useful to study the complex coupling between solid skeleton, pore water, and pore air phases.

(3). Development of a unified fully coupled unsaturated soil model for sands, silts and clays. Many existing constitutive models for unsaturated soils were developed using distinctively different yield surfaces and plastic potentials for sands and clays. The motivation for unified formulations for sands and clays rises from a practical point of view. In the numerical analysis of the initial and boundary value problems, only different material constants and

model parameters need to be incorporated if the form of constitutive equations for several soil types remains the same. It would be particularly advantageous to treat cohesionless soils (silts and sands) and cohesive soil (clays) using a same framework.

(4). In the simulations of seismic response of a level ground deposit of unsaturated Nevada sand, an uniform distribution of degree of saturation in the soil profile is assumed as the initial condition. In geotechnical engineering practice, the degree of saturation profile is typically different along the depth of the sand deposit. The simulations of seismic response of a level ground deposit of unsaturated sand with different initial degree of saturation along the sand profile will definitely be helpful for the understanding of the dynamic behavior of unsaturated soil structures.

(5). Simulations of two and three dimensional boundary value problems and comparison with the experimental results like centrifuge tests are another recommended future research area.

REFERENCES

Aitchison, G. (1960). "Relationships of moisture stress and effective stress functions in unsaturated soils." *Proc.,5th International Conference on Soil Mechanics and Foundation Engineering*, 47-52.

Alonso, E. E., Gens, A., and Josa, A. (1990). "A constitutive model for partially saturated soils." *Géotechnique*, 40(3), 405-430.

Alonso, E. E., Lloret, A., Gens, A., and Yang, D. Q. (1995). "Experimental behaviour of highly expansive double-structure clay." *Proc.,1st Int. Conf. on Unsat. Soils*, Vol. 1, 11-16.

Ananthanathan, P. J. (2002). "Laboratory testing of unsaturated Minco silt." Master Thesis, University of Oklahoma, Norman, Oklahoma.

Arab, A., Shahrour, I., and Lancelot, L. (2011). "A laboratory study of liquefaction of partially saturated sand." *Journal of Iberian Geology*, 37(1), 29-36.

Arulmoli, K., Muraleetharan, K. K., Hossain, M. M., and Fruth, L. S. (1992). "VELACS: Verification of liquefaction analyses by centrifuge studies laboratory testing program: soil data report." Earth Technology Corporation, Irvine, California.

Asaoka, A., Noda, T., Yamada, E., Kaneda, K., and Nakano, M. (2002). "An elasto-plastic description of two distinct volume change mechanisms of soils." *Soils Found.*, 42(5), 47-57.

Bian, H., and Shahrour, I. (2009). "Numerical model for unsaturated sandy soils under cyclic loading: Application to liquefaction." *Soil Dyn. Earthquake Eng.*, 29(2), 237-244.

Bishop, A., and Donald, I. (1961). "The experimental study of partly saturated soil in the triaxial apparatus." *Proc.,5th Int. Conf. on Soil Mechanics and Foundation Engineering*, Vol. 1, 13-21.

Bishop, A. W. (1959). *The principles of effective stress*, Tek. Ukel. .

Bolzon, G., Schrefler, B. A., and Zienkiewicz, O. C. (1996). "Elastoplastic soil constitutive laws generalized to partially saturated states." *Géotechnique*, 46(2), 279-289.

Brooks, R. H., and Corey, A. T. (1964). "Hydraulicpropertiesofporous media." *Colorado State University, Hydro Paper*, 3, 27.

Buenfil, C., Romero, E., Lloret, A., and Gens, A. (2005). "Hydro-mechanical behaviour of a clayey silt under isotropic compression." *Unsaturated Soils: Experimental Studies*, Springer, 331-342.

Buscarnera, G., and Whittle, A. J. (2013). "Model prediction of static liquefaction: influence of the initial state on potential instabilities." *J. Geotech. Geoenviron. Eng.*, 139(3), 420-432.

Callari, C., and Abati, A. (2009). "Finite element methods for unsaturated porous solids and their application to dam engineering problems." *Computers & Structures*, 87(7-8), 485-501.

Chaney, R. C. (1978). "Saturation effects on the cyclic strength of sands." *Proc.,ASCE Special Conference on Earthquake Engineering and Soil Dynamics*, 342-358.

Chen, W., Xia, T., and Hu, W. (2011). "A mixture theory analysis for the surface-wave propagation in an unsaturated porous medium." *Int. J. Solids Struct.*, 48(16–17), 2402-2412.

Chillarige, A. V., Morgenstern, N. R., Robertson, P. K., and Christian, H. A. (1997). "Seabed instability due to flow liquefaction in the Fraser River delta." *Can. Geotech. J.*, 34(4), 520-533.

Chiu, C. F., and Ng, C. W. W. (2003). "A state-dependent elasto-plastic model for saturated and unsaturated soils." *Géotechnique*, 53(9), 809-829.

Cho, S. E., and Lee, S. R. (2001). "Instability of unsaturated soil slopes due to infiltration." *Comput. Geotech.*, 28(3), 185-208.

Coussy, O. (1995). "Mechanics of porous media." *J. Wiley & Sons, Chichester, UK*.

Dafalias, Y., and Popov, E. (1975). "A model of nonlinearly hardening materials for complex loading." *Acta Mech.*, 21(3), 173-192.

Dafalias, Y. F. (1986). "Bounding Surface Plasticity. I: Mathematical Foundation and Hypoplasticity." *J. Eng. Mech.*, 112(9), 966-987.

Dafalias, Y. F., and Herrmann, L. R. (1986). "Bounding Surface Plasticity. II: Application to Isotropic Cohesive Soils." *J. Eng. Mech.*, 112(12), 1263-1291.

Dafalias, Y. F., and Popov, E. P. (1976). "Plastic Internal Variables Formalism of Cyclic Plasticity." *J. Appl. Mech.*, 43(4), 645-651.

Eseller-Bayat, E., Yegian, M. K., Alshawabkeh, A., and Gokyer, S. (2013a). "Liquefaction Response of Partially Saturated Sands. I: Experimental Results." *J. Geotech. Geoenviron. Eng.*, 139(6), 863–871.

Eseller-Bayat, E., Yegian, M. K., Alshawabkeh, A., and Gokyer, S. (2013b). "Liquefaction Response of Partially Saturated Sands. II: Empirical Model." *J. Geotech. Geoenviron. Eng.*, 139(6), 872-879.

Eseller-Bayat, E. E. (2009). "Seismic response and prevention of liquefaction failure of sands partially saturated through introduction of gas bubbles." Ph.D, Northeastern University, Boston, Massachusetts.

Feng, M., and Fredlund, D. G. (1999). "Hysteretic influence associated with thermal conductivity sensor measurements." *Proc.,From Theory to the Practice of Unsaturated Soil Mechanics, in associated with 52nd Can. Geotech. Conference and Unsaturated Soil Group*, 651-657.

Fourie, A. B., Hofmann, B. A., Mikula, R. J., Lord, E. R. F., and Robertson, P. K. (2001 Published). "Partially saturated tailings sand below the phreatic surface." *Proc.,(CD-ROM)Conference Name*, 577-585.

Fredlund, D. G., and Rahardjo, H. (1993). *Soil mechanics for unsaturated soils*, John Wiley & Sons.

Gallipoli, D., Gens, A., Sharma, R., and Vaunat, J. (2003). "An elasto-plastic model for unsaturated soil incorporating the effects of suction and degree of saturation on mechanical behaviour." *Géotechnique*, 53(1), 123-135.

Geiser, F., Laloui, L., and Vulliet, L. (2006). "Elasto-plasticity of unsaturated soils : laboratory test results on a remoulded silt." *Soils Found.*, 46(5), 545-556.

GENS, A. (2010). "Soil–environment interactions in geotechnical engineering." *Géotechnique*, 60(1), 3-74.

Ghayoomi, M., McCartney, J., and Ko, H. (2011). "Centrifuge Test to Assess the Seismic Compression of Partially Saturated Sand Layers." *Geotech. Test. J.*, 34(4), 321-331.

Gillham, R. W., Klute, A., and Heermann, D. F. (1979). "Measurement and Numerical Simulation of Hysteretic Flow in a Heterogeneous Porous Medium." *Soil Science Society of America Journal*, 43(6), 1061-1067.

Grozic, J. L., Robertson, P. K., and Morgenstern, N. R. (2000). "Cyclic liquefaction of loose gassy sand." *Can. Geotech. J.*, 37(4), 843-856.

Habte, M. A. (2006). "Numerical and Constitutive Modelling of Monotonic and Cyclic Loading in Variably Saturated Soils." Ph.D, University of New South Wales.

Hatanaka, M., and Masuda, T. (2008). "Experimental Study on the Relationship Between Degree of Saturation and P-Wave Velocity in Sandy Soils." *Geotechnical Engineering for Disaster Mitigation and Rehabilitation*, H. Liu, A. Deng, and J. Chu, eds., Springer Berlin Heidelberg, 346-351.

He, J., and Chu, J. (2014). "Undrained Responses of Microbially Desaturated Sand under Monotonic Loading." *J. Geotech. Geoenviron. Eng.*, 140(5), 04014003.

Higo, Y., Lee, C.-W., Doi, T., Kinugawa, T., Kimura, M., Kimoto, S., and Oka, F. (2015). "Study of dynamic stability of unsaturated embankments with different water contents by centrifugal model tests." *Soils Found.*, 55(1), 112-126.

Hilber, H. M., Hughes, T. J. R., and Taylor, R. L. (1977). "Improved numerical dissipation for time integration algorithms in structural dynamics." *Earthquake Eng. Struct. Dyn.*, 5(3), 283-292.

Hossain, A. M., Andrus, R. D., and Camp, W. M. (2013). "Correcting Liquefaction Resistance of Unsaturated Soil Using Wave Velocity." *J. Geotech. Geoenviron. Eng.*, 139(2), 277-287.

Hsu, J. R. C., Jeng, D. S., and Lee, C. P. (1995). "Oscillatory soil response and liquefaction in an unsaturated layered seabed." *Int. J. Numer. Anal. Meth. Geomech.*, 19(12), 825-849.

Huang, Y., Tsuchiya, H., and Ishihara, K. (1999). "Estimation of partial saturation effect on liquefaction resistance of sand using P-wave velocity." *Proceedings of Japanese Geotechnical Society*, 113, 431-434.

Hughes, T. J. (1987). *The finite element method: linear static and dynamic finite element analysis*, Prentice-Hall: Englewood Cliffs, NJ.

Inel, S., and Lade, P. V. (1997). "Rotational kinematic hardening model for sand. Part II Characteristic work hardening law and predictions." *Comput. Geotech.*, 21(3), 217-234.

Ishihara, K., Huang, Y., and Tsuchiya, H. (1998). "Liquefaction resistance of nearly saturated sand as correlated with longitudinal wave velocity." *Poromechanics: a tribute to Maurice A. Biot. Balkema, Rotterdam, the Netherlands*, 583-586.

Ishihara, K., Tsuchiya, H., Huang, Y., and Kamada, K. (2001). "Recent studies on liquefaction resistance of sand effect of saturation (keynote lecture)." *Proc.,4th Int. Conf. on Recent Advances in Geotechnical Earthquake Engineering and Soil Dynamics*.

Ishihara, K., and Tsukamoto, Y. (2004). "Cyclic strength of imperfectly saturated sands and analysis of liquefaction." *Proceedings of the Japan Academy, Series B*, 80(8), 372-391.

Jafari-Mehrabadi, A., Abedinzadegan Abdi, M., and Popescu, R. (2007). "Analysis of liquefaction susceptibility of nearly saturated sands." *Int. J. Numer. Anal. Meth. Geomech.*, 31(5), 691-714.

Kayen, R., Moss, R., Thompson, E., Seed, R., Cetin, K., Kiureghian, A. D., Tanaka, Y., and Tokimatsu, K. (2013). "Shear-wave velocity–based probabilistic and deterministic assessment of seismic soil liquefaction potential." *J. Geotech. Geoenviron. Eng.*, 139(3), 407-419.

Kazama, M., Takamura, H., Unno, T., Sento, N., and Uzuoka, R. (2006). "Liquefaction mechanism of unsaturated volcanic sandy soils." *Journal of Geotechnical Engineering, Japan Society of Civil Engineers*, 62(2), 546-561.

Kazama, M., and Unno, T. (2007). "Earthquake-Induced Mudflow Mechanism from a Viewpoint of Unsaturated Soil Dynamics." *Experimental Unsaturated Soil Mechanics*, T. Schanz, ed., Springer Berlin Heidelberg, Berlin, Heidelberg, 437-444.

Khalili, N., Habte, M. A., and Zargarbashi, S. (2008). "A fully coupled flow deformation model for cyclic analysis of unsaturated soils including hydraulic and mechanical hystereses." *Comput. Geotech.*, 35(6), 872-889.

Khalili, N., and Khabbaz, M. H. (1998). "A unique relationship for χ for the determination of the shear strength of unsaturated soils." *Géotechnique*, 48(5), 681-687.

Khoei, A. R., Azami, A. R., and Haeri, S. M. (2004). "Implementation of plasticity based models in dynamic analysis of earth and rockfill dams: A comparison of Pastor–Zienkiewicz and cap models." *Comput. Geotech.*, 31(5), 384-409.

Khoei, A. R., and Mohammadnejad, T. (2011). "Numerical modeling of multiphase fluid flow in deforming porous media: A comparison between two- and three-phase models for seismic analysis of earth and rockfill dams." *Comput. Geotech.*, 38(2), 142-166.

Khosravi, A., and McCartney, J. S. (2012). "Impact of Hydraulic Hysteresis on the Small-Strain Shear Modulus of Low Plasticity Soils." *J. Geotech. Geoenviron. Eng.*, 138(11), 1326-1333.

Krieg, R. D. (1975). "A practical two surface plasticity theory." *J. Appl. Mech.*, 42(3), 641-646.

Kuhn, M. R., Renken, H. E., Mixsell, A. D., and Kramer, S. L. (2014). "Investigation of Cyclic Liquefaction with Discrete Element Simulations." *J. Geotech. Geoenviron. Eng.*, 140(12), 04014075.

Lade, P., and Kim, M. (1988). "Single hardening constitutive model for frictional materials II. Yield critirion and plastic work contours." *Comput. Geotech.*, 6(1), 13-29.

Laloui, L., Klubertanz, G., and Vulliet, L. (2003). "Solid-liquid-air coupling in multiphase porous media." *Int. J. Numer. Anal. Meth. Geomech.*, 27(3), 183-206.

Lewis, R. W., and Schrefler, B. A. (1998). *The finite element method in the static and dynamic deformation and consolidation of porous media*, John Wiley.

Li, X. S., and Dafalias, Y. F. (2000). "Dilatancy for cohesionless soils." *Géotechnique*, 50(4), 449-460.

Liu, C. (2009). "A coupled hydraulic-mechanical elastoplastic constitutive model for unsaturated sands and silts." Ph.D. dissertation, The University of Oklahoma, Norman, Oklahoma.

Liu, C., and Muraleetharan, K. (2006). "Description of Soil Water Characteristic Curves Using the Bounding Surface Plasticity Theory." *Proc.,4th Int. Conf. on Unsaturated Soils, GSP 147*, Vol. 2, G. A. Miller, C. E. Zapata, S. L. Houston, and D. G. Fredlund, eds., Geo-Institute, ASCE, Carefree, AZ, 2432-2440.

Liu, C., and Muraleetharan, K. (2012a). "Coupled hydro-mechanical elastoplastic constitutive model for unsaturated sands and silts. I: formulation." *Int. J. Geomech.*, 12(3), 239-247.

Liu, C., and Muraleetharan, K. (2012b). "Coupled hydro-mechanical elastoplastic constitutive model for unsaturated sands and silts. II: integration, calibration, and validation." *Int. J. Geomech.*, 12(3), 248-259.

Liu, C., and Muraleetharan, K. (2012c). "Numerical Study on Effects of Initial State on Liquefaction of Unsaturated Soils." *Proc.,GeoCongress 2012*, R. D. Hryciw, A. Athanasopoulos-Zekkos, and N. Yesiller, eds., ASCE, 2432-2441.

Liu, C., and Xu, J. (2015). "Experimental Study on the Effects of Initial Conditions on Liquefaction of Saturated and Unsaturated Sand." *Int. J. Geomech.*, 15(6), 04014100.

Maghoul, P., Gatmiri, B., and Duhamel, D. (2011a). "Boundary integral formulation and two-dimensional fundamental solutions for dynamic behavior analysis of unsaturated soils." *Soil Dyn. Earthquake Eng.*, 31(11), 1480-1495.

Maghoul, P., Gatmiri, B., and Duhamel, D. (2011b). "Wave Propagation in Unsaturated Poroelastic Media: Boundary Integral Formulation and Three-dimensional Fundamental Solution." *Comput. Model. Eng. Sci.*, 78(1), 51-76.

Manzari, M. T., and Dafalias, Y. F. (1997). "A critical state two-surface plasticity model for sands." *Géotechnique*, 47(2), 255-272.

Martin, G. R., Seed, H. B., and Finn, W. (1978). "Effects of system compliance on liquefaction tests." *J. Geotech. Engrg. Div.*, 104(4), 463-479.

Matsumaru, T., and Uzuoka, R. (2016). "Three-Phase Seepage-Deformation Coupled Analysis about Unsaturated Embankment Damaged by Earthquake." *Int. J. Geomech.*, 16(5), C4016006.

Maurer, B., Green, R., Cubrinovski, M., and Bradley, B. (2015). "Assessment of CPT-based methods for liquefaction evaluation in a liquefaction potential index framework." *Géotechnique*, 65(5), 328-336.

Meroi, E. A., Schrefler, B. A., and Zienkiewicz, O. C. (1995). "Large strain static and dynamic semisaturated soil behaviour." *Int. J. Numer. Anal. Meth. Geomech.*, 19(2), 81-106.

Miller, G. A., Khoury, C. N., Muraleetharan, K. K., Liu, C., and Kibbey, T. C. G. (2008). "Effects of soil skeleton deformations on hysteretic soil water characteristic curves: Experiments and simulations." *Water Resour. Res.*, 44(5), W00C06.

Montgomery, J., Boulanger, R., and Harder, L. (2014). "Examination of the Kσ Overburden Correction Factor on Liquefaction Resistance." *J. Geotech. Geoenviron. Eng.*, 140(12), 04014066.

Mori, T., Uzuoka, R., Chiba, T., Kamiya, K., and Kazama, M. (2011). "Numerical prediction of seepage and seismic behavior of unsaturated fill slope." *Soils Found.*, 51(6), 1075-1090.

Mróz, Z. (1967). "On the description of anisotropic workhardening." *J. Mech. Phys. Solids*, 15(3), 163-175.

Mróz, Z., Norris, V. A., and Zienkiewicz, O. C. (1979). "Application of an anisotropic hardening model in the analysis of elasto–plastic deformation of soils." *Géotechnique*, 29(1), 1-34.

Mrŏz, Z., Norris, V. A., and Zienkiewicz, O. C. (1978). "An anisotropic hardening model for soils and its application to cyclic loading." *Int. J. Numer. Anal. Meth. Geomech.*, 2(3), 203-221.

Mróz, Z., and Pietruszczak, S. (1983). "A constitutive model for sand with anisotropic hardening rule." *Int. J. Numer. Anal. Meth. Geomech.*, 7(3), 305-320.

Mualem, Y. (1976). "A new model for predicting the hydraulic conductivity of unsaturated porous media." *Water Resour. Res.*, 12(3), 513-522.

Muraleetharan, K., Mish, K., and Arulanandan, K. (1994). "A fully coupled non‐linear dynamic analysis procedure and its verification using centrifuge test results." *Int. J. Numer. Anal. Meth. Geomech.*, 18(5), 305-325.

Muraleetharan, K., and Nedunuri, P. (1998). "A bounding surface elastoplastic constitutive model for monotonic and cyclic behavior of unsaturated soils." *Proc.,12th Engineering Mechanics Conference, ASCE, La Jolla, CA*, 1331-1334.

Muraleetharan, K. K., Deshpande, S., and Adalier, K. (2004). "Dynamic deformations in sand embankments: centrifuge modeling and blind, fully coupled analyses." *Can. Geotech. J.*, 41(1), 48-69.

Muraleetharan, K. K., Liu, C., Wei, C., Kibbey, T. C. G., and Chen, L. (2009). "An elastoplatic framework for coupling hydraulic and mechanical behavior of unsaturated soils." *Int. J. Plast.*, 25(3), 473-490.

Muraleetharan, K. K., and Wei, C. (1999a). "Dynamic behaviour of unsaturated porous media: governing equations using the Theory of Mixtures with Interfaces (TMI)." *Int. J. Numer. Anal. Meth. Geomech.*, 23(13), 1579-1608.

Muraleetharan, K. K., and Wei, C. (1999b). "U_DYSAC2: Unsaturated Dynamic Soil Analysis Code for 2-dimensional problems." *Computer Code,* School of Civil Engineering and Environmental Science, University of Oklahoma, Norman, Oklahoma.

Muraleetharan, K. K., and Wei, C. (2000). "A Fully Coupled Analysis Procedure for Dynamic Behavior of Unsaturated Soils." *Proc.,GSP No. 99, Proceedings, GeoDenver 2000 Conference*, C. D. Shackelford, S. L. Houston, and N.-Y. Chang, eds., Geo-Institute, ASCE, 165-179.

Nagao, K., Azegami, Y., Yamada, S., Suemasa, N., and Katada, T. (2007). "A micro-bubble injection method for a countermeasure against liquefaction." *Proc.,4th International conference on earthquake geotechnical engineering, Thessaloniki*, 25-28.

Nakazawa, H., Ishihara, K., Tsukamoto, Y., and Kamata, T. (2004). "Case studies on evaluation of liquefaction resistance of imperfectly saturated soil deposits." *Proc.,International Conference on Cyclic Behaviour of Soils and Liquefaction Phenomena, Bochum, Germany*, Vol. 31, 295-304.

Ng, C. W. W., Xu, J., and Yung, S. Y. (2009). "Effects of wetting–drying and stress ratio on anisotropic stiffness of an unsaturated soil at very small strains." *Can. Geotech. J.*, 46(9), 1062-1076.

Oettl, G., Stark, R. F., and Hofstetter, G. (2004). "Numerical simulation of geotechnical problems based on a multi-phase finite element approach." *Comput. Geotech.*, 31(8), 643-664.

Oka, F., Tsai, P., Kimoto, S., and Kato, R. (2012). "Damage patterns of river embankments due to the 2011 off the Pacific Coast of Tohoku Earthquake and a numerical modeling of the deformation of river embankments with a clayey subsoil layer." *Soils Found.*, 52(5), 890-909.

Oka, F., Yashima, A., Shibata, T., Kato, M., and Uzuoka, R. (1994). "FEM-FDM coupled liquefaction analysis of a porous soil using an elasto-plastic model." *Appl. Sci. Res.*, 52(3), 209-245.

Okamura, M., Ishihara, M., and Oshita, T. (2003). "Liquefaction resistance of sand deposit improved with sand compaction piles." *Soils Found.*, 43(5), 175-187.

Okamura, M., Ishihara, M., and Tamura, K. (2006). "Degree of Saturation and Liquefaction Resistances of Sand Improved with Sand Compaction Pile." *J. Geotech. Geoenviron. Eng.*, 132(2), 258-264.

Okamura, M., and Soga, Y. (2006). "Effects of pore fluid compressibility on liquefaction resistance of partially saturated sand " *Soils Found.*, 46(5), 695-700.

Okamura, M., Takebayashi, M., Nishida, K., Fujii, N., Jinguji, M., Imasato, T., Yasuhara, H., and Nakagawa, E. (2011). "In-Situ Desaturation Test by Air Injection and Its Evaluation through Field Monitoring and Multiphase Flow Simulation." *J. Geotech. Geoenviron. Eng.*, 137(7), 643-652.

Okamura, M., Tamamura, S., and Yamamoto, R. (2013). "Seismic stability of embankments subjected to pre-deformation due to foundation consolidation." *Soils Found.*, 53(1), 11-22.

Okamura, M., and Teraoka, T. (2005). "Shaking Table Tests to Investigate Soil Desaturation as a Liquefaction Countermeasure." *Seismic Performance and Simulation of Pile Foundations in Liquefied and Laterally Spreading Ground*, ASCE, 282-293.

Pastor, M., Zienkiewicz, O. C., and Chan, A. H. C. (1990). "Generalized plasticity and the modelling of soil behaviour." *Int. J. Numer. Anal. Meth. Geomech.*, 14(3), 151-190.

Pedroso, D. M. (2015). "A consistent u-p formulation for porous media with hysteresis." *Int. J. Numer. Methods Eng.*, 101(8), 606-634.

Pietruszczak, S., and Mróz, Z. (1983). "On hardening anisotropy of K0-consolidated clays." *Int. J. Numer. Anal. Meth. Geomech.*, 7(1), 19-38.

Pietruszczak, S., and Pande, G. N. (1996). "Constitutive Relations for Partially Saturated Soils Containing Gas Inclusions." *Journal of Geotechnical Engineering*, 122(1), 50-59.

Pietruszczak, S., Pande, G. N., and Oulapour, M. (2003). "A hypothesis for mitigation of risk of liquefaction." *Géotechnique*, 53(9), 833-838.

Poulovassilis, A. (1970). "HYSTERESIS OF PORE WATER IN GRANULAR POROUS BODIES." *Soil Science*, 109(1), 5-12.

Qi, S., and Vanapalli, S. K. (2015). "Hydro-mechanical coupling effect on surficial layer stability of unsaturated expansive soil slopes." *Comput. Geotech.*, 70, 68-82.

Rampino, C., Mancuso, C., and Vinale, F. (1999). "Laboratory testing on an unsaturated soil: equipment, procedures, and first experimental results." *Can. Geotech. J.*, 36(1), 1-12.

Ravichandran, N. (2009). "Fully coupled finite element model for dynamics of partially saturated soils." *Soil Dyn. Earthquake Eng.*, 29(9), 1294-1304.

Ravichandran, N., Krishnapillai, S., Bhuiyan, A., and Huggins, E. (2015). "Simplified Finite-Element Model for Site Response Analysis of Unsaturated Soil Profiles." *Int. J. Geomech.*, 16(1), 04015036.

Ravichandran, N., and Krishnapillai, S. H. (2013). "Effect of Deformation-Induced Suction in the Behavior of Unsaturated Fine-Grained Soils Using Simplified Finite-Element Model." *Int. J. Geomech.*, 13(5), 483-495.

Ravichandran, N., and Muraleetharan, K. K. (2009). "Dynamics of unsaturated soils using various finite element formulations." *Int. J. Numer. Anal. Meth. Geomech.*, 33(5), 611-631.

Rebata-Landa, V., and Santamarina, J. C. (2012). "Mechanical Effects of Biogenic Nitrogen Gas Bubbles in Soils." *J. Geotech. Geoenviron. Eng.*, 138(2), 128–137.

Robertson, P., and Campanella, R. (1985). "Liquefaction Potential of Sands Using the CPT." *Journal of Geotechnical Engineering*, 111(3), 384-403.

Sadeghi, H., Kimoto, S., Oka, F., and Shahbodagh, B. (2014). "Dynamic analysis of river embankments during earthquakes using a finite deformation FE analysis method." *Proc.,14th International Conference of the International Association for Computer Methods and Advances in Geomechanics*, F. Oka, A. Murakami, R. Uzuoka, and S. Kimoto, eds., CRC Press, 637-642.

Sawada, S., Tsukamoto, Y., and Ishihara, K. (2006). "Residual deformation characteristics of partially saturated sandy soils subjected to seismic excitation." *Soil Dyn. Earthquake Eng.*, 26(2–4), 175-182.

Schrefler, B. A. (1984). "The finite element method in soil consolidation (with applications to surface subsidence)." Ph.D. dissertation, University College of Swansea.

Schrefler, B. A., and Scotta, R. (2001). "A fully coupled dynamic model for two-phase fluid flow in deformable porous media." *Comput. Meth. Appl. Mech. Eng.*, 190(24–25), 3223-3246.

Schrefler, B. A., and Xiaoyong, Z. (1993). "A fully coupled model for water flow and airflow in deformable porous media." *Water Resour. Res.*, 29(1), 155-167.

Seed, H. B., and Idriss, I. M. (1971). "Simplified procedure for evaluating soil liquefaction potential." *Journal of Soil Mechanics & Foundations Div*, 97(9), 1249–1273.

Seed, H. B., and Idriss, I. M. (1982). *Ground motions and soil liquefaction during earthquakes*, Earthquake Engineering Research Institute.

Seed, H. B., Idriss, I. M., and Arango, I. (1983). "Evaluation of Liquefaction Potential Using Field Performance Data." *Journal of Geotechnical Engineering*, 109(3), 458-482.

Seed, H. B., Tokimatsu, K., Harder, L., and Chung, R. (1985). "Influence of SPT Procedures in Soil Liquefaction Resistance Evaluations." *Journal of Geotechnical Engineering*, 111(12), 1425-1445.

Shahbodagh-Khan, B., Khalili, N., and Alipour Esgandani, G. (2015). "A numerical model for nonlinear large deformation dynamic analysis of unsaturated porous media including hydraulic hysteresis." *Comput. Geotech.*, 69, 411-423.

Sheng, D., Fredlund, D. G., and Gens, A. (2008a). "A new modelling approach for unsaturated soils using independent stress variables." *Can. Geotech. J.*, 45(4), 511-534.

Sheng, D., Gens, A., Fredlund, D. G., and Sloan, S. W. (2008b). "Unsaturated soils: From constitutive modelling to numerical algorithms." *Comput. Geotech.*, 35(6), 810-824.

Sheng, D., Sloan, S. W., Gens, A., and Smith, D. W. (2003). "Finite element formulation and algorithms for unsaturated soils. Part I: Theory." *Int. J. Numer. Anal. Meth. Geomech.*, 27(9), 745-765.

Sheng, D., Sloan, W. S., and Gens, A. (2004). "A constitutive model for unsaturated soils: thermomechanical and computational aspects." *Comput. Mech.*, 33(6), 453-465.

Sherif, M. A., Tsuchiya, C., and Ishibashi, I. (1977). "Saturation effects on initial soil liquefaction." *J. Geotech. Eng. Div.*, 103(8), 914-917.

Shiraishi, T. (1997). "Pneumatic caisson foundation can stand up the severe earthquake." *The foundation engineering & equipment*, 25(9), 120-127.

Singh, R., Roy, D., and Jain, S. K. (2005). "Analysis of earth dams affected by the 2001 Bhuj Earthquake." *Eng. Geol.*, 80(3–4), 282-291.

Steeb, H., Kurzeja, P. S., and Schmalholz, S. M. (2014). "Wave propagation in unsaturated porous media." *Acta Mech.*, 225(8), 2435-2448.

Stelzer, R., and Hofstetter, G. (2005). "Adaptive finite element analysis of multi-phase problems in geotechnics." *Comput. Geotech.*, 32(6), 458-481.

Taboada, V., and Dobry, R. (1993). "Experimental results of model No. 1 at RPI." *Proc.,International Conference on the Verification of Numerical Procedures for the Analysis of Soil Liquefaction Problems* A. K, and S. RF, eds., Rotterdam: A.A. Balkema, 3-18.

Taiebat, M., and Dafalias, Y. F. (2008). "SANISAND: Simple anisotropic sand plasticity model." *Int. J. Numer. Anal. Meth. Geomech.*, 32(8), 915-948.

Tamagnini, R. (2004). "An extended Cam-clay model for unsaturated soils with hydraulic hysteresis." *Géotechnique*, 54(3), 223-228.

Tamagnini, R. (2005). "The influence of hydraulic hysteresis on unsaturated soils FE analyses." *Unsaturated Soils: Numerical and Theoretical Approaches: Proceedings of the International Conference "From Experimental Evidence towards Numerical Modeling of Unsaturated Soils," Weimar, Germany, September 18–19, 2003*, T. Schanz, ed., Springer Berlin Heidelberg, Berlin, Heidelberg, 67-80.

Tan, N. K. (2005). "Pressuremeter and cone penetrometer testing in a calibration chamber with unsaturated Minco Silt." Ph.D Dissertation, University of Oklahoma, Norman, Oklahoma.

Tarantino, A., and Tombolato, S. (2005). "Coupling of hydraulic and mechanical behaviour in unsaturated compacted clay." *Géotechnique*, 55(4), 307-317.

Topp, G. C. (1969). "Soil-Water Hysteresis Measured in a Sandy Loam and Compared with the Hysteretic Domain Model1." *Soil Sci. Soc. Am. J.*, 33(5), 645-651.

Topp, G. C. (1971). "Soil Water Hysteresis in Silt Loam and Clay Loam Soils." *Water Resour. Res.*, 7(4), 914-920.

Tsukamoto, Y., Ishihara, K., Nakazawa, H., Kamada, K., and Huang, Y. (2002). "Resistance of partly saturated sand to liquefaction with reference to longitudinal and shear wave velocities." *Soils Found.*, 42(6), 93-104.

Tsukamoto, Y., Kawabe, S., Matsumoto, J., and Hagiwara, S. (2014). "Cyclic resistance of two unsaturated silty sands against soil liquefaction." *Soils Found.*, 54(6), 1094-1103.

Unno, T., Kazama, M., Uzuoka, R., and Sento, N. (2008). "Liquefaction of unsaturated sand considering the pore air pressure and volume compressibility of the soil particle skelton." *Soils Found.*, 48(1), 87-99.

Uzuoka, R., and Borja, R. I. (2012). "Dynamics of unsaturated poroelastic solids at finite strain." *Int. J. Numer. Anal. Meth. Geomech.*, 36(13), 1535-1573.

Uzuoka, R., Sento, N., Kazama, M., and Unno, T. (2005). "Landslides during the earthquakes on May 26 and July 26, 2003 in Miyagi, Japan." *Soils Found.*, 45(4), 149-163.

Uzuoka, R., Unno, T., Sento, N., and Kazama, M. (2014). "Effect of pore air pressure on cyclic behavior of unsaturated sandy soil." *Proc.,6th Int. Conf. on Unsaturated Soils*, Vol. 2, N. Khalili, A. R. Russell, and A. Khoshghalb, eds., CRC Press, 783-789.

van Genuchten, M. T. (1980). "A Closed-form Equation for Predicting the Hydraulic Conductivity of Unsaturated Soils1." *Soil Sci. Soc. Am. J.*, 44(5).

Vanapalli, S. K., Fredlund, D. G., and Pufahl, D. E. (1999). "The influence of soil structure and stress history on the soil–water characteristics of a compacted till." *Géotechnique*, 49(2), 143-159.

Vaunat, J., Romero, E., and Jommi, C. (2000). "An elastoplastic hydromechanical model for unsaturated soils." *Experimental evidence and theoretical approaches in unsaturated soils*, 121-138.

Verdugo, R., and Ishihara, K. (1996). "The steady state of sandy soils." *Soils Found.*, 36(2), 81-91.

Vinayagam, T. (2004). "Understanding the stress-strain behavior of unsaturated Minco silt using laboratory testing and constitutive modeling." Master Thesis, University of Oklahoma, Norman, Oklahoma.

Wei, C. (2001). "Static and dynamic behavior of multiphase porous media: Governing equations and finite element implementation." Ph.D. dissertation, University of Oklahoma, Norman, Oklahoma.

Wei, C., and Muraleetharan, K. K. (2002a). "A continuum theory of porous media saturated by multiple immiscible fluids: I. Linear poroelasticity." *Int. J. Eng. Sci.*, 40(16), 1807-1833.

Wei, C., and Muraleetharan, K. K. (2002b). "A continuum theory of porous media saturated by multiple immiscible fluids: II. Lagrangian description and variational structure." *Int. J. Eng. Sci.*, 40(16), 1835-1854.

Wheeler, S. J. (1996). "Inclusion of specific water volume within an elasto-plastic model for unsaturated soil." *Can. Geotech. J.*, 33(1), 42-57.

Wheeler, S. J., Sharma, R. S., and Buisson, M. S. R. (2003). "Coupling of hydraulic hysteresis and stress–strain behaviour in unsaturated soils." *Géotechnique*, 53(1), 41-54.

Wheeler, S. J., and Sivakumar, V. (1995 Published). "An elasto-plastic critical state framework for unsaturated soil." *Proc.,(CD-ROM)Conference Name*, 35-53.

Xia, H., and Hu, T. (1991). "Effects of saturation and back pressure on sand liquefaction." *J. Geotech. Engrg.*, 117(9), 1347-1362.

Xu, J. (2012). "Liquefaction potential of unsaturated nevada sand at different initial conditions." Master M.S. thesis, University of South Carolina, Columbia, South Carolina.

Yang, C., Cui, Y. J., Pereira, J. M., and Huang, M. S. (2008). "A constitutive model for unsaturated cemented soils under cyclic loading." *Comput. Geotech.*, 35(6), 853-859.

Yang, J. (2002). "Liquefaction resistance of sand in relation to P-wave velocity." *Géotechnique*, 52, 295-298.

Yang, J., Savidis, S., and Roemer, M. (2004). "Evaluating Liquefaction Strength of Partially Saturated Sand." *J. Geotech. Geoenviron. Eng.*, 130(9), 975-979.

Yegian, M., Eseller-Bayat, E., Alshawabkeh, A., and Ali, S. (2007). "Induced-partial saturation for liquefaction mitigation: experimental investigation." *J. Geotech. Geoenviron. Eng.*, 133(4), 372-380.

Yoshikawa, T., Noda, T., Kodaka, T., and Takaine, T. (2016). "Analysis of the effect of groundwater level on the seismic behavior of an unsaturated embankment on clayey ground." *Soil Dyn. Earthquake Eng.*, 85, 217-230.

Yoshimi, Y., Tanaka, K., and Tokimatsu, K. (1989). "Liquefaction resiatance of a partially saturated sand " *Soils Found.*, 29(3), 157-162.

Youd, T., Idriss, I., Andrus, R., Arango, I., Castro, G., Christian, J., Dobry, R., Finn, W., Harder, L., Hynes, M., Ishihara, K., Koester, J., Liao, S., Marcuson, W., Martin, G., Mitchell, J., Moriwaki, Y., Power, M., Robertson, P., Seed, R., and Stokoe, K. (2001). "Liquefaction Resistance of Soils: Summary Report from the 1996 NCEER and 1998 NCEER/NSF Workshops on Evaluation of Liquefaction Resistance of Soils." *J. Geotech. Geoenviron. Eng.*, 127(10), 817-833.

Zhang, B., and Muraleetharan, K. K. (2017). "Numerical Modelling of the Dynamic Behavior of Unsaturated Soils, Including Hydraulic Hysteresis." *Proc.,Geotechnical Frontiers 2017: Seismic Performance and Liquefaction*, T. L. Brandon, and R. J. Valentine, eds., ASCE, Reston, VA, 61-70.

Zhang, B., Muraleetharan, K. K., and Liu, C. (2015). "Predicting liquefaction of unsaturated sands using a coupled hydro-mechanical elastoplastic constitutive model." *Proc.,6th Asia Pacific Conference on Unsaturated Soils*, Z. Chen, C. Wei, D. Sun, and X. Xu, eds., CRC Press, 607-611.

Zhang, B., Muraleetharan, K. K., and Liu, C. (2016). "Liquefaction of Unsaturated Sands." *Int. J. Geomech.*, 16(6), D4015002.

Zhou, C., and Ng, C. W. W. (2016). "Simulating the cyclic behaviour of unsaturated soil at various temperatures using a bounding surface model." *Géotechnique*, 66(4), 344-350.

Zienkiewicz, O. C., Xie, Y. M., Schrefler, B. A., Ledesma, A., and Bi̊anić, N. (1990). "Static and Dynamic Behaviour of Soils: A Rational Approach to Quantitative Solutions. II. Semi-Saturated Problems." *Proc. R. Soc. Lond. A*, 429(1877), 311-321.

APPENDIX A: DERIVATION OF $\frac{\partial \Gamma}{\partial n_w}$

$$\frac{\partial \Gamma}{\partial n_w} = \frac{\left(\Gamma^e\right)^2 \frac{\partial \Gamma^p}{\partial n_w}}{\left(\Gamma^e + \Gamma^p\right)^2} \tag{A.1}$$

$$\frac{\partial \Gamma^p}{\partial n_w} = \frac{\partial \Gamma^p}{\partial \Gamma_0^p}\frac{\partial \Gamma_0^p}{\partial n_w} + \Gamma_0^p H \frac{\partial\left(\delta / <\delta_{in} - g\delta>\right)}{\partial \delta}\frac{\partial \delta}{\partial n_w} \tag{A.2}$$

$$\frac{\partial \Gamma^p}{\partial \Gamma_0^p} = 1 + \frac{H\delta}{<\delta_{in} - g\delta>} \tag{A.3}$$

$$\Gamma_0^p = \frac{\partial s_c}{\partial n_w} \text{(on the bounding curve)},\ \frac{\partial \Gamma_0^p}{\partial n_w} = \frac{\partial^2 s_c}{\partial^2 n_w} \tag{A.4}$$

$$\text{Drying: } \frac{\partial \Gamma_0^p}{\partial n_w} = \frac{b_3}{d_3}\left(\frac{n_{ws} - n_w}{n_w - n_{wr}}\right)^{\frac{1}{d_3}-2} \frac{\left(n_{ws} - n_{wr}\right)}{\left(n_w - n_{wr}\right)^4}\left[2\left(n_{ws} - n_w\right) + \left(\frac{1}{d_3} - 1\right)\left(n_{ws} - n_{wr}\right)\right] \tag{A.5}$$

$$\text{Wetting: } \frac{\partial \Gamma_0^p}{\partial n_w} = \frac{b_2}{d_2}\left(\frac{n_{ws} - n_w}{n_w - n_{wr}}\right)^{\frac{1}{d_2}-2} \frac{\left(n_{ws} - n_{wr}\right)}{\left(n_w - n_{wr}\right)^4}\left[2\left(n_{ws} - n_w\right) + \left(\frac{1}{d_2} - 1\right)\left(n_{ws} - n_{wr}\right)\right] \tag{A.6}$$

$$\frac{\partial\left(\delta / <\delta_{in} - g\delta>\right)}{\partial \delta} = \frac{<\delta_{in} - g\delta> + g\delta <\delta_{in} - g\delta> / \left(\delta_{in} - g\delta\right)}{\left(<\delta_{in} - g\delta>\right)^2} \tag{A.7}$$

$$\text{Wetting: } \partial\delta / \partial n_w = -\Gamma_{0w}^p,\ \partial\delta / \partial s_{c0w} = -1 \tag{A.8}$$

$$\text{Drying: } \partial\delta / \partial n_w = \Gamma_{0d}^p,\ \partial\delta / \partial s_{c0d} = 1 \tag{A.9}$$

$$\Gamma_{0w}^p = -\frac{b_2}{d_2}\left(\frac{n_{ws} - n_w}{n_w - n_{wr}}\right)^{\frac{1}{d_2}-1} \frac{\left(n_{ws} - n_{wr}\right)}{\left(n_w - n_{wr}\right)^2} \tag{A.10}$$

$$\Gamma_{0d}^{p} = -\frac{b_3}{d_3}\left(\frac{n_{ws}-n_w}{n_w-n_{wr}}\right)^{\frac{1}{d_3}-1}\frac{\left(n_{ws}-n_{wr}\right)}{\left(n_w-n_{wr}\right)^2} \tag{A.11}$$

Γ_{0w}^{p} and Γ_{0d}^{p} the capillary plastic moduli on the wetting and drying bound, respectively.

APPENDIX B: COMPUTATION OF $\mathbf{T} = \dfrac{\partial \bar{\mathbf{R}}}{\partial \mathbf{U}}$

All variables in $\Delta \mathrm{U}_{n+1}^{(m)}$ are assumed to be independent basic variables except the mean intergranular confining stress I is related to the volumetric water content n_w^p. In the following derivatives are computed in the general situation.

$$\frac{\partial \bar{R}_1}{\partial n_w^p} = \frac{\partial \bar{R}_1}{\partial I}\frac{\partial I}{\partial n_w^p} = \frac{\partial \bar{R}_1}{\partial I} s_c = s_c \tag{B.1}$$

$$\frac{\partial \bar{R}_2}{\partial n_w^p} = \frac{\partial \bar{R}_2}{\partial I} s_c = -\frac{\partial D}{\partial I}\Lambda s_c \tag{B.2}$$

$$\frac{\partial \bar{\mathbf{R}}_3}{\partial n_w^p} = \frac{\partial \bar{\mathbf{R}}_3}{\partial I} s_c = -2\left(\Delta\varepsilon_q - \Delta\varepsilon_q^p\right)\frac{\partial G}{\partial I} s_c \tag{B.3}$$

$$\frac{\partial \bar{\mathbf{R}}_4}{\partial n_w^p} = \frac{\partial \bar{\mathbf{R}}_4}{\partial I} s_c = -\Lambda \frac{\partial \mathbf{n}}{\partial I} s_c \tag{B.4}$$

$$\frac{\partial \bar{R}_5}{\partial n_w^p} = 1 + \frac{\Delta s_{c,n+1}}{\left(\Gamma^p\right)^2}\frac{\partial \Gamma^p}{\partial n_w^p},\quad \frac{\partial \bar{R}_5}{\partial s_{c0w}} = \frac{\Delta s_{c,n+1}}{\left(\Gamma^p\right)^2}\frac{\partial \Gamma^p}{\partial s_{c0w}},\quad \frac{\partial \bar{R}_5}{\partial s_{c0d}} = \frac{\Delta s_{c,n+1}}{\left(\Gamma^p\right)^2}\frac{\partial \Gamma^p}{\partial s_{c0d}} \tag{B.5}$$

$$\frac{\partial \bar{\mathbf{R}}_6}{\partial n_w^p} = -\Lambda\left(\mathbf{b}\frac{\partial h}{\partial I} + h\frac{\partial \mathbf{b}}{\partial I}\right) s_c \tag{B.6}$$

$$\frac{\partial \bar{R}_7}{\partial n_w^p} = -c_m\left(1+e_0\right)\Lambda\frac{\partial D}{\partial I} s_c - c_v \varpi \left(\frac{s_c}{p_{ref}}\right)^{\varpi}\left(n_w\right)^{\varpi-1}\Delta n_w^p - c_v\left(\frac{s_c n_w}{p_{ref}}\right)^{\varpi} \tag{B.7}$$

$$\frac{\partial \bar{\mathbf{R}}_8}{\partial n_w^p} = \frac{\partial \bar{\mathbf{R}}_8}{\partial I} s_c = \Lambda c_f\left[< -D > F_{\max}\frac{\partial \mathbf{n}}{\partial I} + \frac{\partial < -D >}{\partial I}\left(F_{\max}\mathbf{n} + \mathbf{F}\right)\right] s_c \tag{B.8}$$

$$\frac{\partial \bar{R}_9}{\partial n_w^p} = \frac{1}{d_2}\frac{\left(n_{ws}-n_{wr}\right)s_{0w,n}}{\left(n_{ws}-n_w\right)\left(n_w-n_{wr}\right)}\left[1+\frac{\left(2n_w-n_{ws}-n_{wr}\right)}{\left(n_{ws}-n_w\right)\left(n_w-n_{wr}\right)}\Delta n_w^p\right] \exp\left[\zeta v\Delta\varepsilon_v^p - \frac{1}{d_2}\frac{\left(n_{ws}-n_{wr}\right)\Delta n_w^p}{\left(n_{ws}-n_w\right)\left(n_w-n_{wr}\right)}\right] \tag{B.9}$$

$$\frac{\partial \bar{R}_{10}}{\partial n_w^p} = \frac{1}{d_3}\frac{\left(n_{ws}-n_{wr}\right)s_{0d,n}}{\left(n_{ws}-n_w\right)\left(n_w-n_{wr}\right)}\left[1+\frac{\left(2n_w-n_{ws}-n_{wr}\right)}{\left(n_{ws}-n_w\right)\left(n_w-n_{wr}\right)}\Delta n_w^p\right] \exp\left[\zeta v\Delta\varepsilon_v^p - \frac{1}{d_3}\frac{\left(n_{ws}-n_{wr}\right)\Delta n_w^p}{\left(n_{ws}-n_w\right)\left(n_w-n_{wr}\right)}\right] \tag{B.10}$$

$$\frac{\partial \bar{R}_{11}}{\partial n_w^p} = \frac{\partial \bar{R}_{11}}{\partial I}s_c = \frac{\partial\sqrt{\mathbf{r}:\mathbf{r}}}{\partial I} - \sqrt{2/3}m\left(\frac{2-\left(2+\beta\right)\left(I/I_0\right)^\beta}{2\sqrt{1-\left(I/I_0\right)^\beta}}\right)s_c \tag{B.11}$$

More derivatives are needed for the above-mentioned quantities, which are given as following:

$$\frac{\partial \Gamma^p}{\partial n_w^p} = \frac{\partial \Gamma^p}{\partial n_w} = \frac{\partial \Gamma^p}{\partial \Gamma_0^p}\frac{\partial \Gamma_0^p}{\partial n_w} + \Gamma_0^p H\frac{\partial\left(\delta/<\delta_{in}-g\delta>\right)}{\partial\delta}\frac{\partial\delta}{\partial n_w} \tag{B.12}$$

$$\frac{\partial \Gamma^p}{\partial s_{c0w}} = \frac{\partial \Gamma^p}{\partial \Gamma_0^p}\frac{\partial \Gamma_0^p}{\partial s_{c0w}} + \Gamma_0^p H\frac{\partial\left(\delta/<\delta_{in}-g\delta>\right)}{\partial\delta}\frac{\partial\delta}{\partial s_{c0w}} \tag{B.13}$$

$$\frac{\partial \Gamma^p}{\partial s_{c0d}} = \frac{\partial \Gamma^p}{\partial \Gamma_0^p}\frac{\partial \Gamma_0^p}{\partial s_{c0d}} + \Gamma_0^p H\frac{\partial\left(\delta/<\delta_{in}-g\delta>\right)}{\partial\delta}\frac{\partial\delta}{\partial s_{c0d}} \tag{B.14}$$

$$\frac{\partial \Gamma^p}{\partial \Gamma_0^p} = 1+\frac{H\delta}{<\delta_{in}-g\delta>} \tag{B.15}$$

Drying: $\frac{\partial \Gamma_0^p}{\partial n_w} = -\frac{s_{c0d}}{d_3}\frac{\left(n_{ws}-n_{wr}\right)\left(2n_w-n_{ws}-n_{wr}\right)}{\left(n_{ws}-n_w\right)^2\left(n_w-n_{wr}\right)^2}$ (B.16)

Wetting: $$\frac{\partial \Gamma_0^p}{\partial n_w} = -\frac{s_{c0w}}{d_2}\frac{\left(n_{ws}-n_{wr}\right)\left(2n_w-n_{ws}-n_{wr}\right)}{\left(n_{ws}-n_w\right)^2\left(n_w-n_{wr}\right)^2} \tag{B.17}$$

$$\frac{\partial \Gamma_0^p}{\partial s_{c0w}} = -\frac{1}{d_2}\frac{\left(n_{ws}-n_{wr}\right)}{\left(n_{ws}-n_w\right)\left(n_w-n_{wr}\right)} \tag{B.18}$$

$$\frac{\partial \Gamma_0^p}{\partial s_{c0d}} = -\frac{1}{d_3}\frac{\left(n_{ws}-n_{wr}\right)}{\left(n_{ws}-n_w\right)\left(n_w-n_{wr}\right)} \tag{B.19}$$

$$\frac{\partial\left(\delta/<\delta_{in}-g\delta>\right)}{\partial\delta} = \frac{<\delta_{in}-g\delta>+g\delta<\delta_{in}-g\delta>/\left(\delta_{in}-g\delta\right)}{\left(<\delta_{in}-g\delta>\right)^2} \tag{B.20}$$

Wetting: $\partial\delta/\partial n_w = -\Gamma_{0w}^p, \partial\delta/\partial s_{c0w} = -1$ (B.21)

Drying: $\partial\delta/\partial n_w = \Gamma_{0d}^p;\ \partial\delta/\partial s_{c0d} = 1$ (B.22)